

Experimental and analytical investigation of shear-reinforced concrete and dowel action

Présentée le 15 mars 2024

Faculté de l'environnement naturel, architectural et construit
Laboratoire de construction en béton
Programme doctoral en génie civil et environnement

pour l'obtention du grade de Docteur ès Sciences

par

Marko PEJATOVIĆ

Acceptée sur proposition du jury

Prof. A. Nussbaumer, président du jury
Prof. A. Muttoni, directeur de thèse
Prof. M. di Prisco, rapporteur
Prof. B. Mihaylov, rapporteur
Prof. D. Ruggiero, rapporteur

To my dear parents Mira and Žarko,
to my brother Mirko, and sister Tijana,
to my wife Sara

Foreword

This doctoral thesis deals with two topics related to the shear resistance of reinforced concrete beams and the fatigue of concrete structures.

The first topic concerns the shear resistance of beams with shear reinforcement and loads applied close to the supports. While solutions based on the stress field method (which in turn is based on limit analysis) are well known for elements of this type with loads sufficiently far from the supports, and have been implemented in standards in the form of easy-to-use formulae for some decades now, the situation is different for the case studied with forces close to the supports. For this case too, solutions based on limit analysis exist, but have never been systematically validated and, above all, the solutions are difficult to use in practice. For this reason, simplified methods or methods based on an empirical approach are generally used in practice.

Marko Pejatović's work fills this gap. Theoretical work has made it possible to derive easy-to-use formulae for estimating the shear resistance of squat members. These have been implemented in the 2nd generation of the European standard for concrete structures EN 1992-1-1:2023, as well as in the international standard *fib* MC2020 published some months ago.

The second topic concerns the dowel action of reinforcing bars (i.e., their ability to carry a shear force) as well as the bending stresses that develop in steel reinforcing bars as a result of the slip and the opening of a crack running through them. The research first involved laboratory tests which allowed to better understand the phenomenon. This new knowledge has enabled existing models to be improved.

A simple equation has been developed to calculate the flexural stresses in the bars as a function of the various parameters. This equation can be used for verifying the risk of fatigue failure of existing structures based on non-destructive in-situ measurements (without the need to remove the concrete cover and stick strain gauges on the bars).

For the ultimate limit state, the existing model based on limit analysis has been improved on the basis of the knowledge acquired from tests and a comparison of the experimental results available.

As described above, the results of the first topic have been implemented in new codes for practice. The results of the second topic can have a significant influence in the assessment of existing structures. For these reasons, the outcome of this research, which has been supported by the Swiss Federal Road Administration, has a significant practical relevance.

Lausanne, February 2024, Prof. Aurelio Muttoni

Acknowledgments

During my doctoral studies at EPFL in the Structural Concrete Laboratory IBETON, which spanned nearly five years, I had the privilege of collaborating with exceptional individuals. Their contributions, support, and assistance were invaluable, and I am deeply grateful for their help in completing this thesis. Therefore, I would like to express my special gratitude to:

The Swiss Federal Roads Authority (FEDRO) for providing the financial support within the framework of the research project AGB 2019/017. In particular, I am thankful to the committee that followed this project for their constructive and pertinent discussions.

My thesis supervisor Prof. Aurelio Muttoni for giving me an opportunity to develop my thesis at EPFL. His consistent support and insightful feedback have been instrumental in shaping my critical thinking and have significantly contributed to the successful completion of this thesis.

The jury members of my thesis Prof. Alain Nussbaumer (president), Prof. Marco di Prisco, Prof. Boyan Mihaylov and Prof. David Ruggiero for the constructive discussion and pertinent comments.

Prof. Miguel Fernández Ruiz who significantly contributed to my first scientific publication. It has been a privilege to meet and collaborate with him.

Dr Oliver Burdet for his invaluable IT support, insightful suggestions regarding laboratory work, and the numerous discussions we've had about various aspects of civil engineering.

The Structural Engineering Platform (GIS) team for the outstanding collaboration and their significant contribution to conducting my experimental campaigns. I am thankful to Gilles, Serge, Armin, Gérald, Frédérique, François, Luca and Gregory.

Yvonne Buehl-Brauch and Jessica Ritzi, our secretaries, for their amazing work, support and assistance with various tasks, especially in handling administrative duties.

My colleagues and friends at IBETON for their exceptional collaboration and engaging discussions on various topics. The time spent with them has been invaluable for both my personal and professional growth. I am therefore sincerely grateful to Enrique, Xhemi, Diego, Qianhui, Frédéric, Raffaele, Max, Patrick, Francesco, Eduardo. I am also thankful to the exchange students and post-doctoral researchers Julia, Andri, Xianlin, Mads, Daniel and Hamid.

I am particularly grateful to my family: my parents Mira and Žarko, my brother Mirko and my sister Tijana. Their love and support have made me who I am today. Also, I owe the unconditional gratitude to my lovely wife Sara for her love and wisdom.

Lausanne, February 2024

Marko Pejatović

Abstract

Codes of practice can be overly conservative, particularly for the shear resistance of reinforced concrete beams with shear reinforcement when large loads act close to supports. This thesis addresses the topic by proposing a refined design approach based on the stress field method for this type of members, with the aim to provide accurate values for the design or verification of both slender and squat members. It then goes on by presenting a model to better understand the behaviour of steel and concrete in presence of dowel action in reinforcing bars.

Consistent models based on suitable stress fields, as for example the Variable-Angle Truss models, can be used for the shear design of slender members with shear reinforcement, as proposed by Eurocode 2 (EN:1992-1-1:2004) and *fib* Model Code 2010. However, this type of approach usually neglects the contribution of direct struts for loads applied close to the supports, and thus underestimates the resistance in these cases. To account for this phenomenon, the shear resistance of slender members in design codes has typically been adjusted by empirical corrections. This thesis shows the advantages of designing these cases based on tailored stress fields, which allow a smooth transition between slender and squat members and yield more accurate predictions than empirical corrections. On that basis, simple design formulae are developed to serve as a basis for a revision for the next generation of design codes (Model Code 2020 and 2nd generation of Eurocode 2).

Reinforcing bars are commonly designed to carry axial forces, neglecting their ability to resist transverse forces by dowel action, which can occur at crack interfaces, connections between various concrete elements or between two concrete parts cast at different times. On the negative side, dowel action can affect the fatigue resistance of reinforcing bars subjected to cyclic loading, inducing stress concentrations near interfaces with relative displacements transverse to the bar.

This thesis contributes to a better understanding of dowel action by two test series. The first series focuses on the dowel response due to monotonic or low stress-level cyclic actions, with optical fibre and digital image correlation measurements. The results show the influence of the bar diameter, the imposed crack kinematics and the angle between the bar and the crack. The second test series investigates the behaviour of concrete underneath the bar due to a point load. The results show a strong dependency on position of the load along the bar.

As for the stress prediction in reinforcing bars due to dowel action, this thesis presents a new formulation for the bearing stiffness of concrete under the bar to be introduced in Winkler's model as a function of the transverse displacement. The formulation is calibrated based on mechanical considerations and optical fibre measurements. The proposed bearing stiffness leads to good predictions of both the dowel force-transverse displacement response and the peak stress in the reinforcing bar for both monotonic and cyclic tests.

Keywords: shear, direct strut, design codes, stress fields, shear reinforcement, dowel action, cracks, stress variation, digital image correlation, optical fibres, concrete bearing stiffness.

Résumé

Les normes de construction peuvent être excessivement conservatrices, surtout pour la résistance à l'effort tranchant des éléments en béton armé avec armature à l'effort tranchant lorsque des charges importantes agissent près des appuis. Cette thèse propose une approche basée sur des champs de contraintes pour la conception pour ce type d'éléments. L'objectif est de fournir des valeurs précises pour le dimensionnement et la vérification des éléments aussi bien élancés que trapus. Elle présente également un modèle pour comprendre le comportement de l'acier et du béton en présence d'effet goujon dans les barres d'armature.

Certains modèles basés sur des champs de contraintes, comme les treillis à angles variables, peuvent être utilisés pour le calcul de l'effort tranchant des éléments élancés avec armature à l'effort tranchant, comme proposé par l'Eurocode 2 et le *fib* Model Code 2010. Cependant, ces approches négligent la contribution de l'appui direct pour les charges agissant près des appuis, conduisant à une sous-estimation de la résistance. Pour tenir compte de l'appui direct, les normes ont souvent été ajustées par des corrections empiriques pour la vérification de la résistance à l'effort tranchant d'éléments élancés. Cette thèse montre les avantages d'une conception basée sur des champs de contraintes adaptés, permettant une transition entre éléments élancés et trapus, avec des prédictions plus précises. Sur cette base, des formules de dimensionnement simples sont développées, pour être introduites dans les prochaines générations de normes (Model Code 2020 et 2^{ème} génération de l'Eurocode 2).

Les barres d'armature sont généralement dimensionnées pour reprendre des efforts longitudinaux, en négligeant leur capacité à reprendre des efforts transversaux par effet goujon. Cet effet peut se produire à proximité des fissures, à l'interface entre divers éléments de béton, etc. L'effet goujon peut influencer négativement la résistance à la fatigue des barres d'armature soumises à des charges cycliques, en provoquant des concentrations de contraintes près des interfaces avec des déplacements relatifs transversaux par rapport à la barre.

Cette thèse contribue à une meilleure compréhension de l'effet goujon par deux séries d'essais. La première se concentre sur la réponse des goujons sous des actions monotones ou cycliques à faible niveau de contrainte, avec des mesures par fibre optique et corrélation d'images numériques. Les résultats montrent l'influence du diamètre de la barre, de la cinématique de la fissure et de l'angle entre la barre et la fissure. La deuxième série d'essais examine le comportement du béton sous la barre soumis à une charge ponctuelle. Les résultats montrent une forte dépendance de la position de la charge le long de la barre.

Pour la prédiction des contraintes dans les barres d'armature dues à l'effet goujon, cette thèse présente une nouvelle formulation de la rigidité du béton sous la barre, qui peut être introduite dans un modèle de Winkler, en fonction du déplacement transversal. La formulation est calibrée sur la base de considérations mécaniques et de mesures par fibre optique. La rigidité proposée conduit à des prédictions précises de la réponse en force de l'effort tranchant-déplacement

transversal et de la contrainte maximale dans la barre d'armature pour les essais monotones et cycliques.

Mots clés : effort tranchant, appui direct, normes, champs de contraintes, armature d'effort tranchant, effet goujon, fissures, variation de contrainte, corrélation d'images numériques, fibres optiques, rigidité du béton sous la barre.

Abstrakt

Norme za projektovanje mogu biti previše konzervativne, posebno za smičuću čvrstoću armirano-betonskih greda sa armaturom na smicanje kada značajne sile djeluju blizu oslonaca. Ova doktorska teza predlaže detaljan pristup projektovanju zasnovan na metodi polja napona za ovu vrstu elemenata, sa ciljem da obezbedi precizne rezultate za projektovanje i verifikaciju kako vitkih tako i zdepastih elemenata. Ova teza dalje prezentuje i model za bolje razumijevanje ponašanja čelika i betona usled efekta moždanika u armaturnim šipkama.

Konzistentni modeli zasnovani na poljima napona, kao što su modeli rešetke sa promjenljivim nagibom pritisnutog polja, mogu se koristiti za projektovanje vitkih elemenata sa armaturom na smicanje, kao što je predloženo u Evrokodu 2 (EN:1992-1-1:2004) i *fib*-ovom Model Kodu 2010. Ovakav pristup međutim zanemaruje doprinos direktnog štapa u slučaju sila blizu oslonaca, i na taj način podcjenjuje čvrstoću u ovim slučajevima. Da bi se ovaj fenomen uzeo u obzir, čvrstoća na smicanje vitkih elemenata u normama za projektovanje je obično prilagođena empirijskim korekcijama. Ova teza pokazuje prednosti projektovanja ovih slučajeva koristeći odgovarajuća polja napona, koja omogućavaju tranziciju između vitkih i zdepastih elemenata i koja daju preciznije predikcije smičuće čvrstoće od empirijskim korekcija. Na osnovu toga, jednostavne jednačine za projektovanje su razvijene i služe kao osnova za reviziju sledeće generacije normi za projektovanje (Model Kod 2020 i druga generacija Evrokoda 2).

Armaturne šipke se obično dimenzionišu na aksijalne sile, zanemarujući njihovu sposobnost da nose poprečne sile efektom moždanika koji se može javiti na prslinama, konekcijama između različitih betonskih elemenata ili između dva betonska elementa betonirana u različito vrijeme. Sa negativne strane, efekat moždanika može negativno uticati na čvrstoću na zamor armaturnih šipki podvrgnutim cikličnom opterećenju, izazivajući koncentracije napona u blizini prslina ili konekcija sa relativnim pomjeranjem poprečnog na osu šipke. Ova teza doprinosi boljem razumijevanju efekta moždanika pomoću dvije serije testova. Prva serija se fokusira na ponašanje moždanika usled monotonog i cikličnog opterećenja malog intenziteta. Rezultati pokazuju uticaj prečnika šipke, aplicirane kinematike prsline i ugla između šipke i prsline. Druga serija testova ispituje ponašanje betona ispod šipke usled koncentrisane sile. Rezultati pokazuju snažnu zavisnost od položaja sile duž šipke.

Što se tiče predikcije napona u armaturnim šipkama usled efekta moždanika, ova teza prezentuje novu formulaciju za krutost betona ispod šipke koja se koristi u Vinklerovom modelu kao funkcija poprečnog pomjeranja. Ova formulacija je kalibrisana na osnovu mehaničkih razmatranja i mjerenja optičkim vlaknima. Predložena krutost betona daje dobre predikcije kako za odgovor moždanika u odnosu na smičuću silu u funkciji od poprečnog pomjeranja, tako i za maksimalni napon u šipki i u monotonim i u cikličnim testovima.

Ključne riječi: smicanje, direktni štap, norme za projektovanje, polje napona, armatura na smicanje, efekat moždanika, prsline, varijacija napona, digitalna korelacija fotografija, optička vlakna, krutost betona.

Riassunto

Per quanto riguarda la resistenza a taglio di travi in calcestruzzo armato con armatura a taglio, le normative attuali possono essere eccessivamente conservative quando grandi carichi agiscono in prossimità degli appoggi. Lo scopo di questa tesi è di proporre un approccio progettuale raffinato basato sul metodo dei campi di tensione per questo tipo di elementi. L'obiettivo è quello di fornire valori accurati per la progettazione e la verifica sia di elementi snelli che tozzi. Inoltre si presenta un modello per comprendere meglio il comportamento dell'acciaio e del calcestruzzo in presenza dell'azione di spinotto nelle barre di armatura.

Modelli coerenti basati su campi di tensione adeguati, come ad esempio i modelli a traliccio ad angolo variabile, possono essere utilizzati per la progettazione a taglio di membrature snelle con armatura a taglio, come proposto dall'Eurocodice 2 (EN:1992-1-1:2004) e dal *fib* Model Code 2010. Tuttavia, questo tipo di approccio solitamente trascura il contributo dell'appoggio diretto per i carichi applicati in prossimità degli appoggi, e quindi sottostima la resistenza in questi casi. Per tenere conto di questo fenomeno, la resistenza a taglio degli elementi snelli nelle normative è stata in genere corretta in modo empirico. Questa tesi mostra i vantaggi di progettare questi elementi sulla base di campi di tensione adattati, i quali consentono una transizione graduale tra elementi snelli e tozzi, fornendo previsioni più accurate rispetto alle correzioni empiriche. Su questa base, vengono sviluppate semplici formule di verifica che serviranno come base per una revisione della prossima generazione di normative (Model Code 2020 e seconda generazione dell'Eurocodice 2).

Le barre d'armatura sono comunemente progettate per lavorare con sforzi assiali, trascurando la loro capacità di resistere a forze trasversali sotto l'azione di spinotto, che può verificarsi all'interfaccia delle fessure, alle connessioni tra vari elementi in calcestruzzo o tra due parti in calcestruzzo gettate in tempi diversi. Lo svantaggio è che l'azione di spinotto può influire sulla resistenza a fatica delle barre d'armatura che sono sottoposte a carichi ciclici, inducendo concentrazioni di tensione in prossimità delle interfacce con spostamenti relativi trasversali alla barra.

Questa tesi contribuisce a migliorare la comprensione dell'azione di spinotto attraverso due serie di test. La prima serie si concentra sulla risposta sotto azioni monotone o cicliche con bassi livelli di tensione, con misure eseguite utilizzando fibre ottiche e correlazione di immagini digitali. I risultati mostrano l'influenza del diametro della barra, della cinematica della fessura imposta e dell'angolo tra la barra e la fessura. La seconda serie di prove studia il comportamento del calcestruzzo sotto la barra soggetto ad un carico puntuale. I risultati mostrano una forte dipendenza dalla posizione del carico lungo la barra.

Riguardo la valutazione dello stress nelle barre di armatura dovute all'azione di spinotto, questa tesi presenta una nuova formulazione per la rigidità del calcestruzzo sotto la barra da introdurre nel modello di Winkler in funzione dello spostamento trasversale. La formulazione è calibrata sulla base di considerazioni meccaniche e di misure con fibre ottiche. La formulazione della

rigidezza proposta porta a una buona stima sia della risposta della forza di spinotto allo spostamento trasversale, sia della tensione di picco nella barra di armatura sia per prove monotone che cicliche.

Parole chiave: taglio, appoggio diretto, normative per le costruzioni, campi di tensione, armatura a taglio, azione di spinotto, fessure, variazione di tensione, correlazione digitale di immagini, fibre ottiche, rigidità portante del calcestruzzo.

Resumen

Las normas de diseño de estructuras pueden ser excesivamente conservadoras, en particular para la resistencia a cortante de vigas de hormigón con armadura de cortante cuando actúan grandes cargas cerca de los apoyos. Esta tesis aborda este tema proponiendo un procedimiento de diseño refinado basado en el método de los campos de tensiones, con el objetivo de proporcionar valores precisos para el diseño o la verificación de miembros tanto esbeltos como compactos. La segunda parte de la tesis presenta un modelo para comprender mejor la interacción entre las barras de armadura y el hormigón como resultado del efecto pasador.

Los modelos basados en campos de tensiones, como por ejemplo los modelos de celosía de ángulo variable, pueden utilizarse para el cálculo de la resistencia a cortante de elementos esbeltos con cercos, tal y como proponen el Eurocódigo 2 (EN:1992-1-1:2004) y el Código Modelo de 2010 de la *fib*. Sin embargo, este tipo de modelos suele despreciar la contribución de las bielas directas para cargas aplicadas cerca de los apoyos y, por tanto, subestima la resistencia en estos casos. Para tener en cuenta este fenómeno en las normas actuales, la resistencia a cortante de los elementos esbeltos se ha ajustado mediante factores de corrección empíricos. Esta tesis muestra las ventajas de diseñar estos elementos usando campos de tensiones, ya que permiten una transición progresiva entre elementos esbeltos y compactos, al mismo tiempo que proporcionan predicciones más precisas que las correcciones empíricas (Código Modelo de 2020 y 2ª generación del Eurocódigo 2).

Las barras de armadura suelen diseñarse para resistir solicitaciones axiales, olvidando su capacidad para resistir solicitaciones de cortante debidas al efecto pasador. Éstas pueden producirse en las fisuras, en las conexiones entre elementos de hormigón o entre dos elementos hormigonados en momentos diferentes. Esta combinación de solicitaciones puede tener un efecto negativo en la resistencia a la fatiga de las barras sometidas a cargas cíclicas, ya que generan concentraciones de tensiones cerca de las interfaces donde se producen los desplazamientos transversales a la barra.

Esta tesis contribuye a una mejor comprensión del efecto pasador mediante dos series de ensayos. La primera serie se centra en el comportamiento de las barras debido a solicitaciones transversales monotónicas y cíclicas para niveles de tensiones bajos, utilizando mediciones con fibra óptica y correlación digital de imágenes. Los resultados muestran la influencia del diámetro de la barra, la cinemática de la fisura y el ángulo entre la barra y la fisura. La segunda serie de ensayos investiga el comportamiento del hormigón bajo la barra debido a una carga puntual. Los resultados muestran una fuerte dependencia de la posición de la carga a lo largo de la barra.

En cuanto a la predicción de tensiones en la barra debidas al efecto pasador, esta tesis presenta una nueva formulación de la rigidez del hormigón bajo la barra que depende del desplazamiento transversal, para su uso en el modelo de Winkler. La formulación ha sido calibrada en base a consideraciones mecánicas y resultados experimentales de las fibras ópticas. La rigidez

propuesta conduce a buenas predicciones tanto de la relación entre la fuerza y el desplazamiento transversal como de la tensión máxima en la barra para ensayos monotónicos y cíclicos.

Palabras clave: cortante, biela directa, códigos de diseño, campos de tensiones, armadura de cortante, efecto pasador, fisura, variación de tensiones, correlación digital de imágenes, fibra óptica, rigidez del hormigón.

摘要

现行规范中对于有腹筋梁的条款可能过于保守，特别是当较大的荷载作用于支座附近的位置时。针对此类构件，本文提出了一种基于应力场的改良设计方法，可为高剪跨比以及低剪跨比的构件提供更准确的抗剪设计和校验。本文继而提出了一个更好地解释加劲钢筋销栓效应中钢筋和混凝土作用的模型。

基于适宜的应力场的设计模型，例如变角度桁架模型，可被用于高剪跨比含腹筋构件的抗剪设计。Eurocode 2 (EN:1992-1-1:2004) 以及 *fib Model Code 2010* 均采纳了此类模型。然而，此类模型通常忽略了当荷载作用于支座附近时，直接压杆传力模式对抗剪的贡献，因而低估了此类作用下构件的承载力。为了计入此现象的影响，规范中对于高剪跨比构件的抗剪模型通常计入了基于经验的修正系数。本文展示了使用适宜的应力场方法分析此类构件的优势。本文所提出的应力场模型允许从低到高剪跨比构件的平滑过渡，并且提供了比经验模型更准确的抗力评估。基于此模型，本文亦提出了相应的简化的设计公式，可被用于新一代的设计规范 (*Model Code 2020* 以及第二代 Eurocode 2) 中相应条款的修订。

混凝土结构中的钢筋通常被用于承载轴向力，而其因销栓效应而对横向承载力的贡献通常被忽略不计。销栓效应的贡献通常在裂缝界面、混凝土构件的连接处以及浇筑时间不同的混凝土界面上发展。但另一方面，销栓效应也可能对钢筋在循环荷载作用下的抗疲劳性能有负面影响，因为销栓效应会在钢筋存在相对横向位移的界面引发应力集中。

本研究通过两个系列试验对销栓效应进行了深入研究。第一个系列试验着重于研究在单调荷载和低应力循环荷载作用下的销栓效应。本实验采用了光纤传感测量和数字图像相关 (DIC) 等先进量测技术。试验结果表明，钢筋的直径、被动施加的裂缝发展模式以及钢筋与裂缝方向之间的夹角都会对销栓效应造成影响。第二个系列试验研究了钢筋下方混凝土在集中力作用下的响应。结果表明其响应取决于荷载在钢筋上的施力位置。

针对销栓效应在钢筋中引起的应力分析，本文提出了一个新的基于横向位移的钢筋下混凝土刚度的计算公式。该公式可被引入到温克勒模型 (*Winkler's model*) 中，对销栓效应在钢筋中引起的应力进行分析。在力学分析和光纤量测数据基础上，对该公式进行了参数校准。引入该公式的刚度分析后，实现了对单调试验和循环试验中的锚固力-横向位移响应以及钢筋中的峰值应力的准确预测。

关键词：剪力，直接压杆传力，设计规范，应力场，腹筋，销栓效应，裂缝，应力变化，数字图像相关技术，光纤传感测量，混凝土承载刚度

Contents

Foreword	i
Acknowledgments	iii
Abstract	v
Résumé	vii
Abstrakt	ix
Riassunto	xi
Resumen	xiii
摘要	xv
Chapter 1 Introduction	1
1.1 Context and motivation	1
1.2 Scientific contributions.....	6
1.3 Structure of the thesis.....	7
1.4 List of publications.....	8

**Chapter 2 Design of slender and squat reinforced concrete members
with shear reinforcement 9**

Abstract..... 10

2.1 Introduction..... 10

2.2 Suitable stress fields for slender and squat members 15

 2.2.1 Influence of slenderness on the mechanical response of concrete members..... 15

2.3 Stress fields accounting for direct strutting conditions 18

 2.3.1 Stress Fields with concentrated strut (CSSF) (LoA I, II) 18

 2.3.2 Stress Fields with spreading strut (SSSF) (LoA III)..... 23

**2.4 Performance of the considered shear models with respect to the extended and
reduced databases 25**

2.5 Conclusions 27

Appendix 2.A: Refined approach of CSSF (LoA II) 29

Appendix 2.B.1: SSSF with full spreading (LoA III) 30

Appendix 2.B.2: SSSF with partial spreading (LoA III) 32

Appendix 2.C 34

Nomenclature..... 40

Chapter 3 Experimental investigation of dowel action in reinforcing bars using refined measurements 43

Abstract..... 45

3.1 Introduction..... 45

3.2 Experimental programme..... 48

 3.2.1 Specimens and test set-ups..... 49

 3.2.2 Material properties 51

 3.2.3 Measurements 53

3.3 Experimental results..... 54

 3.3.1 Monotonic dowel tests 54

 3.3.2 Cyclic dowel tests 62

 3.3.3 CP test series 66

3.4 Comparison with existing models..... 69

 3.4.1 Concrete stiffness at the serviceability limit state..... 69

 3.4.2 Ultimate resistance 70

3.5 Conclusions..... 73

Appendix 3.A: Failure pattern of DP test series..... 74

Appendix 3.B: Optical fibre measurements of DP series 75

Appendix 3.C: Spalling pattern at peak load in CP tests 79

Nomenclature 80

Chapter 4 Steel stresses and shear forces in reinforcing bars due to dowel action 83

Abstract	84
4.1 Introduction	84
4.2 Steel stresses and shear force in the bar according to Winkler’s model	87
4.2.1 Analytic solution for the symmetric case	87
4.2.2 Existing models for the bearing stiffness of concrete.....	89
4.3 Improved expression for the bearing stiffness	91
4.3.1 General formulation, influence of angle θ and of imposed displacement	91
4.3.2 Influence of the casting conditions, concrete cover, and direction of the dowel force	94
4.3.3 Influence of the concrete strength	98
4.3.4 Interaction with bond.....	99
4.3.5 Influence of the number of cycles	99
4.3.6 Solution of Winkler’s equation for different bearing stiffness on opposite sides of the crack	100
4.4 Validation of the enhanced expression for the bearing stiffness k_c	102
4.5 Conclusions	107
Appendix 4.A: Solution of Winkler’s model for an asymmetric case with different bearing stiffness on opposite sides of the crack	108
Nomenclature	111

Chapter 5 A contribution to predicting the dowel resistance 113

5.1 Rasmussen’s model	114
5.1.1 Solution of Rasmussen’s model	114
5.1.2 Enhancement of Rasmussen’s model and validation	116
5.2 Conclusions	118
Nomenclature	119

Chapter 6 Conclusions and Outlook	121
6.1 Conclusions.....	121
6.2 Outlook and future works.....	125
Bibliography	129
Curriculum Vitae	141

Chapter 1

Introduction

1.1 Context and motivation

The shear behaviour of reinforced concrete structures presents several challenges because it involves complex phenomena. Over the years, most of these phenomena have been clarified and the corresponding load-carrying actions have been formalised, providing engineers with analytical expressions for both the design of new and the assessment of existing structures. However, commonly used expressions, as found in codes of practice, sometimes yield overly conservative results. This is particularly the case of the shear resistance of members with shear reinforcement subjected to large loads on the upper chord near the supports, where a direct strut develops in concrete. In this context, developing more accurate models of the shear behaviour is essential to minimize the material usage, reduce the maintenance and their associated costs. In a similar manner, the local bending of reinforcing bars due to dowel action, a load-carrying mechanism which is often neglected, can lead to stress concentrations which can potentially lead to fatigue failures. This thesis addresses these two relatively distant topics: the shear design of reinforced concrete members with shear reinforcement based on the stress field approach, and the dowel action of reinforcing bars embedded in concrete.

Design of slender and squat members with shear reinforcement using stress fields

The stress field method is a consistent tool for the design and assessment of concrete structures [Mut96, Nik17, Kos09, Fer07]. Based on equilibrium and yield conditions, it provides safe predictions of the load-carrying capacity according to the lower-bound theorem of limit analysis [Fer07, Dru61, Nie11]. The stress field method is especially advantageous for designing new structures, enabling designers to select the most appropriate load-carrying actions. For the assessment of existing structures, if the considered stress field is compatible with the admissible failure mechanism (upper-bound solution of limit analysis), the exact solution of the load-carrying capacity according to limit analysis can be calculated [Jen79, Jen81, Jen78, Nie11].

The initial development of stress fields considered a rigid-plastic response of the materials [Mut96], which allowed for simple manual calculations and the selection of the suitable load-carrying actions. More refined solutions are also possible for the assessment of existing structures according to the Levels-of-Approximation approach [FIB21]. In the rigid-plastic analysis, to account for the cracking in concrete, a constant strength reduction factor of concrete v is typically adopted [Mut96, Vec86] based on strain conditions in the member. To be applicable, this approach requires a minimum amount of shear reinforcement to ensure a smeared development of cracking [Mon22].

The shear design of slender members is based on stress fields, as proposed by several codes of practice [FIB13, Eur04, ACI08, SIA13]. This is for example the case of the Variable-Angle Truss models (VAT) which are based on the acting shear force in equilibrium with an inclined compression field and the longitudinal and transverse reinforcement in tension (Fig. 1.1a). Based on the VAT models and rigid-plastic stress fields, simple design expressions have been incorporated into codes of practice, such as Eurocode 2 EN 1992-1-1:2004 [Eur04] and *fib*'s MC 2010 [FIB13]. This approach provides accurate predictions of the resistance for slender beams. However, it yields overly conservative results in the case of gravity loads applied on the upper chord near the supports, because it neglects the development of a direct strut in the concrete between the load and the support (Fig. 1.1b). This strut leads to a more favourable cracking state and thus to a larger shear resistance. This was recognised and empirical corrections of the shear resistance of slender members were introduced for the design of members with a large contribution of the direct strut. Unfortunately, these empirical corrections are mechanically inconsistent and can be overly conservative. This thesis investigates the shear design of various reinforced concrete members using the stress field method through various Levels-of-Approximation (LoA). The transition between squat and slender members as well as the main load-carrying actions are analysed using the most refined approach (the Elastic-Plastic Stress Fields, EPSF) [Fer07] which provide exact solutions according to the limit analysis. On that basis, simplified Rigid-Plastic Stress Fields are proposed for the design accounting for the direct strut. In addition, a consistent approach to evaluate the associated strength reduction factors accounting for compatibility of deformations is presented. The proposed expressions are simple to use, and are a basis for the revision for the next generation of design codes (Model Code 2020 and 2nd generation of Eurocode 2).

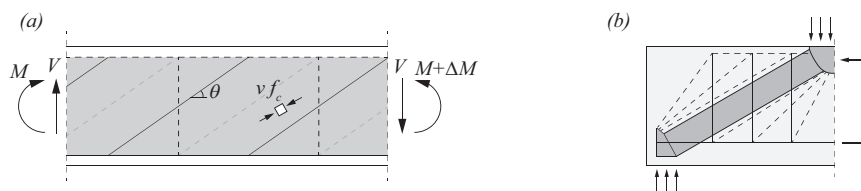


Figure 1.1: Design of slender and squat members: (a) slender member (VAT approach) and (b) direct strut action.

Dowel action in reinforcing bars

Reinforcing bars are typically designed to carry axial forces and their ability to resist transverse forces (by dowel action) due to their bending stiffness is neglected to simplify the structural design. Dowel action can be accounted for at the ultimate limit state in cases when it contributes to the resistance, for instance, in connections of precast elements (Fig. 1.2c), at the interface between two concrete parts cast at different times (Fig. 1.2b), etc. On the negative side, dowel action can have a negative impact on the fatigue life due to associated additional longitudinal bending stresses in the reinforcing bars. These stresses are induced by a relative crack displacement component transverse to the bar axis, resulting from the sliding of the crack perpendicular to the bar, and the opening and sliding of a crack inclined with respect to the bar (Fig. 1.2a,f).

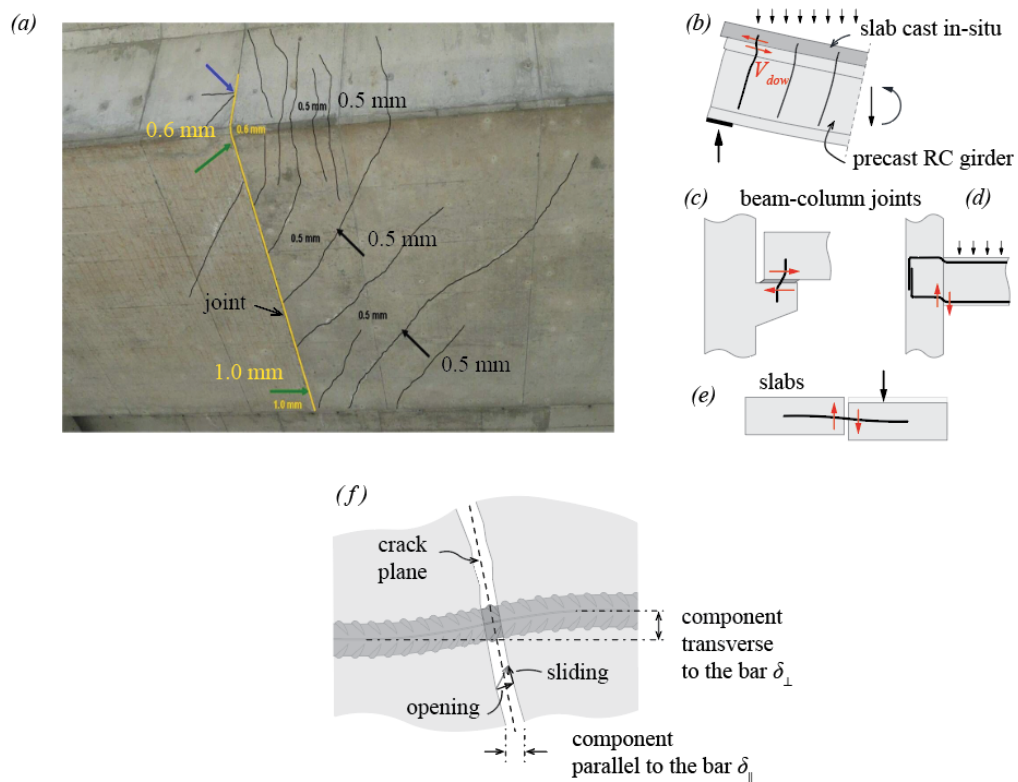


Figure 1.2: (a) Cracks due to torsion in the Weyermannshaus Viaduct (Bern, Switzerland); (b-e) other cases where dowel action can occur and (f) components of the crack kinematics.

Typically, the fatigue verification in presence of dowel action can be based on an estimate of the crack kinematics and a model of the dowel action giving an estimate of the stresses as a function of the imposed deformations, accounting for the interaction between the reinforcing bar and the surrounding concrete. For the assessment of existing structures, in-situ measurements could also be used, for example using strain gauges or fibre optics [Can20, Cor23, Bad21, Mon21] in the

reinforcement. Unless these devices were placed before casting of concrete, this approach is invasive because it involves removing the concrete cover, which disrupts the local bond and dowel behaviour. Alternatively, in-situ measurements of strains and crack movements at the surface of the concrete using image recognition and correlation techniques [Can21] can be used without invasive action. In this case, a model enabling to predict the stresses in reinforcing bars based on the measured crack kinematics is required.

If the concrete cover is not strong enough, spalling of the concrete cover tends to limit the dowel force, and consequently the steel stresses [Vin86]. Conversely, when the cover is strong, substantial stresses in the reinforcing bars can occur, causing plastic hinges in the reinforcement due to localized bending combined with localized concrete crushing beneath the bar near the crack (or the interface between concrete parts cast at different times). This type of failure results in a relatively ductile behaviour due to the potentially large steel plastic strains. Consequently, numerous authors have evaluated the dowel resistance of a steel bar using the limit analysis approach (see Rasmussen [Ras62] and [Sor86, Dul72, Dei87, Dei92, Tan11, Pru88, Nør15, Vin87]). The presence of an axial force in the bar was observed to reduce the dowel resistance [Sha69, Kem77, Tak19, Mae96, Mae96]. In addition, the dowel resistance decreases when the angle between the bar and the crack decreases [Dul72]. Experimental investigations of the dowel behaviour under imposed cyclic loading [Ele74, Sta77, Jim79] typically indicated an increase of the shear displacement with cycles, a substantial degradation of the stiffness, and a reduction of the area of hysteresis loops over cycles.

A better understanding of the phenomenology of dowel action in a strong concrete embedment is needed. This particularly concerns the contribution of dowel action to carry shear forces and its impact on stress variations in reinforcing bars, which can potentially lead to a decrease in fatigue life.

To that aim, this thesis presents a contribution to a better understanding of dowel action by two test series. The first series investigates the dowel behaviour using the concrete specimens with embedded bars subjected to monotonic or low stress-level cyclic actions. The measurements included optical fibres on the surface of the reinforcement and digital image correlation on the concrete surface. The tests typically finished with the development of the full plastic capacity of the dowel and a rupture due to catenary action. The results are strongly influenced by: the bar diameter, the imposed crack kinematics and the angle between the bar and the crack. The second test series focuses on the behaviour of concrete underneath a bar subjected to a point load. The results show a strong dependency on the position of the load along the bar.

For the fatigue verifications, it is crucial to accurately estimate the stresses in the reinforcement due to dowel action as a function of the associated imposed transverse displacement. In that context, this thesis presents an improvement of the model by Winkler, introducing a new formulation for the bearing stiffness of concrete under the bar, calibrated based on mechanical considerations and measurements with optical fibres. The formulation accounts for various effects: bar diameter, concrete strength, angle between the crack and the bar, casting conditions,

thickness of the concrete cover, number of load cycles and local secondary cracks in concrete near the ribs due to the axial force. The results of the improved model are in good agreement with monotonic and cyclic tests, both for the shear force-transverse displacement response and for the peak stress in the reinforcing bar. Additionally, the case of asymmetric behaviour on both sides of the crack, which typically results from bleeding and settlement of fresh concrete as well as the presence of a free concrete surface near the bar, is investigated analytically.

1.2 Scientific contributions

The main scientific contributions of this thesis are:

- Development of suitable stress fields including a concentrated direct strut to determine the load-carrying capacity of squat reinforced concrete members with shear reinforcement.
- Calibration of the strength reduction factor accounting for the cracking state of concrete for slender and squat members with shear reinforcement. This factor and the stress fields accounting for the concentrated direct strut are implemented in the next generation of design codes (Model Code 2020 and 2nd generation of Eurocode 2).
- Development of suitable stress fields accounting for the full and partial spreading of the direct strut to estimate the load-carrying capacity of squat reinforced concrete members with shear reinforcement.
- Investigation of the shear failure mechanisms and the main load-carrying actions in squat and slender members with shear reinforcement using the Elastic-Plastic Stress Fields (EPSF).
- Establishment of a database of 463 tests of members with shear reinforcement failing in shear with various material and geometrical properties, including various shear slendernesses.
- Experimental programme comprising dowel tests on 11 specimens subjected to monotonic or low stress-level cyclic actions to investigate the influence of the diameter of the bar, the imposed crack kinematics and the angle between the bar and the crack.
- Refined measurements with optical fibres of strains in the reinforcing bar to investigate the dowel behaviour and the distribution of internal forces in the bar.
- Experimental programme comprising compression tests of concrete underneath the reinforcing bar of 9 specimens to investigate the concrete behaviour due to a point load introduced at various locations into concrete through a reinforcing bar.
- Refined measurements based on the digital image correlation of the concrete surface underneath the bar to investigate the concrete behaviour.
- Establishment of a database of 142 dowel tests failing with plastic hinges and concrete crushing to evaluate the existing dowel models for the resistance prediction.
- Proposal of a new formulation for the concrete bearing stiffness to be used in the model by Winkler. It is calibrated based on mechanical considerations and optical fibre measurements, accounting for various effects in real-life structures.

- Proposal of a new concrete confinement factor to be used in the model by Rasmussen. This factor is calibrated based on optical fibre measurements accounting for various angles between the crack and the bar.

1.3 Structure of the thesis

This thesis consists of the following chapters:

- **Chapter 1: *Introduction***

Context and motivation, scientific contributions and list of publications.

- **Chapter 2: *Design of slender and squat reinforced concrete members with shear reinforcement***

Simple design expressions based on tailored stress fields are formulated in an effort to serve as a revision for the next generation of design codes (Model Code 2020 and 2nd generation of Eurocode 2).

- **Chapter 3: *Experimental investigation of dowel action in reinforcing bars using refined measurements***

Dowel tests and compression tests of concrete underneath the bar are conducted using measurements with optical fibres and digital image correlation.

- **Chapter 4: *Steel stresses and shear forces in reinforcing bars due to dowel action***

A new formulation for the concrete bearing stiffness to be used in Winkler's model is proposed based on mechanical considerations and measurements with optical fibres. Additionally, the case of asymmetric behaviour on both sides of the crack is investigated analytically.

- **Chapter 5: *A contribution to predicting the dowel resistance***

A new confinement factor to be used in Rasmussen's model is proposed accounting for various angles between the bar and the crack.

- **Chapter 6: *Conclusions and outlook***

Conclusions of this thesis and the outlook on the potential future work.

The Chapters 2 to 4 contain their own introductions, literature review (state-of-the art), conclusions, appendixes and notations as this thesis is based on journal publications. The complete bibliography is given at the end of the thesis.

1.4 List of publications

This thesis was developed at the Structural Concrete Laboratory (IBETON) of the Swiss Institute of Technology of Lausanne (Ecole Polytechnique Fédérale de Lausanne, EPFL), leading to the following publications:

- **Pejatović M., Fernández Ruiz M., Muttoni A.**, *Design of slender and squat reinforced concrete members with shear reinforcement*, Structural Concrete, 17 p., 2022.
DOI: <https://doi.org/10.1002/suco.202200887>
- **Pejatović M., Muttoni A.**, *Experimental investigation of dowel action using advanced measurement techniques*, 14th fib International PhD Symposium in Civil Engineering, pp. 573-580, Rome, Italy, 2022.
- **Pejatović M., Muttoni A.**, *Experimental investigation of dowel action in reinforcing bars using refined measurements*, Structural Concrete, 2024 [submitted, December 2023]
- **Pejatović M., Muttoni A.**, *Steel stresses and shear forces in reinforcing bars due to dowel action*, 2024 [publication in preparation]

Chapter 2

Design of slender and squat reinforced concrete members with shear reinforcement

This chapter is a post-print version of the following publication:

Pejatović M., Fernández Ruiz M., Muttoni A., *Design of slender and squat reinforced concrete members with shear reinforcement*, Structural Concrete, 17 p., 2022.

<https://doi.org/10.1002/suco.202200887>

The authors of this publication are Marko Pejatović (PhD candidate), Prof. Miguel Fernández Ruiz (Universidad Politécnica de Madrid, Spain) and Prof. Aurelio Muttoni (thesis director, École Polytechnique Fédérale de Lausanne, Switzerland).

This work was conducted by the first author (Marko Pejatović) under the supervision of Prof. Miguel Fernández Ruiz and Prof. Aurelio Muttoni who consistently offered the constructive feedback, proofreading, and manuscript revisions.

The main contributions of Marko Pejatović to this publication and chapter are the following:

- Elaboration of suitable stress fields accounting for the concentrated direct strut, the direct strut with the full and partial spreading for squat reinforced concrete members with shear reinforcement.
- Collection of the database with 463 shear tests of members with shear reinforcement with various material and geometrical properties used to validate the considered models.
- Investigation of the shear failure of squat and slender members with the shear reinforcement using the Elastic-Plastic Stress Fields (EPSF).
- Calibration of the strength reduction factor based on the collected database.
- Elaboration of the figures and tables included in the publication and writing of the manuscript of the publication.

Abstract

As proposed in several design standards for structural concrete, including Eurocode 2 (EN:1992-1-1:2004) and *fib's* Model Code 2010, the shear design of slender members with shear reinforcement can be performed by means of consistent models based on suitable stress fields. This is for instance the case of the variable-angle truss models, where the acting shear force is equilibrated by an inclined compression field and the shear reinforcement in tension. The application of such design expressions to squat members or when gravity loads are applied on the upper chord near to the supports, has however been observed to lead to overly conservative results. This is due to the fact that a direct strut can develop in the concrete between the load and the support without the need of being suspended through shear reinforcement. In addition, this leads to a more favourable cracking state and thus to enhanced shear resistance. Despite the fact that such phenomena can be also formulated in a consistent manner with the stress field method, empirical corrections of the resistance of slender members have traditionally been adopted to design beams when significant loads act close to supports. In this chapter, the benefits of designing such cases on the basis of tailored stress fields are demonstrated. Such an approach provides a smooth transition between slender and squat members and, when compared to tests, leads to a significantly lower Coefficient of Variation than empirical corrections. On that basis, simple design expressions are formulated in an effort to serve as a revision for the next generation of design codes (Model Code 2020 and 2nd generation of Eurocode 2).

Keywords: design codes, direct support, D-regions, shear reinforcement, stress fields

2.1 Introduction

Stress fields are comprehensive and consistent tools for design and assessment of concrete structures [Mut96, Nik17, Kos09, Fer07]. Based on equilibrium and yield conditions, the stress field method provides safe estimates of the load-carrying capacity according to the lower-bound theorem of limit analysis [Fer07, Dru61, Nie11]. This approach is particularly convenient for the design of new structures, allowing a designer to select the most suitable load-carrying actions. In addition, provided that the resulting stress field is compatible with an admissible failure mechanism (upper-bound solution of limit analysis), it can also be used to calculate exact solutions of the load-carrying capacity according to limit analysis [Jen79, Jen81, Jen78, Nie11]. Such stress fields are thus also valuable tools for the assessment of existing structures, providing the load-bearing capacity of a structure and allowing for verification of detailing comprising the force that should be anchored by the longitudinal reinforcement at the support.

Stress fields were originally developed considering a rigid-plastic response of the materials [Mut96]. This enables the simple hand-made calculations, allowing to select the most convenient load-carrying actions and to design the member accordingly. Also, more refined

solutions can be developed upon need, as for the assessment of existing structures following the Levels-of-Approximation approach [FIB21]. Since cracking of concrete reduces its effective compressive strength [Vec86, Bre63, Vec04, Bet18], a constant strength reduction factor of concrete ν is usually adopted in rigid-plastic analyses depending on the expected strain conditions of the member [Mut96, Vec86]. This approach can be applied provided that the member has a minimum amount of transverse reinforcement to ensure a smeared development of cracking [Mon22]. A more refined estimate of the shear resistance can be obtained by assuming a simplified strain state and by calculating the strength reduction factor using semi-empirical expressions [Vec86, Sig11, FIB13]. Recently, the use of the finite element method has opened the possibility to develop stress fields accounting for compatibility conditions, allowing for refined estimates of the strength reduction factors associated to concrete cracking and also for automatic calculation of exact solutions [Nik17, FIB21].

Accounting for its generality and consistency, the design for shear of slender members based on stress fields has been incorporated into several codes of practice [FIB13, Eur04, ACI08, SIA13] as the Variable-Angle Truss models (VAT). VAT models (see Fig. 2.1, Fig. 2.2a) are based on the equilibrium of an inclined compression field (assuming that concrete carries only compression stresses) and the shear reinforcement (carrying only tensile forces). In this case, the shear resistance can be governed by three failure conditions as sketched in Fig. 2.1. In this Figure, the ordinate represents the shear stress resistance τ_R (equal to the shear force V_R divided by the width of the web b_w and the flexural lever arm z) normalized by the concrete uniaxial compressive strength f_c whereas the abscissa shows the shear reinforcement ratio ($\rho_w = A_{sw} / (b_w \cdot s)$, where A_{sw} is the area of a shear reinforcement unit and s is its spacing) multiplied by the ratio between the yield strength of the shear reinforcement f_y and the concrete uniaxial strength f_c .

With respect to the three regimes, the latter (regime III) refers to concrete crushing at an angle of 45° without yielding of the shear reinforcement. The second (regime II) refers to simultaneous crushing of the compression field and yielding of the shear reinforcement. With respect to the regime I, it governs for low amounts of shear reinforcement and is related to the minimum angle of the compression field θ_{min} which can be activated consistently with the considered strength reduction factor associated to the cracking of the web.

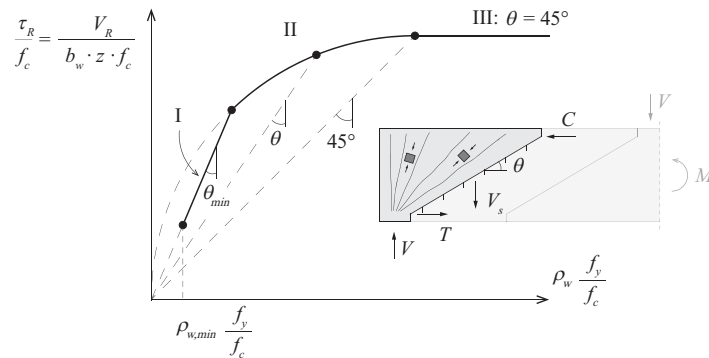


Figure 2.1: Shear resistance as a function of the amount of shear reinforcement according to the Variable Angle Truss models (VAT).

Other than the VAT, alternative design approaches for shear such as the Modified Truss Analogy (MTA) also known as “truss approach with concrete contribution” (ASCE-ACI Committee 445 1998 [ASC98]) are implemented in some codes of practice [ACI19, AAS20]. The MTA accounts in its design formulation for the contribution of concrete (in compression and potentially in tension), as well as for a contribution of the shear reinforcement. Although MTA and VAT models do not necessarily lead to the same results, they are grounded on similar principles. For this reason, they are combined in some design codes, such as *fib*'s Model Code 2010 (Sigrist et al. 2013 [Sig13]).

With respect to shear design based on VAT models and rigid-plastic stress fields, simple and efficient design expressions have been provisioned into codes of practice (as in Eurocode 2 EN 1992-1-1:2004 [Eur04] or the level of approximation II according to *fib*'s MC 2010 [FIB13]). This approach provides accurate estimates of the resistance for slender beams without significant concentrated loads near to the support. Its design expressions are also easy to understand and to use for practical purposes. Such an approach is however not directly applicable to squat members with gravity loads acting on the upper chord, as a direct strut can develop between the load and support without the need of carrying the complete shear force by the shear reinforcement (Fig. 2.2b). In addition, the crack openings developed in the web are more limited for the same level of shear force than for slender members, enhancing the effective concrete strength and eventually the resistance of the member. In order to account for the beneficial effect of the direct strut action, empirical corrections have been proposed as a pragmatic approach in the past. For instance, in EN 1992-1-1:2004, the contribution of loads closer than $a_v \leq 2d$ to the support is reduced by an empirical coefficient β (Fig. 2.2b). In case of a single concentrated load near to the support (acting shear force equal to the load), the design equation reads:

$$\beta \cdot V_{Ed} \leq V_{Rd} = \max(V_{Rd,c}; n \cdot A_{sw} \cdot f_{ywd}) \quad (2.1)$$

where n is the number of activated shear reinforcement units located within three-quarters of the clear shear span a_v [Asi00], f_{yw} is the yield strength of the shear reinforcement, A_{sw} is the cross section area of a shear reinforcement unit, and $V_{Rd,c}$ is the design shear resistance of a member without shear reinforcement. The coefficient β depends on the ratio between the clear shear span a_v and the effective depth of the cross-section d and is calculated as:

$$\beta = \frac{a_v}{2d} \geq 0.25 \quad (2.2)$$

The same expression, but with a value $\beta \geq 0.5$, is assumed by *fib*'s Model Code 2010 [FIB13].

As it can be noted, the approach based on the use of coefficient β is theoretically inconsistent, as it has been derived for members without shear reinforcement and corrects a model developed for slender beams with shear reinforcement (that cannot physically develop when direct strut governs). The performance of the empirical approach of EN 1992-1-1:2004 is compared in Fig. 2.2c with the results of a database on shear-critical beams with shear reinforcement (refer to Table 2.3 in Appendix 2.C, comprising 463 tests and completing a previous database of 263 tests previously collected by Liu [Liu19]). The results of this comparison, see Fig. 2.2c, show a relatively poor performance and is associated with a high scatter.

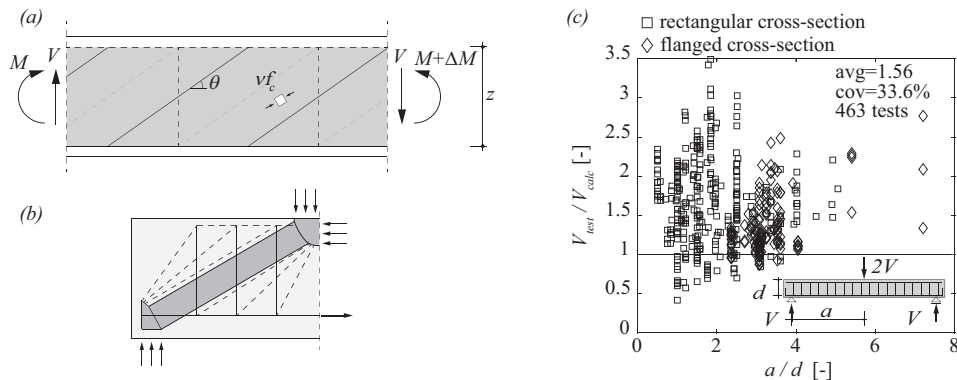


Figure 2.2: Design of slender and squat members: (a) VAT approach; (b) direct strut action and (c) comparison of EN 1992-1-1:2004 accounting for arching action with tests as a function of the shear slenderness a/d .

In an effort to provide more consistent design approaches for squat members, tailored methods have been developed in the past based on rigid-plastic stress fields (lower-bound of the resistance, see Müller [Mül78], Fig. 2.3a) and failure mechanisms (upper-bound of the resistance, Nielsen et al. [Nie11], Fig. 2.3b). Such solutions constitute sound approaches. However, as the state of strains can be significantly different from that of slender members, questions can be raised on the value of the effective strength to be considered in the compression field (strength reduction factor ν according to EN 1992-1-1:2004).

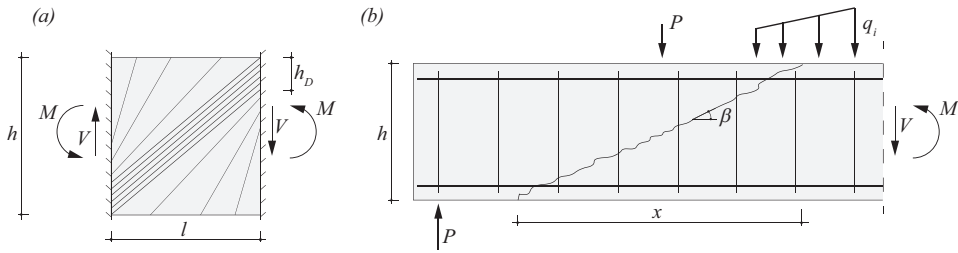


Figure 2.3: Rigid-plastic approaches (a) lower bound approach [Mül78] and (b) upper bound approach [Nie11].

Also, specific strut-and-tie models have been proposed in the past (as Russo’s model [Rus05], Fig. 2.4a) or more refined models, as the Two-Parameter Kinematic Theory (2PKT) by Mihaylov et al. [Mih10, Mih13] (Fig. 2.4b). These approaches are efficient to calculate the response of squat members, but can be difficult to generalize and particularly to provide a smooth transition to slender members.

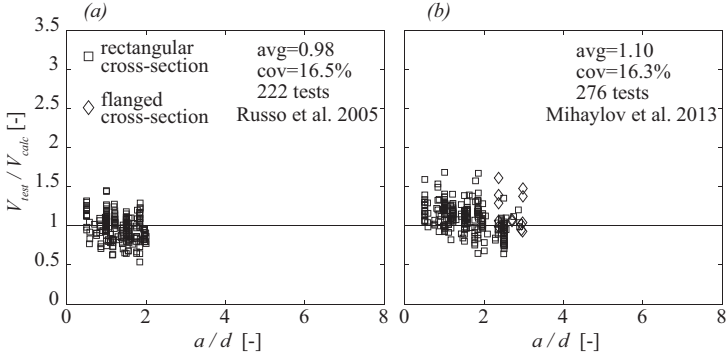


Figure 2.4: Comparison of tailored approaches for squat members: (a) Russo’s model applicable for tests for $a/d \leq 2$ and (b) Two-Parameter Kinematic Theory (2PKT) by Mihaylov et al. for $a/d \leq 3$.

In this chapter, the shear design of squat and slender members is investigated using the stress field method through various Levels-of-Approximation (LoA). The structural response and the transition between squat and slender members are first analysed using the most refined approach (the Elastic-Plastic Stress Fields, EPSF) [Fer07] in order to clarify the governing load-carrying actions. EPSF allow fulfilling equilibrium and yield conditions as well as compatibility of deformations, resulting into an admissible stress field compatible with a failure mechanism as for an exact solution according to limit analysis. On that basis, in this chapter, simplified Rigid-Plastic Stress Fields are proposed for design considering direct struts and fans (or other stress fields to ensure load spreading). In addition, a consistent method is presented to suitably evaluate the associated strength reduction factors accounting for compatibility of deformations. The resulting expressions appear to be simple to be used in practice, and ground the current draft for the revision of *fib* MC2020 and EN 1992-1-1 (prEN 1992-1-1:2022).

2.2 Suitable stress fields for slender and squat members

2.2.1 Influence of slenderness on the mechanical response of concrete members

Shear design has typically been performed distinguishing between slender and squat members following geometrical rules based on the shear slenderness of the member (defined by the shear span-to-effective depth ratio $a/d = M/(V \cdot d)$). According to the works of Kani for members without shear reinforcement [Kan64], a squat member response is assumed for slenderness ratios below $a/d \approx 2.5$ (with the possibility to consider a direct strut action between the load and the support).

For members with shear reinforcement, a more general approach to consider direct support conditions shall however be discussed with reference to the mechanical response of the element. To that aim, the Elastic-Plastic Stress Fields (EPSF) will be used in the following. This approach provides consistent estimates of the resistance both for discontinuity regions (where direct support conditions apply) and slender elements (where plane section deformation holds valid) [Fer07, Mut16, Nik17]. Fig. 2.5 shows for instance a comparison of the resistance calculated with the EPSF approach against a reduced database containing 119 beams with both slender and squat members (a subset of the extended database previously modelled with EPSF by Niketic et al. [Nik17], see Table 2.3). The EPSF approach provides very accurate results (Fig. 2.5) with a mean value (avg) of the measured-to-calculated resistance equal to 1.04 and a Coefficient of Variation (cov) equal to solely 10.6%.

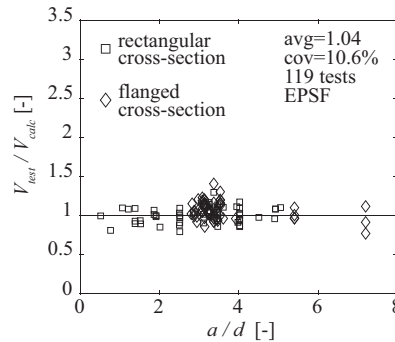


Figure 2.5: Performance of EPSF to model squat and slender beams.

Fig. 2.6 provides more detailed insights of the response observed with EPSF, by comparing three tests with varying slenderness performed by Birrcher et al. [Bir09, Tuc16] and three numerical simulations completing the series. All beams had a rectangular cross section (height $h = 1.905$ m and width $b_w = 0.533$ m) as well as a constant amount of vertical shear reinforcement ($\rho_w = 0.21$ %) and horizontal web reinforcement ($\rho_h = 0.21$ %, except beam 1.85-02 that presented $\rho_h = 0.19$ %). All specimens had comparable uniaxial compressive concrete strength

($f_{cm} = 34 \text{ MPa}$) and flexural reinforcement ratio ($\rho_l = 2.37 \%$). The specimens were modelled using EPSF [Fer07] according to the guidelines of Muttoni et al. [Mut16] as well as by means of rigid-plastic stress fields (RPSF) adapted from Müller [Mül78] and considering a constant value of the strength reduction factor $\nu = 0.5$ to account for the detrimental effect of concrete cracking in the web. As it can be noted, the accuracy of the models is fairly good in both cases, with RPSF being slightly more conservative than the EPSF.

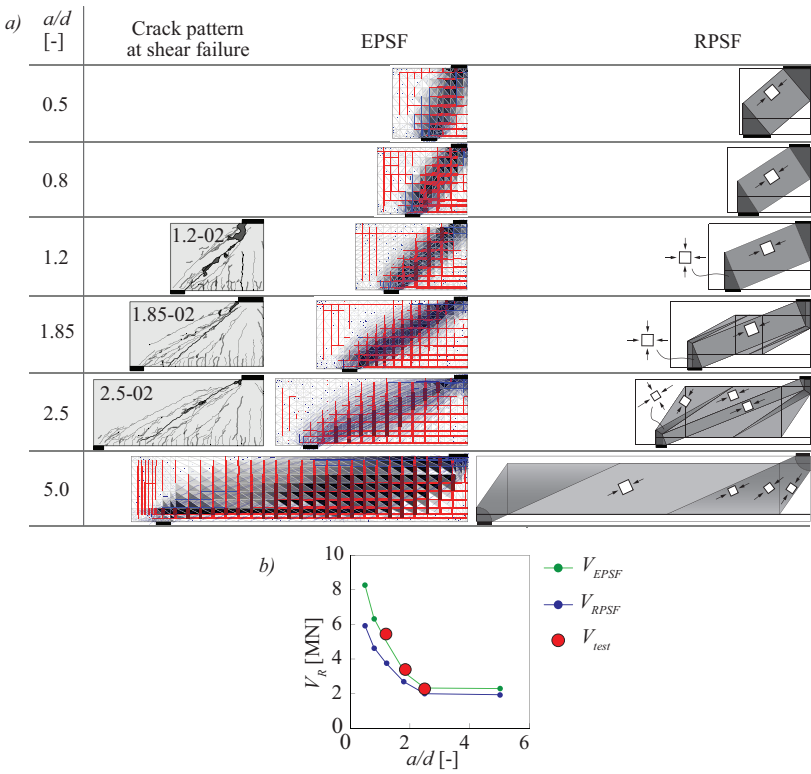


Figure 2.6: Comparison of the three tested beams with EPSF and RPSF. Blue lines of EPSFs represent directions and relative intensity of principal compressive stresses; light and dark red lines represent elastic tension and yield stresses in the reinforcement, respectively (the thickness of red lines being proportional to the steel stress).

The analysis by EPSF clearly shows the transition from the direct strut action (for low shear slenderness) towards a compression field with constant stress over the member’s depth (for higher slenderness). It is also worth noting that when the concentrated load acts closer to the support, the horizontal web reinforcement can be easily activated in the critical region, and both the horizontal and vertical web reinforcements control the spreading of the inclined direct strut carrying shear. Conversely, for slender members, the vertical shear reinforcement usually yields and the horizontal reinforcement plays a minor role. In addition, in this case, the direct strut contribution vanishes for a shear slenderness of approximately $a/d > 2.5$.

With respect to the analysis of the strains, the distribution of the first principal tensile strain ε_1 and the vertical strain ε_y along the beam axis is shown in Fig. 2.7a. Concerning the shear reinforcement, the EPSF analysis shows that it is fully yielded at failure in the critical zone of slender beams. For shear slenderness lower than 0.8, it remains on the contrary in the elastic regime (Fig. 2.7a). The results also indicate that both strains experience peak values approximately in the middle of the shear span for squat members ($a/d \leq 2.5$), while the point of maximum strains shifts towards approximately three-quarters of the shear span for the slenderest member ($a/d = 5$). Such strain distributions govern the strength reduction factor (v , Fig. 2.7c, where v is determined according to Vecchio et al. [Vec86] on the basis of the calculated local principal tensile strain ε_1) and the location of the critical crushing regions.

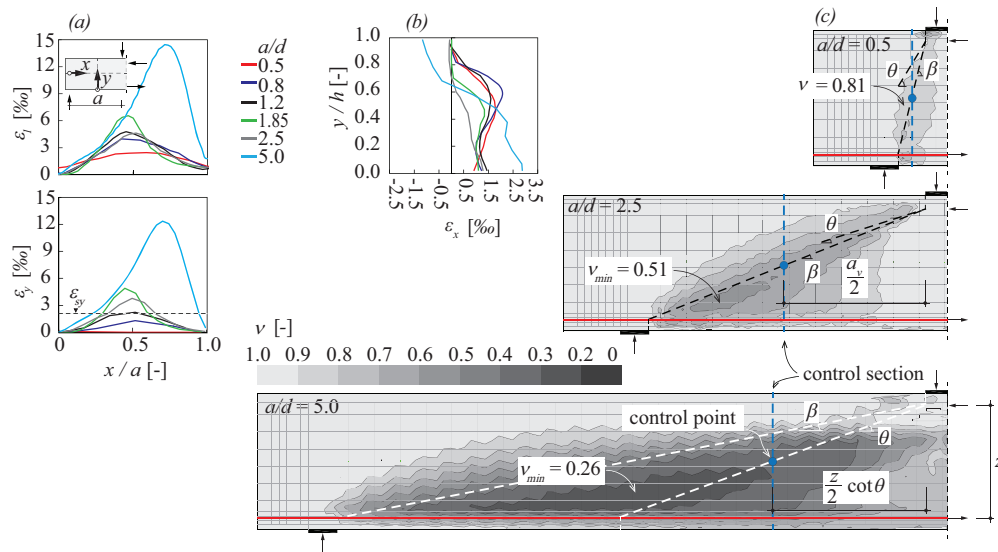


Figure 2.7: Results of simulations based on EPSF: (a) first principal tensile strain ε_1 and vertical strain ε_y distributions along the longitudinal beam axis; (b) longitudinal strain profiles ε_x over the defined control sections and (c) concrete strength reduction factor v for three beams with varying shear slenderness.

Finally, the longitudinal strain profile ε_x is evaluated at a control section located in the middle of the clear shear span a_v for members with direct strutting and at the distance $z/2 \cdot \cot\theta$ from the edge of the loading plate for members without direct strutting (where θ is the inclination of the compression field, refer to Fig. 2.7c). The results are compared for the different cases in Fig. 2.7b. It is worth nothing that, particularly for squat members, the profile of the longitudinal strain ε_x deviates significantly from the linear distribution and thus that the Bernoulli-Navier hypothesis (plane sections remain plane) is not applicable, in agreement with the expected behaviour of discontinuity regions (Fig. 2.7b). Such strain level is in fact comparable to the one in the tension chord.

2.3 Stress fields accounting for direct strutting conditions

In the following, a number of stress fields will be developed aiming at representing the transfer of forces in the support region under direct strut conditions. Their level of refinement will be progressively increased, following a Levels-of-Approximation (LoA) approach [FIB13, Mut12]. First, simple stress fields according to Müller [Mül78] combining fans and concentrated struts will be presented. Such stress fields are developed on the basis of simple and safe assumptions for the strain state and the associated efficiency factors ν for the concrete strength. These fields will correspond thus to a LoA I and will be refined (LoA II) in a second step by considering consistent estimates of the strain state (accounting for compatibility of deformations at the critical regions), in an effort to improve the accuracy of the predicted efficiency factors ν . A more general stress field will later be introduced (LoA III) considering the spreading of the concentrated forces and enabling the activation of the horizontal reinforcement in the web. These models are eventually completed with the EPSF analyses presented in Section 2.2, which constitute the highest degree of refinement (LoA IV, ensuring the compatibility of deformations in the whole element).

2.3.1 Stress Fields with concentrated strut (CSSF) (LoA I, II)

The simplest stress fields for a consistent design of support regions with direct strut conditions are developed assuming rigid-plastic constitutive laws, in a similar manner as Müller [Mül78] for panels. Such stress field consists of a direct (concentrated) inclined strut and two fan regions which activate the shear reinforcement (Fig. 2.9a). The fan regions can consist of struts with varying inclination (as the upper fan region in Fig. 2.9a) or uniaxially and a biaxially compressed wedges (as the lower fan region in Fig. 2.9a) which represent an almost equivalent solution. As it can be noted in Fig. 2.8, when no direct strut develops, the stress field is identical to the one assumed for the design of slender members (Fig. 2.9c), ensuring a smooth transition between cases with and without direct strutting.

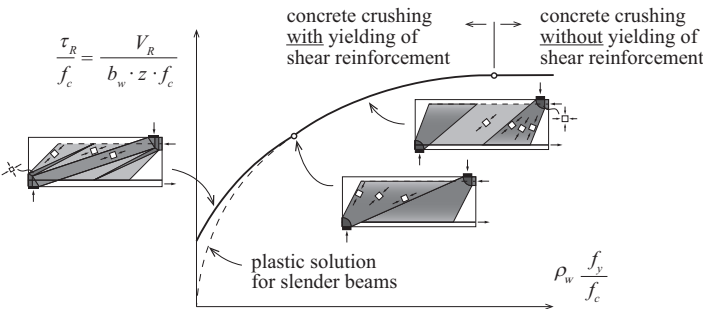


Figure 2.8: Governing stress fields and associated resistance compared to the plastic solution for slender beams.

Based on a free-body analysis of the stress field with direct strutting (Fig. 2.9b), the shear resistance of squat beams can be calculated as the sum of the contributions of the direct strut V_c and the one of the shear reinforcement V_s according to Eq. 2.3.

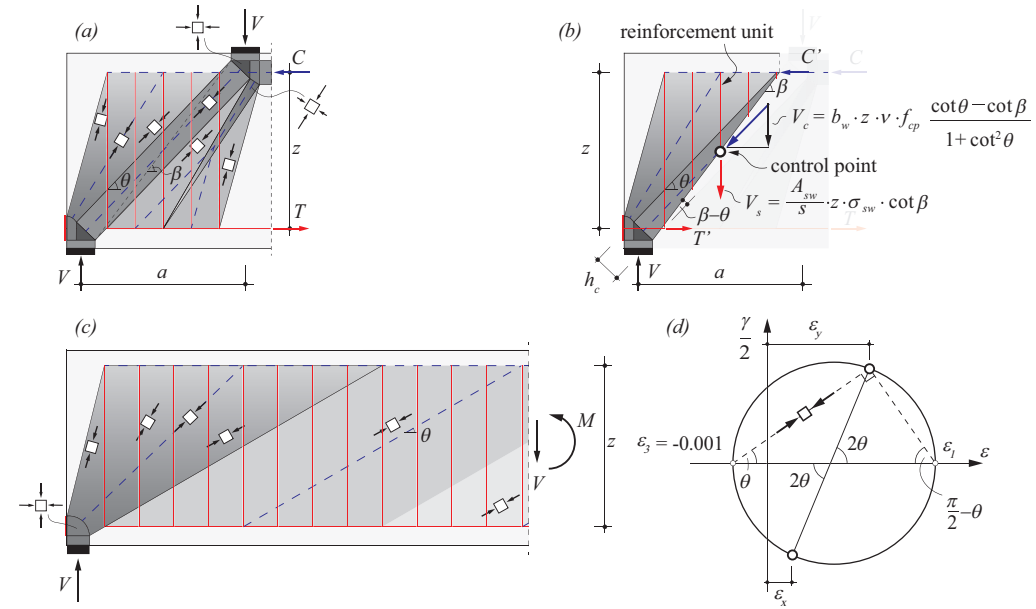


Figure 2.9: RPSF for end regions of beams: (a) stress field with concentrated strut (CSSF); (b) free-body analysis of the CSSF; (c) stress field for slender members, and (d) Mohr's circle of strains at the control point.

$$V_R = V_c + V_s \quad (2.3)$$

It can be noted that the direct strut is inclined at an angle θ , whereas the inclination of the free-body corresponds to an angle β defined by the clear shear span (implicitly accounting for the size of the bearing plates) and the lever arm ($\cot\beta = a_v / z$).

The value of the angle θ is estimated assuming simultaneous yielding of the shear reinforcement and crushing of the compression field for a slender member [Nie11] (Fig. 2.8). The shear force carried by the shear reinforcement intersected by the free-body defined at an angle θ results:

$$V_s = \rho_w \cdot b_w \cdot f_{yw} \cdot z \cdot \cot\theta \quad (2.4)$$

while the shear force carried by concrete for a slender member is calculated as

$$V_c = v \cdot f_{cp} \cdot b_w \cdot z \cdot \cos\theta \cdot \sin\theta \quad (2.5)$$

Assuming both resistances to be equal (failure at simultaneous concrete crushing and reinforcement yielding, $V_s = V_c$) and solving the equation as a function of the angle θ , it results:

$$\cot \theta = \sqrt{\frac{v}{\omega_w} - 1} \quad (2.6)$$

where v refers to the strength reduction factor accounting for the cracking state of concrete (which will be evaluated later according to different levels of refinement) and ω_w is the mechanical shear reinforcement ratio ($\omega_w = \rho_w \cdot f_{yw} / f_{cp}$) where $f_{cp} = \eta_{fc} \cdot f_c$ is the equivalent uniaxial plastic concrete strength, where the concrete brittleness factor η_{fc} is evaluated according to MC2010 (see also Moccia et al. [Moc20]):

$$\eta_{fc} = \left(\frac{30}{f_c} \right)^{\frac{1}{3}} \leq 1.0 \quad (2.7)$$

with f_c in MPa.

If the ratio $\cot \beta / \cot \theta$ is larger than 1, the response of a slender member can be considered corresponding to that of a slender member without direct strutting (Fig. 2.8). On the contrary, if $\cot \beta / \cot \theta < 1$, direct strut action occurs and the width of the concentrated strut h_c can be determined geometrically as:

$$h_c = \frac{z}{\sin \beta} \sin(\beta - \theta) \quad (2.8)$$

Thus, the contribution of this strut to the total resistance results:

$$V_c = b_w \cdot h_c \cdot v \cdot f_{cp} \cdot \sin \theta \quad (2.9)$$

where b_w refers to the effective width of the web, z to the lever arm and f_{cp} to the equivalent uniaxial plastic concrete strength. On that basis, it results a shear resistance:

$$V_R = b_w \cdot z \cdot v \cdot f_{cp} \frac{\cot \theta - \cot \beta}{1 + \cot^2 \theta} + \rho_w \cdot b_w \cdot z \cdot \sigma_{sw} \cdot \cot \beta \quad (2.10)$$

where σ_{sw} is the stress in the shear reinforcement crossing the direct strut. If the resistance is written in terms of shear stress resistance $\tau_R = V_R / (b_w \cdot z)$, previous equation can be rewritten as follows:

$$\tau_R = v \cdot f_{cp} \frac{\cot \theta - \cot \beta}{1 + \cot^2 \theta} + \rho_w \cdot \sigma_{sw} \cdot \cot \beta \quad (2.11)$$

With respect to the term σ_{sw} , it can be calculated accounting for the compatibility of deformations in the clear shear span region (by using Mohr's circle for instance, Fig. 2.9d):

$$\sigma_{sw} = E_s \varepsilon_y = E_s \left[\cot^2 \theta (\varepsilon_x - \varepsilon_3) + \varepsilon_3 \right] \leq f_{yw} \quad (2.12)$$

where E_s is the modulus of elasticity of the shear reinforcement, ε_3 is the principal compressive strain in the direct strut which is assumed to be $\varepsilon_3 = -1$ ‰ and ε_x is the longitudinal strain which

can be calculated as the average between the strain in the bottom longitudinal chord and the strain in the upper chord at the vertical cross-section defined by the control point shown in Fig. 2.9b (this is based on the assumption that plane sections remain plane, which has been observed to deviate from EPSF results particularly for squat members (Fig. 2.7b), but has a limited influence on the global resistance of the member).

Also, for practical purposes, the term σ_{sw} can be assumed to be equal to the yield strength of the reinforcement ($\sigma_{sw} = f_{yw}$) when $\cot\theta > 1$, which is in agreement with experimental evidences and also with elastic-plastic analysis of this region (Fig. 2.7).

As for slender members, the shear resistance with the proposed approach is in any case limited by the crushing resistance of the concrete in the web (horizontal plateau in Fig. 2.8). For the case of vertical stirrups, the maximum resistance can be calculated investigating a free-body limited by a vertical section at mid-distance of the clear shear span, where both the direct strut and concrete in the fans reach their crushing capacities. For the calculation of the crushing resistance (upper limit of Eq. 2.13), it can be assumed that the different regions have the same inclination θ of the concrete fields (assuming the fans to be composed by three wedges each (Fig. 2.9a), where the ones next to the direct strut have the same constant angle as the direct strut [Nie11]):

$$\tau_R = v \cdot f_{cp} \frac{\cot\theta - \cot\beta}{1 + \cot^2\theta} + \rho_w \cdot f_{yw} \cdot \cot\beta \leq v \cdot f_{cp} \frac{\cot\theta}{1 + \cot^2\theta} \quad (2.13)$$

As the previous equation is based on a stress field (lower-bound of the resistance according to limit analysis), the best solution can be found by maximizing the load-carrying capacity as a function of the parameter θ . This can be performed considering, in a simplified manner for the LoA I, a constant value of the efficiency factor v or by calculating v on the basis of the strain state of the member at LoA II.

In the former case (constant value of v , LoA I), a value $v = 0.5$ can be adopted (consistently with prEN 1992-1-1:2022 [Eur21]) resulting into:

$$\cot\theta = \cot\beta + \sqrt{\cot^2\beta + 1} \leq \cot\theta_{min} \quad (2.14)$$

where the right-hand side of the inequality corresponds to the condition for maximum shear resistance outside of this region (with a minimum inclination equal to $\cot\theta_{min} = 2.5$ for members without axial force applied [Eur21, Eur04]). Other values $1 \leq \cot\theta \leq \cot\theta_{min}$ can also be selected for design purposes and will constitute lower-bounds of the resistance.

For the case of variable v (LoA II), the value of θ can be determined numerically, by evaluating v at a control point located in the middle of the clear shear span and at mid-height of the cross-section, in a similar manner as Vecchio and Collins [Vec86]:

$$v = \frac{1}{k_1 + k_2 \left[\varepsilon_x + (\varepsilon_x - \varepsilon_3) \cot^2\theta \right]} \leq 1.0 \quad (2.15)$$

where, after calibration of the three parameters (k_1 , k_2 and ε_3), the best results are obtained for $k_1 = 1.0$, $k_2 = 110$ and $\varepsilon_3 = -0.001$ (see Rupf et al. [Rup13]) which represents a principal compressive strain in the direct strut. Despite the fact that a numerical procedure is required to derive the optimum value of θ with the previous equation, a first estimate can be determined in a simple manner considering:

$$\cot \theta \approx 1.3 \frac{a}{z} \quad (2.16)$$

The mechanical basis of the CSSF allows for a good accuracy (Fig. 2.10) while being still simple to be used. In its simplest formulation (LoA I, constant value of the strength reduction factor ν), it shows more conservative results (Fig. 2.10a), particularly for slender beams, primarily due to the condition limiting $\cot \theta$ to $\cot \theta_{min}$. The refined CSSF approach with variable strength reduction factor ν (LoA II) shows better results (Fig. 2.10b), mostly because it does not have the limitation $\cot \theta \leq \cot \theta_{min}$ which is replaced by more realistic values of ν (low values of ν for smaller compression field inclinations). In any case, both approaches show better predictions than current empirical approaches as that of Eurocode 2 (EN 1992-1-1:2004, Fig. 2.2). It is also interesting to note in Fig. 2.10 that the limit between squat and slender members (red and blue colours, respectively) is not dictated only by the shear slenderness, but also by other factors, such as the shear reinforcement ratio.

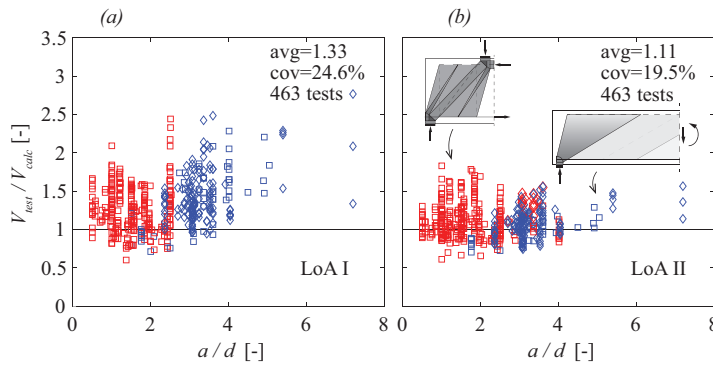


Figure 2.10: Comparison of CSSF model with tests: (a) simplified approach (LoA I) and (b) refined approach (LoA II). Note: red markers refer to tests with direct strutting ($\cot \beta < \cot \theta$); blue markers refer to members without direct strutting ($\cot \beta > \cot \theta$); diamond markers refer to flanged cross-sections while squares represent tests with rectangular cross-sections.

For practical purposes, when multiple concentrated forces are applied [Pas22], all potential critical inclinations β_i should be verified. In addition, in order to account for a uniformly distributed load q acting between the concentrated load and the support, Eq. 2.13 can be adjusted by adding q/b_w to the term $\rho_w \cdot \sigma_{sw}$ in the shear reinforcement contribution Fig. 2.11.

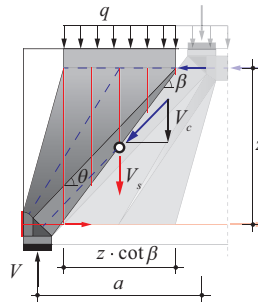


Figure 2.11: Free-body analysis of a member with direct strut action accounting for a uniformly distributed load.

2.3.2 Stress Fields with spreading strut (SSSF) (LoA III)

According to the EPSF results shown in Fig. 2.7, it can be noted that the direct strut does not necessarily have a rectangular shape with constant thickness, but it tends to spread activating both the horizontal and the vertical reinforcement in the web. Such a response can be reproduced with a suitable stress field considering spreading of the strut as shown in Fig. 2.12a. Such a stress field can also be used to reproduce the response of members with higher slenderness (Fig. 2.12b,c), ensuring a transition to slender beams. Three cases can in general be distinguished:

- Members with low slenderness, where full spreading of the direct strut occurs ($\theta_2 > 0$, Fig. 2.12a), with the potential to activate both the vertical shear reinforcement and the horizontal web reinforcement.
- Members with moderate slenderness and larger shear reinforcement (typically $\theta_2 \approx 0$, Fig. 2.12a), where partial spreading of the direct strut can be considered (Fig. 2.12b). In this case, the spreading is primarily ensured by the vertical shear reinforcement equilibrating the struts of the fan.
- For slender members, a smeared compression field can be considered as previously discussed (Fig. 2.12c), where direct strutting completely vanishes.

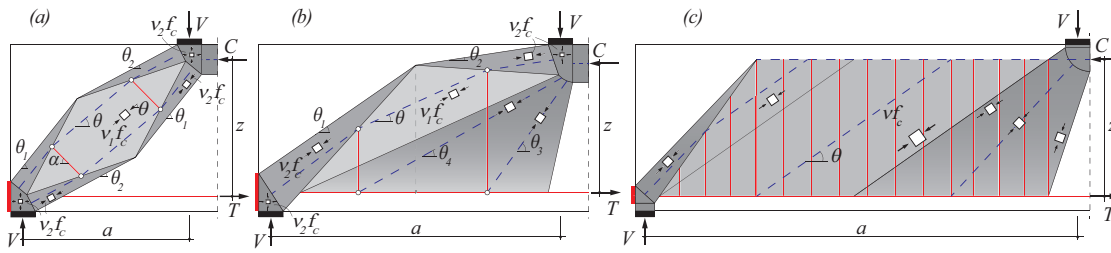


Figure 2.12: Stress fields of SSSF: (a) full spreading; (b) partial spreading and (c) distributed constant compression field.

A detailed description of the transmission of internal forces in the stress field with full strut spreading is sketched in Fig. 2.13a. Its geometry is assumed to be polar symmetric with respect to the point P located in the centre of the shear span. The deviated struts are inclined by angles θ_1 and θ_2 whereas the inner compression field has an inclination θ which can be simply assumed as $\cot\theta = a/z$.

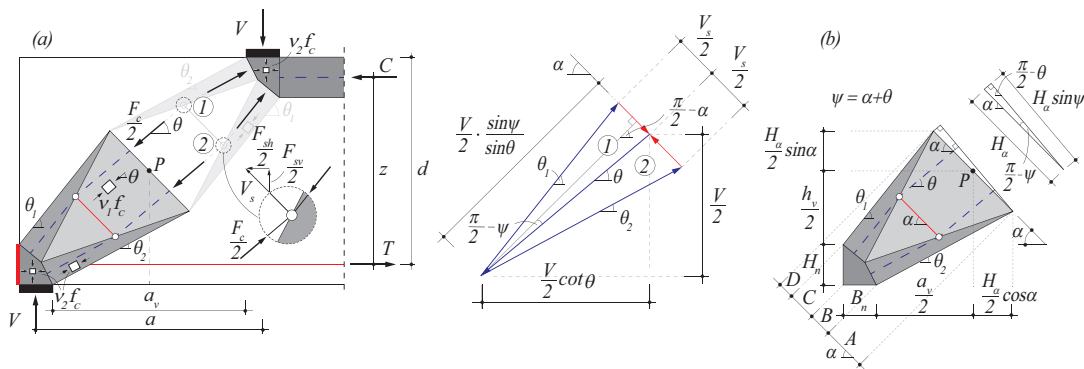


Figure 2.13: SSSF with full spreading: (a) equilibrium in nodes and (b) geometry.

The full development of such case and the associated design expressions are presented in Appendix 2.B.1 of this chapter.

The stress field with partial spreading represents a transition from squat to slender beams. The main definition of this stress field is presented in Fig. 2.14, while details on the solution and design expressions can be found in Appendix 2.B.2. With respect to the stress field for slender members, the governing design expressions remain the same as presented for the previous cases.

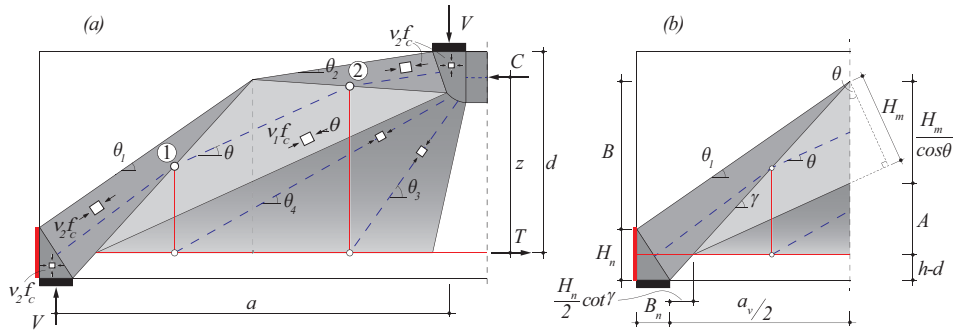


Figure 2.14: SSSF with partial spreading: (a) nodes of strut-and-tie model and (b) geometry.

A comparison of the SSSF approach against the database of beams is shown in Fig. 2.15, showing consistent agreement and enhancing the accuracy of the CSSF. More details are given in the following section.

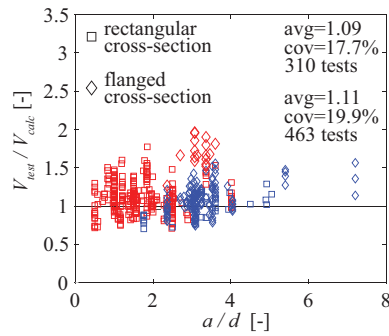


Figure 2.15: Comparison of SSSF (LoA III) with direct strutting (red marks) and beams without direct strutting (blue marks).

2.4 Performance of the considered shear models with respect to the extended and reduced databases

A systematic comparison of the shear models is reported in Table 2.1 and 2.2 through statistical values for the extended database of 463 tests and the reduced database of 119 tests. The reduced database refers to a subset, containing the members analysed by EPSF (tests with sufficiently detailed descriptions of the geometry, the reinforcement and the loading conditions to be analysed using EPSF). The results are given for shear slenderness lower and higher than $a_v/d = 2.25$, which is here adopted as an approximated estimate of the limit between slender and squat response EN1992-1-1:2004 [Eur04].

As it can be noted, the simplified CSSF (LoA I) provides a safe estimate with an accuracy comparable to that of the empirical correction of EN1992-1-1:2004. The accuracy is significantly improved with the refined CSSF (LoA II), and is further enhanced by using the SSSF (LoA III) and the EPSF analyses (LoA IV). It can be noted that the CSSF considers in these analyses the lever arm z as the governing geometrical dimension, but stress fields accounting for the height of the member h can also be developed for rectangular cross sections leading to an improvement of the results.

Table 2.1: Performance of different shear models for beams with rectangular cross-sections (avg - average and cov - coefficient of variation).

Rectangular beams	Reduced database						Extended database					
	all		$a_v/d < 2.25$		$a_v/d \geq 2.25$		all		$a_v/d < 2.25$		$a_v/d \geq 2.25$	
	(54 tests)		(28 tests)		(26 tests)		(310 tests)		(270 tests)		(40 tests)	
shear model	avg	cov	avg	cov	avg	cov	avg	cov	avg	cov	avg	cov
EN1992-1-1:2004	1.54	0.31	1.45	0.39	1.65	0.20	1.66	0.34	1.68	0.35	1.54	0.23
Simplified CSSF (LoA I)	1.34	0.30	1.06	0.21	1.71	0.22	1.29	0.25	1.26	0.24	1.54	0.23
Refined CSSF (LoA II)	1.03	0.17	0.99	0.17	1.06	0.17	1.11	0.20	1.12	0.21	1.01	0.14
SSSF (LoA III)	1.07	0.18	1.01	0.17	1.13	0.16	1.09	0.18	1.10	0.18	1.07	0.18
EPSF (LoA IV)	1.01	0.11	0.98	0.10	1.03	0.10	-	-	-	-	-	-

Table 2.2: Performance of different shear models for flanged beams.

Flanged beams	Reduced database						Extended database					
	all		$a_v/d < 2.25$		$a_v/d \geq 2.25$		all		$a_v/d < 2.25$		$a_v/d \geq 2.25$	
	(65 tests)		(0 tests)		(65 tests)		(153 tests)		(15 tests)		(138 tests)	
shear model	avg	cov	avg	cov	avg	cov	avg	cov	avg	cov	avg	cov
EN1992-1-1:2004	1.59	0.26	-	-	1.59	0.26	1.35	0.27	1.17	0.12	1.37	0.27
Simplified CSSF (LoA I)	1.58	0.25	-	-	1.58	0.25	1.42	0.23	1.29	0.14	1.43	0.24
Refined CSSF (LoA II)	1.22	0.14	-	-	1.22	0.14	1.11	0.18	0.95	0.12	1.11	0.18
SSSF (LoA III)	1.30	0.22	-	-	1.30	0.22	1.15	0.23	0.97	0.14	1.17	0.23
EPSF (LoA IV)												

2.5 Conclusions

This chapter investigates the response of beams with shear reinforcement and varying shear slenderness with the potential to develop direct strutting conditions. Its main conclusions are:

1. The empirical corrections of the shear resistance of slender members adopted by several codes of practice (as EN 1992-1-1:2004 or Model Code 2010) for the design of squat members lack a physical basis and present highly scattered predictions.
2. Consistent design methods based on stress fields can be developed for the shear response of squat and slender members leading to simple and physically-sound expressions. They can be safely used for the design of new structures (lower-bound of the resistance) and also, by optimization of the failure load, as accurate models for the assessment of existing structures. Such stress fields can be formulated with increasing level of refinement following a Levels-of-Approximation approach.
3. A method named Stress Fields with a concentrated strut (CSSF) is presented enabling to cover direct strutting conditions for squat members with a smooth transition to the case without direct strutting for slender members. It consists of the combination of a direct inclined strut with two fan regions and can be interpreted as a simplification of the Elastic-Plastic Stress Field (EPSF) method. The CSSF provides accurate and reliable estimates of the shear resistance, while being simple to use. The proposed model allows calculating the efficiency factor ν accounting for concrete cracking, the inclination of the compression field θ and the tensile strains in the shear reinforcement accounting for compatibility of deformations at a control point (located at centre of the clear shear span).
4. Two levels of refinement can be considered in the CSSF. The first (LoA I) is intended for simple design of new structures, assuming a constant value of the efficiency factor of concrete ($\nu = 0.5$) and limiting the angle of the compression field as performed for slender members. The latter refers to a more refined approach (LoA II) intended for detailed design or for the assessment of existing structures. It allows calculating the value of ν on the basis of the strain state in the web without introducing an additional limit on the angle of the compression field.
5. Both the simplified and the refined CSSF approaches, implemented in the second generation of Eurocode 2 and in MC2020, provide more accurate predictions of the shear resistance than those of EN 1992-1-1:2004. Particularly, the scatter of the test evaluation is significantly reduced when the refined method is applied.

6. An alternative interpretation of EPSF named Stress Fields with the spread strut (SSSF, LoA III) is also presented. It accounts for spreading of the direct strut by considering both the shear reinforcement and the horizontal web reinforcement. As for the CSSF, the efficiency factors are calculated based on the compatibility of deformations, resulting into less scattered results than the CSSF.

Appendix 2.A: Refined approach of CSSF (LoA II)

The refined approach of the CSSF (LoA II) considers that the efficiency factor ν can be calculated on the basis of a refined estimate of chord forces in the middle of the shear span (see Fig. 2.16). These forces can be calculated as follows:

$$l_{c,act} = a_v - H_n \cot \theta = a_v - z \frac{\cot \theta - \cot \beta}{1 + \cot^2 \theta} \cot^2 \theta \quad (2.17)$$

$$C_2 = \rho_w \cdot b_w \cdot f_{sy} \frac{l_{s,act}}{2} \cdot \frac{B_n + \frac{H_n}{2} \cot \theta + \frac{l_{s,act}}{4}}{z - \frac{H_n}{2}} \quad (2.18)$$

$$T_1 = (V - \rho_w \cdot b_w \cdot f_{sy} \cdot l_{s,act}) \cot \theta \quad (2.19)$$

$$\Delta T_2 = \rho_w \cdot b_w \cdot f_{sy} \frac{l_{s,act}}{2} \cdot \frac{\frac{3}{4} l_{s,act} + \frac{H_n}{2} \cot \theta + z \frac{\cot \theta - \cot \beta}{1 + \cot^2 \theta}}{z \left(1 - \frac{1}{2} \cdot \frac{\cot \theta - \cot \beta}{1 + \cot^2 \theta} \cot \theta \right)} \quad (2.20)$$

$$T_2 = T_1 + \Delta T_2 \quad (2.21)$$

where $l_{s,act}$ refers to the width of the fan region where a part of the force is carried by the shear reinforcement, C_2 and T_2 to the corresponding compression and tension chord forces, respectively. The height and of the node can be approximated as $H_n = B_n \cdot \cot \theta$, where the width is calculated as $B_n = z \frac{\cot \theta - \cot \beta}{1 + \cot^2 \theta}$.

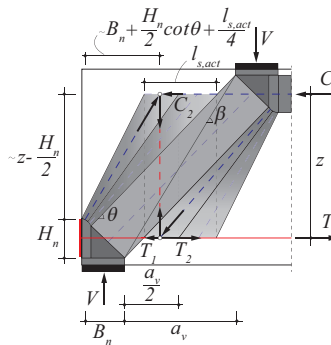


Figure 2.16: Stress field with direct strut for refined calculation of chord forces.

Appendix 2.B.1: SSSF with full spreading (LoA III)

In order to obtain the solution of the stress field with the full spreading, the equilibrium in the nodes is enforced (Fig. 2.13a,b) as follows:

$$V_s = V \frac{\sin \psi}{\sin \theta} (\cot \psi_2 - \cot \psi) \quad \text{in node 1} \quad (2.22)$$

and

$$V_s = V \frac{\sin \psi}{\sin \theta} (\cot \psi - \cot \psi_1) \quad \text{in node 2} \quad (2.23)$$

where $\psi_{1(2)} = \theta_{1(2)} + \alpha$. Here, α represents the inclination of the resultant of the forces in the shear reinforcement F_{sv} and of the horizontal web reinforcement F_{sh} which can be calculated as $\alpha = \text{acot}(F_{sh} / F_{sv})$. Combining these two nodal equilibrium conditions, one obtains a geometrical condition:

$$\cot \psi_1 + \cot \psi_2 = 2 \cot \psi \quad (2.24)$$

In order to evaluate the stresses in the shear reinforcement satisfying the compatibility of deformations in the shear span, one can use the following formula:

$$\sigma_{svv} = E_s \cdot \varepsilon_y = E_s \left[\cot^2 \theta (\varepsilon_x + 0.001) - 0.001 \right] \leq f_{yvv} \quad (2.25)$$

and the stresses in the horizontal web reinforcement can be calculated assuming an elastic-plastic behaviour according to:

$$\sigma_{swh} = E_s \cdot \varepsilon_x \leq f_{ywh} \quad (2.26)$$

where ε_x is the longitudinal strain evaluated at the control point in the middle of the clear shear span (see Fig. 2.9a). Furthermore, a geometrical condition has to be established based on Fig. 2.13b. It refers to the dimensions of the support/load node (B, C) projected at an inclined cut (at angle α) added to the projected distances (A, D) from the node to the edges governed by angles θ_1 and θ_2 :

$$A + B + C + D = H_\alpha \quad (2.27)$$

where

$$H_\alpha = \frac{V}{b_w \cdot v_1 \cdot f_{cp}} \frac{1}{\sin \psi \cdot \sin \theta} \quad (2.28)$$

$$A = \left(\frac{a}{2} - \frac{V}{2 \cdot b_w \cdot v_2 \cdot f_{cp}} + \frac{H_\alpha}{2} \cos \alpha \right) \frac{\cot \psi_2}{\cot \psi_2 \cdot \cos \alpha + \sin \alpha} \quad (2.29)$$

$$B = \frac{V}{b_w \cdot v_2 \cdot f_{cp}} \cos \alpha \quad (2.30)$$

$$C = \frac{V \cot \theta}{b_w \cdot v_2 \cdot f_{cp}} \sin \alpha \quad (2.31)$$

$$D = \left(-\frac{h}{2} + \frac{V \cot \theta}{b_w \cdot v_2 \cdot f_{cp}} - \frac{H_\alpha}{2} \sin \alpha \right) \frac{\cot \psi_1}{\cos \alpha - \cot \psi_1 \cdot \sin \alpha} \quad (2.32)$$

As Eq. 2.27 is non-linear, one can calculate the shear resistance V iteratively. The support and the load nodes as well as the deviated struts (under θ_1 and θ_2) are assumed to be uncracked ($v_2 = 1$) whereas the inner compression field (with inclination θ) is considered to be cracked with an efficiency factor v_1 lower than 1, which can be calculated on the basis of the longitudinal strains and the compression field inclination as follows:

$$v_1 = \frac{1}{1.0 + 110 \cdot \left[\varepsilon_x + (\varepsilon_x + 0.001) \cot^2 \theta \right]} \leq 1.0 \quad (2.33)$$

A limiting condition of the crushing nodes shall also be verified:

$$V_{\max, c_p} = \min(c_{p, \text{inf}}; c_{p, \text{sup}}) \cdot b_w \cdot v_2 \cdot f_{cp} \quad (2.34)$$

where $c_{p, \text{sup}}$ and $c_{p, \text{inf}}$ are the widths of the loading and support plates, respectively. The maximum possible shear resistance can be calculated referring to concrete crushing of a compression field of a free body cut at mid-way between the load and the support:

$$V_{\max, h} = h \cdot b_w \cdot v_1 \cdot f_{cp} \frac{\sin \psi \cdot \sin \theta}{\sin \alpha} \quad (2.35)$$

Appendix 2.B.2: SSSF with partial spreading (LoA III)

The solution of the stress field with partly spread strut can be derived on the basis of the nodal equilibrium of forces (Fig. 2.14):

$$V_s = 2V \left(1 - \frac{\tan \theta}{\tan \theta_1} \right) \quad \text{in node 1} \quad (2.36)$$

and

$$V_s = 2V \left(1 - \frac{\tan \theta_2}{\tan \theta_1} \right) \quad \text{in node 2} \quad (2.37)$$

Combining the two conditions, it results:

$$\tan \theta_1 + \tan \theta_2 = 2 \tan \theta \quad (2.38)$$

In addition, a geometrical condition based on the Fig. 2.14b has to be satisfied:

$$\frac{H_n}{2} + B = A + \frac{H_m}{\cos \theta} \quad (2.39)$$

where:

$$B = \left(\frac{a_v}{2} + \frac{a_v}{b_w \cdot v_2 \cdot f_{cp}} \right) \tan \theta_1 \quad (2.40)$$

$$A = [a_v/2 - (h-d) \cot \gamma] \tan \theta \quad (2.41)$$

$$H_m = \frac{V \cdot \cot \theta_1}{b_w \cdot v_1 \cdot f_{cp} \cdot \cos^2 \theta} \quad (2.42)$$

The inclination γ of the deviated strut can be calculated as follows:

$$\cot \gamma = \frac{a_v}{2} \cdot \frac{1}{H_n + (B_n + a_v/2) \tan \theta_1} \quad (2.43)$$

and the two diagonal struts in the fan region are defined by the inclinations θ_3 and θ_4 as follows:

$$\cot \theta_3 = \frac{\frac{a_v}{4} + \frac{V}{b_w \cdot v_2 \cdot f_{cp}}}{h - \frac{H_n}{2} - V \cdot \cot \theta_1} \quad (2.44)$$

$$\cot \theta_4 = \frac{a_v + B_n - \frac{H_n}{2} \cot \gamma - \frac{1}{2} \left(\frac{a_v}{2} - \frac{H_n}{2} \cot \gamma \right)}{h - \frac{H_n}{2} - V \cdot \cot \theta_1} \quad (2.45)$$

The considerations on the calculation of the strength reduction factor (already presented for the full spreading case), hold valid for the stress field with partial spreading, by accepting the Bernoulli-Navier hypothesis. Therefore, ε_x is approximately equal to $\varepsilon_T/2$ which can be calculated at a cross section in the middle of the shear span on the basis of, for instance, the stress field sketched in Fig. 2.17.

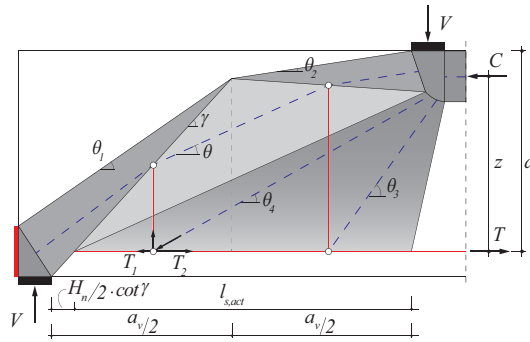


Figure 2.17: Tension chord forces.

The shear reinforcement is considered active solely along its active length $l_{s,act}$:

$$l_{s,act} = a_v - H_n/2 \cot \theta \quad (2.46)$$

Furthermore, the tension force can be evaluated as:

$$T_1 = V \cdot \cot \theta_1 \quad (2.47)$$

$$\Delta T_2 = \rho_w \cdot b_w \cdot f_{wy} \cdot l_{s,act} / 2 \cdot \cot \theta_4 \quad (2.48)$$

$$T_2 = T_1 + \Delta T_2 \quad (2.49)$$

Once V_s has been calculated and the fan geometry has been defined in terms of $\cot \theta_3$ and $\cot \theta_4$ (Fig. 2.14a), a shear resistance condition has to be verified:

$$V_{fan} = \frac{\frac{V_s}{2} (\cot \theta_3 + \cot \theta_4)}{\cot \theta - \cot \theta_1} \quad (2.50)$$

In addition, another resistance condition has to be verified referring to concrete crushing (assuming the same inclination of the compression field all over the cross section):

$$V_c = v_1 \cdot f_{cp} \cdot b_w (H_m + A) \frac{\cot \theta}{1 + \cot^2 \theta} \quad (2.51)$$

The SSSF approach (LoA III) is developed for beams with rectangular cross section, and the presence of flanges will potentially increase the load-carrying capacity.

Appendix 2.C

The number of members stored in the extended and the reduced databases are reported in Table 2.3.

Table 2.3: The extended and the reduced databases.

Year	Author(s)	No of tests in the extended (reduced) database	Year	Author(s)	No of tests in the extended (reduced) database
1951	Clark [Cla51]	46 (-)	2005	Salamy et al. [Sal05]	8 (-)
1954	Moody et al. [Moo54]	2 (-)	2007	Zhang et al. [Zha07]	4 (-)
1963	Leonhardt et al. [Leo63]	11 (11)	2007	Sherwood et al. [She07]	2 (-)
1963	Bresler et al. [Bre63]	5 (5)	2008	Garay et al. [Gar08]	2 (-)
1966	Krefeld et al. [Kre66]	9 (9)	2008	Fernández et al. [Fer08]	4 (4)
1971	Placas et al. [Pla71]	45 (23)	2009	Zhang et al. [Zha09]	14 (-)
1974	Sørensen [Sør74]	10 (8)	2009	Birrcher et al. [Bir09]	27 (6)
1980	Bach et al. [Bac80]	57 (10)	2010	Sahoo et al. [Sah10]	7 (1)
1982	Lee [Lee82]	4 (-)	2010	Senturk et al. [Sen10]	4 (3)
1982	Smith et al. [Smi82]	47 (-)	2010	Zhang et al. [Zha10]	1 (-)
1986	Rogowsky et al. [Rog86]	10 (1)	2010	Mihaylov et al. [Mih10]	8 (-)
1988	Levi et al. [Lev89]	7 (-)	2010	Sagaseta et al. [Sag10]	1 (1)
1996	Kaufmann et al. [Kau96]	4 (4)	2011	Sagaseta et al. [Sag11]	7 (7)
1998	Foster et al. [Fos98]	1 (-)	2013	Rupf et al. [Rup13]	13 (13)
1998	Kong et al. [Kon98]	31 (2)	2013	Walraven et al. [Wal13]	18 (-)
1999	Tan et al. [Tan99]	9 (-)	2015	De Wilde et al. [De15]	2 (2)
2000	Yoshida [Yos00]	1 (-)	2018	Hu et al. [Hu18]	6 (6)
2005	Tanimura et al. [Tan05]	36 (3)			

In the following, the comparison between considered tests and Levels of Approximation I, II and III is presented.

		LoA I	LoA II	LoA III		LoA I	LoA II	LoA III
	test	V_{test}/V_{calc}			test	V_{test}/V_{calc}		
[Cla51]	A1-1	0.98	0.92	1.01	[Lee82]	SD-1	1.03	1.09
	A1-2	0.92	0.87	0.96		SD-2	1.23	1.18
	A1-3	0.98	0.93	1.03		SD-3	1.17	1.07
	A1-4	1.07	1.01	1.10		SD-4	1.25	1.12
	B1-1	1.19	1.22	1.14	[Smi82]	1A1-10	1.74	1.46
	B1-2	1.07	1.07	1.00		1A2-11	1.64	1.38
	B1-3	1.22	1.24	1.15		1A3-12	1.69	1.42
	B1-4	1.15	1.17	1.09		1A4-51	1.73	1.46
	B1-5	1.02	1.03	0.96		1A6-37	1.82	1.54
	B2-1	1.06	0.84	0.99		2A1-38	1.43	1.14
	B2-2	1.00	0.86	1.00		2A3-39	1.53	1.18
	B2-3	1.10	0.91	1.07		2A4-40	1.50	1.17
	B6-1	1.35	1.34	1.16		2A6-41	1.51	1.14
	C1-1	1.13	1.18	1.01		3A1-42	1.55	0.86
	C1-2	1.25	1.31	1.12		3A3-43	1.60	0.90
	C1-3	1.03	1.08	0.93		3A4-45	1.53	0.90
	C1-4	1.09	1.15	0.97		3A6-46	1.50	0.86
	C2-1	1.00	0.88	0.90		1B1-01	1.55	1.44
	C2-2	0.98	0.90	0.91		1B3-29	1.60	1.48
	C2-4	0.87	0.85	0.84		1B4-30	1.53	1.42
	C3-1	1.29	1.20	1.13		1B6-31	1.75	1.61
	C3-2	1.18	1.08	1.02		2B1-05	1.34	1.12
	C3-3	1.10	1.01	0.96		2B3-0.6	1.38	1.15
	C4-1	1.29	1.30	1.07		2B4-07	1.44	1.15
	C6-2	1.29	1.36	1.08		2B4-52	1.37	1.23
	C6-3	1.33	1.40	1.11		2B6-32	1.46	1.24
	C6-4	1.28	1.35	1.07		3B1-08	1.61	1.03
	D1-1	0.99	0.98	0.86		3B1-36	1.55	1.03
	D1-3	0.88	0.87	0.76		3B3-33	1.66	1.05
	D2-1	0.97	0.89	0.81		3B4-34	1.61	1.02
	D2-2	0.96	0.92	0.84		3B6-35	1.60	1.07
	D3-1	1.12	0.90	0.84		4B1-09	1.79	0.83
	D4-1	1.08	0.70	0.75		1C1-14	1.59	1.61
	D1-6	1.01	1.05	0.98		1C3-02	1.52	1.55
	D1-7	1.03	1.07	1.00		1C4-15	1.58	1.62
	D1-8	1.07	1.11	1.04		1C6-16	1.51	1.54
	E1-2	0.99	0.95	1.07		2C1-17	1.29	1.30
	D2-6	0.78	0.79	1.00		2C3-03	1.12	1.10
	D2-7	0.75	0.75	0.95		2C3-27	1.24	1.22
	D2-8	0.83	0.82	1.06		2C4-18	1.27	1.29
	D4-1	0.96	0.94	1.11		2C6-19	1.24	1.28
	D4-2	0.90	0.89	1.07		3C1-20	1.40	1.07
	D4-3	1.01	0.98	1.21		3C3-21	1.57	1.02
	D5-1	1.09	0.99	1.05		3C4-22	1.45	1.00
	D5-2	1.17	1.05	1.10		3C6-23	1.50	1.07
	D5-3	1.17	1.07	1.14		4C1-24	1.55	0.93
[Moo54]	III-30	1.30	1.27	1.20		4C3-04	1.44	0.94
	III-31	1.54	1.11	1.16		4C3-28	1.64	0.97

Design of slender and squat reinforced concrete members with shear reinforcement

	LoA I	LoA II	LoA III		LoA I	LoA II	LoA III
test	V_{rest}/V_{calc}			test	V_{rest}/V_{calc}		
	1.21	0.99	1.18	3-1400/0.75	1.22	1.04	1.34
	1.56	0.98	1.15	4-1750/0.75	1.21	1.09	1.40
	0.91	0.82	1.08	2-1000/1.00	1.04	0.93	0.83
[Rog86]	0.95	0.94	1.01	4-1750/1.00	1.09	1.10	0.89
	2.09	1.83	1.36	3-1400/1.00	1.24	1.20	0.99
	1.51	1.36	1.33	[Yos00] YB2000/4	1.61	0.93	0.91
	1.38	1.26	1.32	[Tan05] 2	1.64	1.23	1.18
	1.04	0.98	1.04	3	1.57	1.19	1.20
	1.84	1.66	1.30	4	1.53	1.18	1.25
	1.33	1.25	1.21	6	1.67	1.46	1.38
	1.26	1.20	1.20	7	1.40	1.27	1.17
	1.11	1.09	1.14	8	1.32	1.16	1.11
[Fos98]	0.95	1.07	1.09	10	1.53	1.56	1.33
[Kon98]	1.36	1.01	0.93	28	1.25	1.02	1.16
	1.24	0.92	0.85	11	1.15	1.09	1.08
	1.23	0.91	0.84	31	0.84	0.88	1.02
	1.66	1.23	1.13	12	1.30	0.94	1.06
	1.51	1.12	1.03	14	1.58	1.40	1.32
	1.34	0.99	0.91	15	1.35	1.24	1.14
	2.09	1.36	1.12	16	1.28	1.17	1.12
	1.63	1.12	0.96	17	1.22	1.08	1.02
	1.49	1.09	0.99	18	1.37	1.25	1.15
	1.29	0.95	0.86	19	1.15	1.04	1.00
	1.32	1.08	1.02	20	1.32	0.88	1.19
	1.64	1.17	1.04	21	1.18	0.61	0.92
	1.39	0.99	0.88	22	0.80	0.67	0.83
	1.80	1.21	1.00	29	1.11	0.93	1.11
	1.38	0.92	0.76	30	1.13	0.95	1.16
	2.44	1.55	1.22	32	0.71	0.66	0.92
	2.33	1.48	1.16	33	1.26	0.94	0.94
	1.32	0.81	0.71	34	1.16	0.88	0.88
	1.32	0.88	0.77	36	0.96	0.94	0.73
	1.49	1.07	0.95	37	0.89	0.91	0.72
	1.45	1.24	1.10	39	0.96	1.10	1.15
	1.74	1.10	1.04	40	0.87	0.89	1.01
	1.41	1.01	0.89	41	0.76	0.72	0.72
	1.57	1.69	1.38	46	1.20	1.19	1.26
	1.57	1.78	1.46	47	1.03	1.05	1.12
	2.17	1.41	1.16	48	1.10	1.28	1.17
	1.75	1.20	1.02	49	0.79	0.92	0.98
	1.82	1.33	1.20	L6	0.82	1.01	1.07
	1.56	1.14	1.03	L7	0.82	1.00	1.06
	1.40	1.11	1.05	[Sal05] B-3	1.22	0.95	0.88
	1.27	1.05	1.01	B-4	1.66	1.30	1.30
[Tan99]	1.37	1.01	0.80	B-7	1.39	1.26	1.07
	1.24	1.10	1.15	B-8	1.25	1.19	1.07
	1.33	1.10	1.02	B-11	1.37	1.45	1.28
	1.23	0.97	1.29	B-12	1.25	1.14	1.16

	LoA I	LoA II	LoA III		LoA I	LoA II	LoA III
test	V_{test}/V_{calc}			test	V_{test}/V_{calc}		
	1.09	1.16	1.09	IV-2123-2.5-02	1.06	1.19	1.21
	0.99	1.03	1.01	M-03-4-CCC2436	1.54	1.63	1.53
[Zha07]	1.01	1.04	0.93	M-03-4-CCC0812	1.44	1.50	1.41
	0.88	0.92	0.83	[Sah10] BML-85-85	1.30	1.09	0.91
	0.95	1.00	0.93	BML-68-83	1.29	1.10	0.91
	0.88	0.93	0.84	BML-57-57	1.31	1.11	0.93
[She07]	1.52	0.86	0.82	BML-57-0	1.19	1.01	0.84
	1.74	0.97	0.88	BML-26-0	1.02	0.89	0.74
[Gar08]	1.72	1.63	1.55	BML-53-100	1.20	1.03	0.85
	1.59	1.76	1.59	BMM-125-125	1.42	1.20	1.01
[Zha09]	0.87	1.00	0.93	[Sen10] D6.A4.G60#5S	0.75	0.90	1.02
	1.06	1.22	1.14	D6.A4.G40#4S	0.79	0.98	0.99
	0.89	1.03	0.96	D6.A2.G40#4S	0.60	0.83	0.89
	0.95	1.14	1.07	D4.A2.G40#4S	0.73	0.86	1.12
	0.95	1.08	1.08	[Zha10] TCDB-2-3	0.80	0.88	0.85
	1.09	0.90	1.06	[Mih10] S1M	0.79	1.01	0.90
	1.07	1.21	1.13	S1C	0.79	1.01	0.91
	1.00	1.13	1.06	L1M	1.03	0.89	0.83
	1.11	1.25	1.17	L1C	1.00	0.86	0.81
	0.78	0.88	0.82	B2	1.48	1.26	1.46
	0.85	0.98	1.00	B8	1.29	1.16	1.36
	1.17	1.04	1.08	C2	1.52	1.29	1.50
	0.84	0.86	1.01	C8	1.17	1.05	1.23
	1.17	0.96	0.73	[Rog86] 1/1.0 N	0.90	0.89	0.94
[Bir09]	1.21	1.34	1.28	[Sag10] AL3	1.12	1.20	1.16
	1.30	1.45	1.41	[Sag11] BG1	0.90	0.82	0.82
	1.33	1.43	1.32	BG2	0.85	0.70	0.70
	1.41	1.53	1.44	BL1	0.97	0.87	0.87
	1.30	1.41	1.36	BL2	0.98	0.89	0.89
	0.96	0.99	0.87	CB1	1.00	0.80	0.80
	1.35	1.55	1.53	CB2	0.93	0.88	0.88
	1.32	1.49	1.45	DB1	0.97	0.78	0.78
	1.34	1.42	1.38	[Hu18] D1.9	1.14	1.26	1.22
	1.58	1.67	1.50	D2.5	0.92	0.87	1.12
	1.42	1.53	1.44	D3.1	0.84	0.76	0.76
	1.39	1.50	1.45	R1.9	1.05	1.15	1.13
	0.91	1.01	0.98	R2.5	1.05	1.00	1.29
	0.87	0.95	0.91	R3.1	0.95	0.85	0.85
	1.25	1.38	1.35	[Kre66] 26-1	1.42	0.85	1.08
	1.56	1.64	1.56	29a-1	1.65	0.89	0.98
	1.69	1.53	1.60	29b-1	1.65	0.89	0.99
	1.14	1.04	1.05	213.5-1	2.28	1.11	1.04
	1.31	1.24	1.48	29a-2	2.05	1.14	1.31
	1.15	1.22	1.07	29b-2	1.78	0.98	1.10
	1.04	1.11	1.03	29c-3	1.50	0.93	1.17
	1.14	0.92	0.91	29d-3	1.61	0.94	1.13
	1.45	1.37	1.26	29e-3	1.87	1.00	1.11
	1.45	1.70	1.77	[Rup13] SR21	1.65	1.20	1.20

Design of slender and squat reinforced concrete members with shear reinforcement

	LoA I	LoA II	LoA III		LoA I	LoA II	LoA III
test	V_{test}/V_{calc}			test	V_{test}/V_{calc}		
SR22	1.53	1.14	1.14	LG30L	1.32	1.11	1.11
SR23	1.75	1.23	1.23	LG30M	1.41	1.05	1.05
SR24	1.20	1.03	1.03	LG30H	1.43	0.86	0.86
SR25	1.40	1.16	1.16	LR30L	1.02	0.91	1.27
SR26	1.49	1.21	1.21	LR30M	1.04	0.84	0.84
SR27	1.16	1.09	1.09	LR30H	1.24	0.80	0.80
SR28	1.78	1.02	1.02	LG60L	1.00	0.94	0.94
SR29	1.22	1.05	1.05	LG60M	1.20	0.95	0.95
SR30	1.21	1.03	1.03	LG60H	1.34	0.81	0.81
SR31	1.86	1.20	1.20	GD90L	1.18	1.11	1.66
SR31B	1.82	1.18	1.18	GD90M	1.26	1.08	1.08
SR32	1.52	0.86	0.86	GD90H	1.54	1.11	1.11
[Fer08] SH1	1.10	1.00	1.00	[Bac80] V6002W	1.85	1.31	1.59
SH2	0.94	0.89	0.89	V6002E	1.91	1.35	1.64
SH3	1.11	1.02	1.02	V6004W	1.44	1.19	1.72
SH5	1.28	1.13	1.13	V6004E	1.64	1.35	1.95
[Kau96] VN1	1.25	1.00	1.00	U6004W	1.69	1.39	1.86
VN2	1.35	1.06	1.06	U6004E	1.79	1.47	1.96
VN3	1.33	1.05	1.05	U6007W	1.15	1.09	1.09
VN4	1.16	1.04	1.04	U6007E	1.23	1.16	1.16
[Sør74] T21	1.25	1.06	1.06	U6010W	1.24	1.14	1.14
T22	1.30	1.10	1.10	U6010E	1.22	1.12	1.12
T23	1.59	1.24	1.24	U6017W	1.14	1.05	1.05
T3a	1.36	1.22	1.22	U6017E	1.14	1.00	1.00
T4a	0.99	0.98	0.98	U6007cW	1.18	1.16	1.16
T1b	1.40	1.23	1.23	U6007cE	1.18	1.16	1.16
T2b	1.45	1.27	1.27	U6010cE	1.18	1.12	1.12
T3b	2.06	1.52	1.52	U6013cW	1.25	1.05	1.05
T4b	1.79	1.35	1.35	U6013cE	1.14	0.96	0.96
T5	1.84	1.37	1.37	U6017cW	1.13	0.95	0.95
[Leo63] TA1	1.53	0.98	0.98	U6017cE	0.97	0.81	0.81
TA2	1.46	1.07	1.07	U6023cW	1.04	0.82	0.82
TA3	1.35	1.13	1.13	U6023cE	1.04	0.82	0.82
TA4	1.35	1.25	1.25	U6029cW	1.13	0.89	0.89
TA13	1.33	0.92	0.92	U6029cE	0.99	0.78	0.78
TA14	1.31	1.02	1.02	U6044cW	1.15	0.76	0.76
TA15	1.32	1.14	1.14	U6044cE	1.15	0.76	0.76
TA11	1.34	1.32	1.32	U6007hW	1.25	1.18	1.18
TA12	1.31	1.21	1.21	U6007hE	1.29	1.22	1.22
TA6	1.15	0.96	0.96	U6010hE	1.06	0.98	0.98
TA16	1.33	1.15	1.15	U6017hW	1.01	0.88	0.88
[Wal13] AE30L	1.10	0.98	0.98	U6017hE	0.96	0.84	0.84
AE30M	1.43	1.00	1.00	U4213mW	1.25	0.96	0.96
AE30H	1.54	0.92	0.92	U4213mE	1.20	0.92	0.92
GD30L	1.44	1.22	1.22	U4222mW	1.48	0.96	0.96
GD30M	1.42	0.96	0.96	U4222mE	1.31	0.85	0.85
GD30H	1.47	0.88	0.88	U4230mW	1.31	0.82	0.82

	LoA I	LoA II	LoA III		LoA I	LoA II	LoA III
test	V_{test}/V_{calc}			test	V_{test}/V_{calc}		
U4230mE	1.19	0.74	0.74	T4	2.04	1.31	1.61
U4244mW	1.37	0.84	0.84	T5	1.30	1.11	1.11
U4244mE	1.37	0.84	0.84	T6	1.20	1.18	1.18
X6009W	1.30	1.17	1.17	T7	2.10	1.38	1.68
X6009E	1.40	1.26	1.26	T8	2.48	1.55	1.81
X6018W	1.61	1.36	1.36	T9	1.54	1.43	1.43
X6018E	1.50	1.26	1.26	T10	2.42	1.46	1.66
X9032W	1.38	0.96	0.96	T13	1.67	1.46	1.46
X9032E	1.53	1.06	1.06	T15	2.08	1.36	1.36
X9043W	1.43	0.98	0.98	T16	2.77	1.56	1.56
X9043E	1.56	1.08	1.08	T17	1.34	1.14	1.14
B6009W	1.20	1.20	1.20	T19	2.26	1.47	1.47
B6009E	1.06	1.07	1.07	T20	1.53	1.27	1.27
B9025aW	1.19	1.01	1.01	T25	2.14	1.30	1.55
B9029W	1.32	0.97	0.97	T26	1.79	1.25	1.25
B9040W	1.49	1.03	1.03	T27	1.60	1.48	1.48
U5617iW	1.25	1.08	1.08	T31	1.77	1.17	1.52
U5617iE	1.28	1.12	1.12	T32	1.22	1.22	1.22
U5604pW	1.57	1.43	1.43	T34	2.24	1.39	1.39
U5604pE	1.45	1.31	1.31	T35	2.29	1.45	1.45
R5651W	1.83	1.17	1.17	T36	1.79	1.56	1.56
R5651E	1.70	1.09	1.09	T37	1.09	1.12	1.12
[Lev89] RC30A1	1.18	0.94	0.94	T38	1.28	1.30	1.30
RC30A2	1.20	0.95	0.95	W1	1.45	0.91	0.91
RC60A1	1.18	1.08	1.08	W3	1.27	0.85	0.85
RC60A2	1.12	1.02	1.02	W5	1.49	0.95	0.95
RC60B1	1.19	0.98	0.98	W6	1.23	0.78	0.78
RC60B2	1.25	1.03	1.03	W7	1.27	0.81	0.81
RC70B1	1.26	1.06	1.06	[Bre63] BSA2	2.20	1.29	1.29
[De15] B104	1.78	1.41	1.66	BSB1	1.82	1.17	1.17
B105	1.59	1.26	1.26	BSB2	1.64	1.08	1.08
[Pla71] R8	1.48	1.02	1.40	BSC1	1.38	0.96	0.96
R9	0.97	0.85	0.85	BSC2	1.47	1.02	1.02
R10	1.40	0.97	1.43				
R11	1.67	1.13	1.45				
R13	1.49	1.15	1.15				
R15	1.39	1.10	1.10				
R16	1.39	1.09	1.09				
R17	1.30	1.12	1.12				
R20	1.67	1.06	1.28				
R21	1.49	1.04	1.04				
R22	1.48	1.03	1.03				
R24	1.84	1.16	1.16				
R25	2.08	1.32	1.53				
R27	1.06	0.98	0.98				
R28	0.93	0.93	0.93				
T1	2.05	1.40	1.90				
T3	1.95	1.34	1.80				

Nomenclature

Latin characters: lower case

a	shear span
a_v	clear shear span
b_w	width of web
$c_{p, inf}$	width of the support plate
$c_{p, sup}$	width of the loading plate
d	effective cross section depth
f_c	uniaxial compressive concrete strength
f_{ck}	characteristic values of the uniaxial compressive concrete strength
f_{cm}	mean uniaxial compressive concrete strength
f_{cp}	uniaxial effective concrete strength
f_{yw}	yield stress of the shear reinforcement
f_{ywh}	yield stress of the horizontal web reinforcement
f_{yvw}	yield stress of the vertical shear reinforcement
h	height of the beam
h_c	direct strut thickness
$k_{1(2)}$	calibration coefficients of the reduction factor ν
$l_{s,act}$	length of the activated shear reinforcement
n	number of activated shear reinforcement units
q	uniformly distributed load
s	spacing of the shear reinforcement units
z	lever arm of internal forces

Latin characters: upper case

A, D	inclined projection of deviated struts
A_{sw}	area of shear reinforcement unit
B, C	inclined projection of node dimensions
B_n	width of node
C_2	force in compression chord in the middle of the shear span
E_s	modulus of elasticity of steel
F_{sh}	force in the horizontal web reinforcement
F_{sv}	force in the vertical shear reinforcement
H_m	m -inclined projection of the compression field
H_n	height of node
H_α	α -inclined projection of the compression field
T_1	force in the tension chord close to the support

T_2	force in the tension chord in the middle of the shear span
V	shear force
V_c	contribution of concrete in compression in VAT models
V_c	shear force carried by direct strut
V_{Ed}	design acting shear force
V_{fan}	shear resistance governed by crushing in fan regions
$V_{max,cp}$	shear resistance governed by node crushing under concentrated loads
$V_{max,h}$	shear resistance governed by crushing of the compression field
V_R	total shear resistance
V_{Rd}	total design shear resistance
$V_{Rd,c}$	minimum design shear resistance provided by plain concrete
V_s	shear force carried by the shear reinforcement
V_s	resistance of the shear reinforcement
ΔT_2	increment of the force in the tension chord in the middle of the shear span

Greek characters: lower case

α	inclination of the force resultant accounting for the force in the shear reinforcement and the horizontal web reinforcement
β	reduction factor for acting shear force according to EC2
β	critical inclination defining the shear span
β_i	potential critical inclination i in case of multiple concentrated forces
γ	inclination of the deviated strut border
ε_1	principal tensile strain
ε_3	principal compressive strain
ε_c	longitudinal strain in the compression chord
ε_T	longitudinal strain in the tension chord
ε_x	longitudinal strain
ε_y	vertical strain / strain in the shear reinforcement
η_{fc}	strength reduction factor accounting for concrete brittleness
θ	compression field inclination
$\theta_{1(2)}$	angles of deviated compression struts
$\theta_{3(4)}$	inclinations of struts in the fan region
θ_{min}	minimum compression field inclination
ν	concrete strength reduction factor
ν_1	concrete strength reduction factor in the middle of the shear span
ν_2	concrete strength reduction factor in deviated struts and nodes
ρ_h	horizontal web reinforcement ratio
ρ_l	flexural reinforcement ratio

Design of slender and squat reinforced concrete members with shear reinforcement

ρ_w	shear reinforcement ratio
σ_{sw}	stress in the shear reinforcement
σ_{swh}	stress in the horizontal web reinforcement
σ_{swv}	stress in the vertical shear reinforcement
τ	shear stress
τ_R	shear stress at the shear failure
$\psi_{1(2)}$	$\theta_{1(2)} + \alpha$
ω_w	mechanical shear reinforcement ratio

Chapter 3

Experimental investigation of dowel action in reinforcing bars using refined measurements

This chapter represents the following publication:

Pejatović M., Muttoni A., *Experimental investigation of dowel action in reinforcing bars using refined measurements*, Structural Concrete, 2024 [submitted, December 2023]

The authors of this publication are Marko Pejatović (PhD candidate) and Prof. Aurelio Muttoni (thesis director, École Polytechnique Fédérale de Lausanne, Switzerland).

This work was conducted by the first author (Marko Pejatović) under the supervision of Prof. Aurelio Muttoni who consistently offered the constructive feedback, proofreading and manuscript revisions.

The main contributions of Marko Pejatović to this publication and chapter are the following:

- Dowel tests: preparation, casting and testing 11 specimens subjected to monotonic or low stress-level cyclic actions, including various parameters: bar diameter, imposed crack kinematics and angle between the bar and the crack.
- Preparation of the optical fibre measurement system on opposite sides of each reinforcing bar for the continuous strain measurement along the bar.
- Compression tests under the bar: preparation, casting and testing 9 specimens subjected to a point load introduced at various locations into concrete through a reinforcing bar.
- Detailed measurements by digital image correlation of the displacement field.
- Post-processing of the experimental data: interpretation and analysis.
- Elaboration of the figures and tables included in the publication.
- Manuscript preparation for the publication.

Experimental investigation of dowel action in reinforcing bars using refined measurements

- Collection of the database containing 142 dowel tests to evaluate the existing dowel models for the resistance prediction.

Abstract

In typical reinforced concrete design, reinforcement is designed to carry axial forces, but it can also resist transverse forces by dowel action. This is usually neglected for simplicity's sake in the design phase, but it can be accounted for either explicitly in mechanical models or implicitly in empirical relationships. Furthermore, there are cases where the connection between various concrete elements explicitly depends on dowel action, as for example in connections between precast elements or between two concrete parts cast at different times. On the other side, dowel action can have a negative impact on the fatigue resistance of reinforcing bars subjected to cyclic loading, because of the local stress concentrations near interfaces due to relative movements, either in sliding or in opening of cracks not perpendicular to the bar. For the assessment of the remaining capacity of existing structures, improved models of the behaviour are needed, including realistic models of the behaviour of concrete, steel and their interfaces. The aim of the present chapter is to provide a contribution to a better understanding of dowel action by two test series. The first series focused on the behaviour of the dowel: the concrete specimens with the embedded bars were placed in a custom-made test setup and subjected to monotonic or low stress-level cyclic actions with a longitudinal and a transverse crack opening component, up to developing the full plastic capacity of the dowel and rupture at the peak of catenary action. The measurement system included tracking the displacement field at the surface of the concrete and the strains in the dowel by optical fibres glued on its surface. The latter measurements allow to derive the internal forces in the reinforcing bar and deformed shape of the bar as well as the contact pressure between the bar and the surrounding concrete. The results show a strong dependency on the test variables: diameter of the bar, imposed crack kinematics and angle between the bar and the crack. The second test series looked more closely at the behaviour of concrete underneath the bar, in the presence of a point load introduced at various locations into concrete through a reinforcing bar. A comparison of the test results with existing models shows a general good agreement and some aspects that deserve to be improved.

Keywords: dowel action, cracks, structural joints, shear, fatigue, digital image correlation, optical fibres, existing structures

3.1 Introduction

The steel reinforcement in reinforced concrete (RC) structures is commonly designed to carry longitudinal forces only. Its ability to resist transverse forces by dowel action is usually neglected to simplify the structural design and the assessment of existing structures. Dowel action is the transmission of transverse forces in a reinforcing bar on either side of cracks (Fig. 3.1a), in connections of precast elements (Fig. 3.1c), at the interface between two concretes cast at different times, etc. (Fig. 3.1b), where a relative displacement component

perpendicular to the bar axis occurs. Reinforcing bars can also be designed to carry transverse forces at the ultimate limit state (Fig. 3.1c,d), provided the concrete embedment is strong enough. If cracks or joints are subjected to cyclic loadings, for instance due to traffic loads, stress concentrations due to dowel action can lead to fatigue failures of the reinforcing bars.

Simplified design formulae in codes of practice [Eur04, FIB13, SIA13] are typically conservative, underestimating the actual structural resistance for most cases. This can become problematic for the assessment of existing structures, because underestimating the actual strength can lead to unnecessary retrofitting measures, with the associated costs. This is why more refined models are needed, allowing to accurately estimate the actual resistance. In some cases, the analytical verification can be complemented with in-situ measurements. This is typically the case for the fatigue verification, where the stress variations in the steel reinforcement can be estimated on the basis of detailed measurements on the concrete surface. Directly gluing strain gages on reinforcing bars is impractical as it implies a significant disturbance of the bond behaviour and the dowel action. This is why more refined models of dowel action are needed to reliably evaluate the resistance of the existing structures at the ultimate and fatigue limit states.

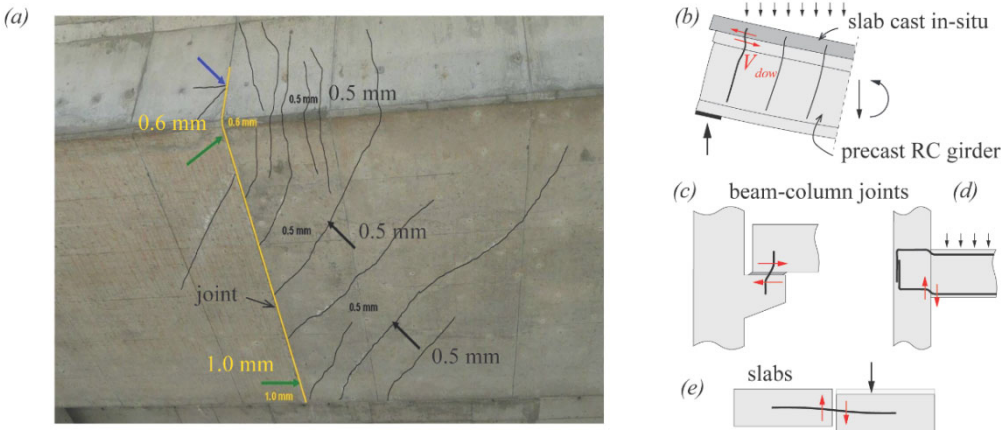


Figure 3.1: (a) Cracks due to torsion in the Weyermannshaus Viaduct (Bern, Switzerland) and (b-e) other cases where dowel action can occur.

Previous investigations have often focused on dowel action at the ultimate limit state under monotonic or cyclic loads (e.g. due to seismic actions). Three failure modes are generally distinguished (Fig. 3.2): (1) splitting of the concrete cover for dowel forces parallel to the free surface, (2) spalling of concrete perpendicular to the free surface and (3) local crushing of concrete in combination with yielding of the dowel bar in bending.

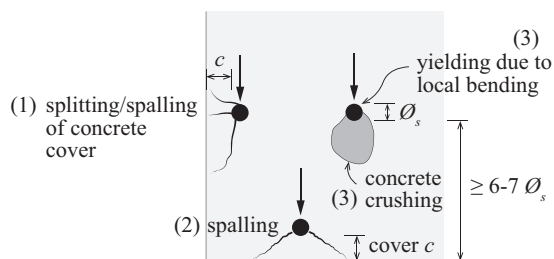


Figure 3.2: Failure modes due to dowel action.

The first two failure modes typically occur for concrete covers smaller than 6-7 times the bar diameter [Vin86]. In this case, the dowel resistance was observed to depend on the bar diameter, the concrete strength, the thickness of the cover, the crack kinematics (crack opening and relative displacement parallel or perpendicular to the free surface), etc. [Mar51, Kre66, Tay69, Bau70, Dei93, Aut23]

If the concrete cover is larger than 6-7 times the bar diameter, splitting and spalling failures are prevented. In this case, relatively large imposed transverse displacements can be reached leading to plastic hinges in the steel bar due to local bending. At the same time, local crushing of the concrete occurs under the bar, near the crack (or the interface between concretes cast at different times) [Ras62, Sor86, Dul72, Sor17, Dei87, Dei92, Hof69, Tan11, Pru88, Nør15, Vin87, Czi83]. In this case, most of the concrete reaction is provided over a length of approximately two bar diameters from the crack, where the plastic hinge is located [Vin84]. If the dowel is not perpendicular to the crack, its resistance decreases [Dul72]. Significant concrete strains associated to concrete crushing can be observed, up to a depth of around half a bar diameter from the crack [Dei92]. The effect of an axial force in the bar on its dowel response has also been examined: in addition to concrete crushing, larger tensile axial forces also degrade the dowel response, as they reduce the stiffness of the concrete embedment due to the development of micro cracks around the bar associated to the bond stresses [Got71, Mae96, Mae96a]. In addition, the bending resistance of the bar which contributes to the dowel resistance is reduced by the presence of an axial tensile force [Sha69, Kem77, Tak19, Mae96, Mae96a]. The activation of the second-order catenary action in a dowel bar has also been observed for large transverse displacements. If the axial tensile force in the bar reaches the plastic axial force, the bending capacity of the dowel disappears. Under these conditions, the catenary action is the only remaining contribution to the dowel resistance [Sor17]. If the bar is subjected to large cyclic stresses, the dowel response is notably degraded after only a couple of cycles, because of yielding of the dowel and local concrete crushing [Vin86, Vin87, Tak19].

The stiffness and the strength of the concrete embedment have also been investigated and their values exhibit a large scatter. They were observed to depend on multiple parameters including the bar diameter, the compressive concrete strength, the confinement level, the magnitude of the imposed displacements, etc. [Sor87].

The modelling of the dowel mechanism has been investigated by numerous authors. The elastic solution was developed based on the analysis of a beam on elastic foundation [Tim25, Fri38, Win67, Zim88]. The dowel resistance at the ultimate limit state was calculated using the principles of limit analysis [Ras62, Nør15, Sor17, Nie11]. Existing predictions of fundamental load-displacement relationships are typically based on empirical formulations. This particularly concerns the evolution of the stiffness of the concrete embedment [Vin86, Sor86, Dul72, Dei87, Dei92]. More general models account for the interaction between the axial force and the dowel force [Mae96, Mae96a].

With respect to its phenomenology, further in-depth understanding of dowel action in the confined concrete embedment is still required. This particularly concerns the contribution of the dowel action to carry shear forces and its influence on steel stress variations, which can potentially lead to a fatigue failure.

To that purpose, this chapter presents the results of an experimental investigation of dowel action in a confined concrete embedment (with sufficient concrete cover) subjected to monotonic loading up to failure and low-stress cyclic loading. This includes cutting-edge measurement techniques: Three-Dimensional Digital Image Correlation (DIC-3D) [Non13] and optical fibre sensors [Can20, Bad21, Lem22]. They allow for precise measurements of, respectively, the complete 3D-displacement field of the cracked concrete surface and the continuous strain distribution in the steel reinforcement. The dowel test series consisted of bars embedded in concrete blocks designed to prevent concrete spalling and to limit the risk of concrete splitting. They were subjected to low-stress level cycles and/or monotonic loading up to the bar rupture due to excessive catenary action. Imposed axial and shear forces were selected in the cyclic tests to match typical service load scenarios. The results of an additional test series, aimed at investigating the local concrete behaviour and resistance under the bar, are also reported in this chapter. The modelling of dowel action at ultimate and fatigue limit states will be the subject of a future work by the authors.

3.2 Experimental programme

The experimental programme was carried out at the Structural Concrete Laboratory of the École Polytechnique Fédérale de Lausanne in Switzerland. It consisted of two different test campaigns: the first investigated the dowel action (DP series) and the second studied the stiffness and strength of concrete under a rebar (CP series).

3.2.1 Specimens and test set-ups

The main design idea for the specimens of both series was to reproduce the behaviour of confined structural details at cracks or member interfaces, as shown in Fig. 3.1. The laboratory tests of DP series (dowel action) were performed using 11 concrete block specimens (Fig. 3.3b-e). Each specimen contained a single ribbed reinforcing bar of diameters $\varnothing_s = 20$ mm or 14 mm subjected to dowel action. Each bar was 500 mm long and was symmetrically embedded in a 300 mm concrete block. The reinforcing bars subjected to dowel action had threaded ends which allowed anchoring them to the testing machine (Fig. 3.3a). Each concrete block (Fig. 3.3c-e) was in two parts, separated by a smooth pre-made notch with a thin concrete layer around the bar to simulate the crack. The notch was created by placing steel sheets in the formwork during the casting of concrete, and removing them after hardening of the concrete. This ensured that there was no transfer of stresses by the aggregate interlock. The angle between axis of the bar and the crack (θ , Fig. 3.3a) was 45° , 70° or 90° . The casting direction of the specimens is shown in Fig. 3.3c. To prevent a global splitting failure of the concrete, each half of the specimen was reinforced by four stirrups ($\varnothing 10$ mm, Fig. 3.3c-e). To align the applied shear force with its horizontal reaction, the specimens were confined using steel plates fixed by threaded steel bars (Fig. 3.3a), which allowed controlling the global rotation of the specimens. The external confining bars were fixed sufficiently far from the pre-made crack that they did not affect the dowel response. The properties of the specimens are summarised in Table 3.1.

The specimens were tested in a test setup (Fig. 3.3a) that was derived from that previously used to investigate aggregate interlocking and local bond behaviour [Tir21, Pun19]. The testing machine has a stiff steel frame with three vertical columns, rigidly connected by the steel caps. Two perpendicular hydraulic jacks were fixed to the machine frame and enabled to apply displacements in two independent directions. A set of rollers prevented unwanted rotations. The vertical jack was attached to the bottom steel cap. Its tensile capacity was close to 1 MN for static loading. The vertical jack allowed applying the axial force by pulling on the vertical reinforcing bar. The bar was fixed to two steel anchoring plates (Fig. 3.3a) using small steel plates and nuts screwed on both threaded bar ends. The anchoring steel plates (500 x 500 x 50 mm) had slits to enable the placement of the specimens on the test machine. The horizontal jack used to impose the transverse displacement had a 0.3 MN compression capacity for the static loading (no tensile force was applied). It was fixed to two frame columns of the test machine while the third frame column was used as a horizontal support.

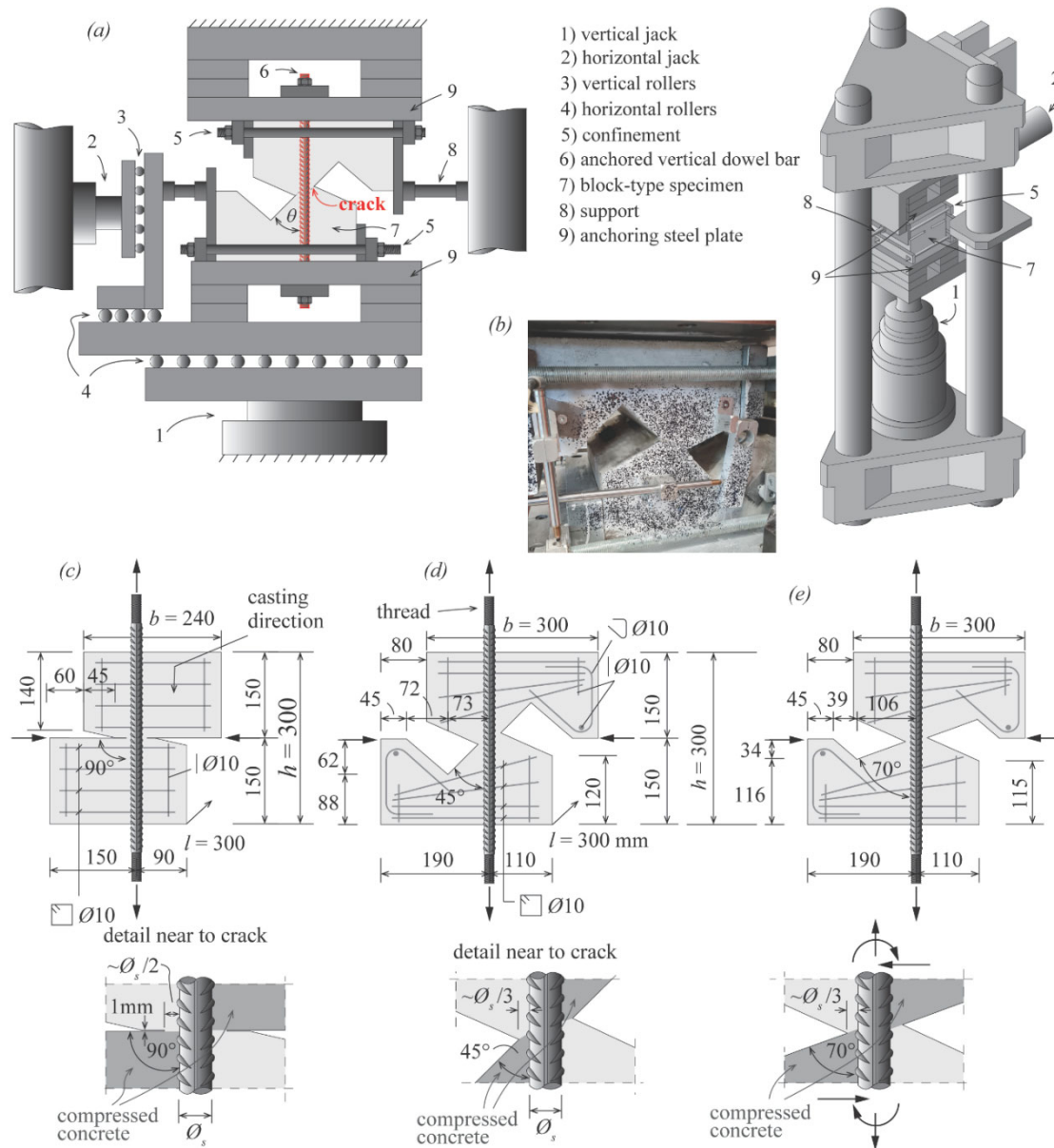


Figure 3.3: Test set-up and specimens for dowel DP tests: (a) test set-up; (b) photo of a specimen; and geometry of specimens, reinforcement and applied forces for (c) 90° ; (d) 45° and (e) 70° specimens (dimensions in mm).

The second experimental campaign (CP series), aimed at investigating the concrete behaviour under a steel reinforcing bar, consisted of 9 specimens. Each specimen contained a single reinforcing bar ($\varnothing_s = 20$ mm, length: 120 mm) horizontally embedded on top of the concrete block (Fig. 3.4). The concrete blocks were shaped so that the acting and reacting forces were vertically aligned. The embedded bar was welded to a steel profile with a rectangular cross-section (120 x 30 x 20 mm, Fig. 3.4a). This allowed applying the point load along the bar causing small bending deformations. It also provided a vertical surface for DIC measurements of the bar

kinematics as the bar itself was hidden in concrete. The concentrated force was applied at various locations along the axis of the bar (distance a from its end, Fig. 3.4a). In all tests of this series, the concrete surface representing the crack surface was perpendicular to the bar ($\theta = 90^\circ$) and was aligned with the end of the bar. The specimens were confined by horizontal reinforcing bars and stirrups ($\varnothing 8$ mm) to prevent a brittle global splitting failure. The specimens were cast from the side and turned by 90° to be tested (casting direction shown in Fig. 3.4a). Relatively small casting height with respect to the bar ensured good concrete conditions around the bar, preventing notable voids due to bleeding and fresh concrete settlement [Moc21]. The specimens of the CP series were tested using a Schenck test machine with a compression capacity of 2.5 MN. The point load on the investigated bar was applied under displacement control.

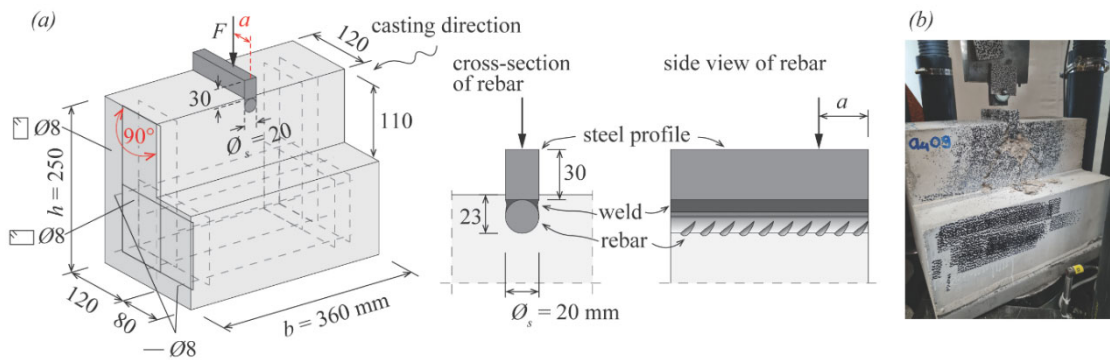


Figure 3.4: Specimens for CP tests: (a) geometry, reinforcement and applied force and (b) photo of a specimen.

3.2.2 Material properties

Normal strength concrete with crushed aggregates with the maximum size of 16 mm was used for all specimens. The uniaxial compressive concrete strength f_{cm} was measured on cylinders ($\varnothing 160 \times 320$ mm). Their mean values at the time of testing were 36.3 MPa and 27.5 MPa for the DP and the CP series, respectively (details are given in Tables 3.1 and 3.2).

Conventional ribbed steel rebars were used for both test series. Figure 3.5a shows the experimental stress-strain relationships for the two used diameters.

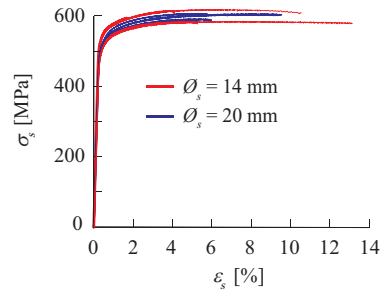


Figure 3.5: Stress-strain relationships of the reinforcement.

Table 3.1 summarises the main test variables and properties of the DP test series: angle θ between the bar and the crack, bar diameter \varnothing_s , mean concrete compressive strength f_{cm} , yield strength of the dowel bar f_y , tensile strength of the dowel bar f_u , ultimate first-order dowel force $V_{dow L,u}$ (without the contribution of catenary action), test type, angle α defining the applied crack kinematics in monotonic tests (see section 3.3 and Fig. 3.9), initial crack opening component in the direction of the reinforcement $\delta_{\parallel, init}$ and initial global axial force N_{init} . The first two digits in the name of the specimens refer to the bar diameter while the last two are the serial number.

Table 3.1: Properties of dowel tests (series DP).

Test	θ [°]	\varnothing_s [mm]	f_{cm} [MPa]	$f_y^{1)}$ [MPa]	f_u [MPa]	test type	α [°]	$\delta_{\parallel, init}$ [mm]	N_{init} [kN]	$V_{dow L,u}$ [kN]
DP2001	90	20	33.6	524	606	monotonic	0	0.08	47.1	76.1 ²⁾
DP2002			33.9				15	0.20	78.8	63.8
DP2007	70		37.3	0	0.20	122	51.5 ²⁾			
DP2008	45		38.3	0	0.20	120	32.8			
DP2022	90	34.9	520	590	cyclic / monotonic	0	0.15	98.1	52.5 ²⁾	
DP2027	45	36.2					0.10	51.1	35.5	
DP1403	90	14	35.6	510	584	monotonic	30	0.20	42.6	18.6 ²⁾
DP1404			35.5				0	0.20	40.2	30.2 ²⁾
DP1411	45		38.9	0	0.20	51.4	19.0			
DP1437	45		38.4	547	618	cyclic / monotonic	0	0.20	38.7	18.1
DP1440	90	36.8	0.10					21.5	25.1 ²⁾	

¹⁾ The yield strength is taken at 0.2% residual strain.

²⁾ Based on the shear force without catenary action (see Fig. 3.8 for tests without clearly defined plateau).

Table 3.2 summarises all relevant properties related to the CP test series including the position of the point load a , the compressive concrete strength f_{cm} and the peak load F_u .

Table 3.2: Properties of tests of concrete behaviour under a rebar (series CP).

Test	\varnothing_s [mm]	a [mm]	f_{cm} [MPa]	F_u [kN]
CPa101	20	18	26.7	87.0
CPa102		18	26.7	78.5
CPa104		18	27.9	87.1
CPa205		31	27.3	146.5
CPa206		30	27.9	150.4
CPa307		44	27.9	213.9
CPa308		45	27.3	193.1
CPa409		60	28.5	270.5
CPa410		60	27.3	254.1

3.2.3 Measurements

For the DP series, the applied forces were measured by load cells while 3D Digital Image Correlation was used to measure the displacement field in three perpendicular directions [Mat20, Can20]. The DIC was used to track displacements of the concrete surface around the crack (Fig. 3.6b). A pair of digital cameras SVCam-hr29050 (29 megapixels) were used. The black speckle dots had the diameter of around 2-3 mm. The pixel size of the images was in the range from 0.155 mm to 0.220 mm. The acquisition rate of the cameras was in the range of 1-2 Hz up to the ultimate dowel force. Thereafter, when the catenary action started to increase, it was decreased to 0.5 Hz up to the final bar rupture. The VIC-3D software was used to analyse and post-process the acquired images [Cor10]. Before each test, a sufficient number of images of the unloaded specimens was taken to verify the noise level of the measurement. The mean noise value of maximum and minimum displacements was around 1/70 and 1/20 of a pixel size for in-plane and out-of-plane displacements, respectively.

In addition, optical fibres were used to continuously follow the longitudinal strains in the dowel (Fig. 3.6a,b). The software Odisi-B by Luna Innovations [Lun13] was used to analyse the results. This software is based on Optical Frequency Domain Reflectometry which treats optical light paths and reflection characteristics. This allows for the refined measurements with the high frequency and the sufficiently large spatial resolutions [Can20, Bra19, Bad21, Bad21a]. In this work, the spatial resolution was chosen as the gage pitch of 0.65 mm for all the specimens. Optical fibres (125 μm diameter) were glued inside grooves milled on two opposite sides of the reinforcing bar (Fig. 3.6a,b, see green and blue colours). The grooves were 1 mm wide and 2 mm deep. The fibres were placed using a two-component glue. In some specimens, the fibres were additionally protected by a soft silicon layer along the groove. This allowed reducing the perturbation of the optical fibre measurement due to the stress concentrations at the ribs. More information about the adopted fibre installation process can be found in [Can20].

Four vertical LVDTs were used to control the imposed crack opening component δ_{\parallel} (relative displacement between the two crack faces in the direction of the bar axis, Fig. 3.6b). Two of them were fixed on the front and two on the back side of the specimen. A pair of horizontal LVDTs were used to control and measure the transverse displacement (δ_{\perp} , relative displacement between the two sides of the crack perpendicular to the bar axis).

For the CP series (Fig. 3.6c), in the DIC measurement pixel size was somewhat less than 0.1 mm for all specimens. The rest of the DIC properties were similar to those of the DP series. The speckle pattern for the measurement was applied: on the front vertical concrete surface below the end of the bar, on the front cross-section of the bar and on the vertical side of the welded steel piece along the bar axis. This enabled the DIC measurements to follow the in-plane and out-of-plane displacements of the concrete surface, the penetration of the bar end into the concrete δ and the kinematics of the bar welded to the steel profile.

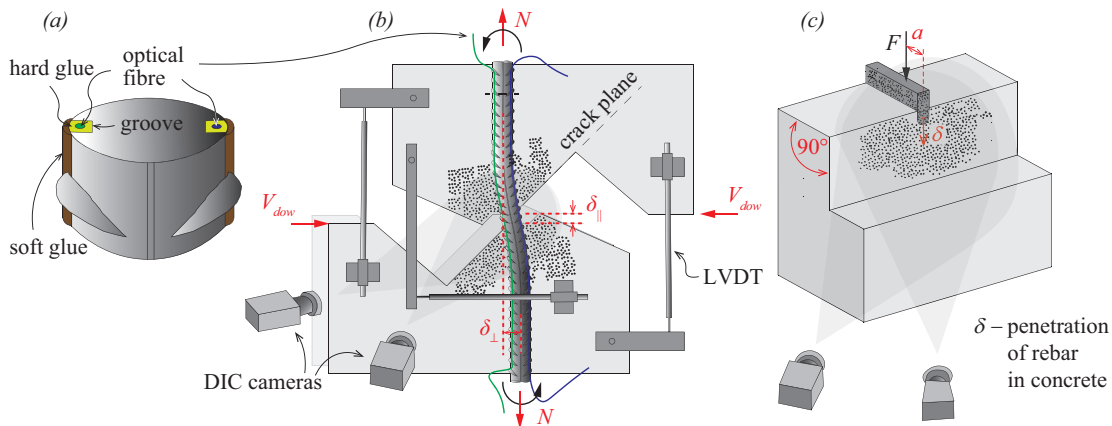


Figure 3.6: Measurements: (a) optical fibres glued on the reinforcing bar; (b) DIC and LVDTs measuring $\delta_{\parallel} / \delta_{\perp}$ ratios in DP series and (c) DIC measurement in CP series.

3.3 Experimental results

The results of the dowel tests (DP) are divided in two groups, depending on their loading regime: monotonic and cyclic tests. The test results of the concrete behaviour under the bar (CP) are presented in another subsection.

3.3.1 Monotonic dowel tests

The monotonic dowel tests were conducted under controlled displacement to follow the full dowel response up to the bar rupture. The monotonic tests were carried out in two phases. In the

first phase (called MI for Mode I), the bar was pulled to impose a specified initial crack opening component $\delta_{\parallel, init}$ in the direction of the reinforcement. In the second phase, a gradually increased transverse displacement δ_{\perp} (crack opening component perpendicular to the reinforcement) was applied. The opening component δ_{\parallel} was either simultaneously incremented proportionally with δ_{\perp} in Mixed-Mode (MM) or kept approximately constant in Mode II (MII).

Figure 3.7 shows the results of the monotonic dowel tests in terms of the shear force V_{dow} and the global axial force N , as a function of the transverse displacement δ_{\perp} . The results are shown for the specimens with various crack-bar angles θ and bar diameters \varnothing_s . Figure 3.7a,c shows the response up to a transverse displacement $\delta_{\perp} = 3$ mm, whereas Fig. 3.7b,d shows the full dowel response up to the bar rupture.

It can be observed that the dowel response is linear-elastic for small imposed transverse displacements (small shear forces). As the force increases, the bar reaches its yield strength and the concrete embedment starts crushing locally under the bar, close to the crack. These two phenomena reduce the initial stiffness of the dowel response (Fig. 3.7a). An almost horizontal plateau in the shear force – transverse displacement relationship is reached when a plastic hinge develops in the reinforcement and the concrete strength is reached (in accordance with Rasmussen's model [Ras62]). The plateau is clearly visible for tests with cracks inclined with respect to the bar, whereas for cracks perpendicular to the bar, the shear forces slightly increased. The load defined by the plateau, which is characterized by a negligible second-order catenary action is defined as first-order resistance $V_{dow1,u}$. Figure 3.7b shows that after reaching this plateau, the dowel force can be further increased by activating the catenary action related to a significant displacement (transverse displacement larger than approximately one bar diameter). This is enabled by the fixed bar ends which reproduce the typical boundary conditions in most structural RC cracked members (sufficient anchorage away from the crack). The tests typically finished with the bar rupture close to the crack. This occurs at the cross-section with the maximum combination of local axial strains due to bending and the local axial force. The axial force measured at the edges of the specimen (in the direction of the undeformed bar) was observed to decrease up to the transverse displacement δ_{\perp} reached approximately $\varnothing_s/2$ and increased thereafter showing the activation of the catenary action (Fig. 3.7c,d). This decrease of the axial force can be explained by the loss of the bond between the concrete and the bar as the transverse displacement increases (δ_{\parallel} was an imposed displacement). In addition to that, when the bar's most stressed cross-section is fully plasticized (refer to the plastic domain in Fig. 3.8g), the axial force reduces due to the plastic deformation associated to the local bending of the bar. For the transverse displacement δ_{\perp} larger than approximately half of the bar diameter, the axial force increases again due to the local elongation associated with the catenary action.

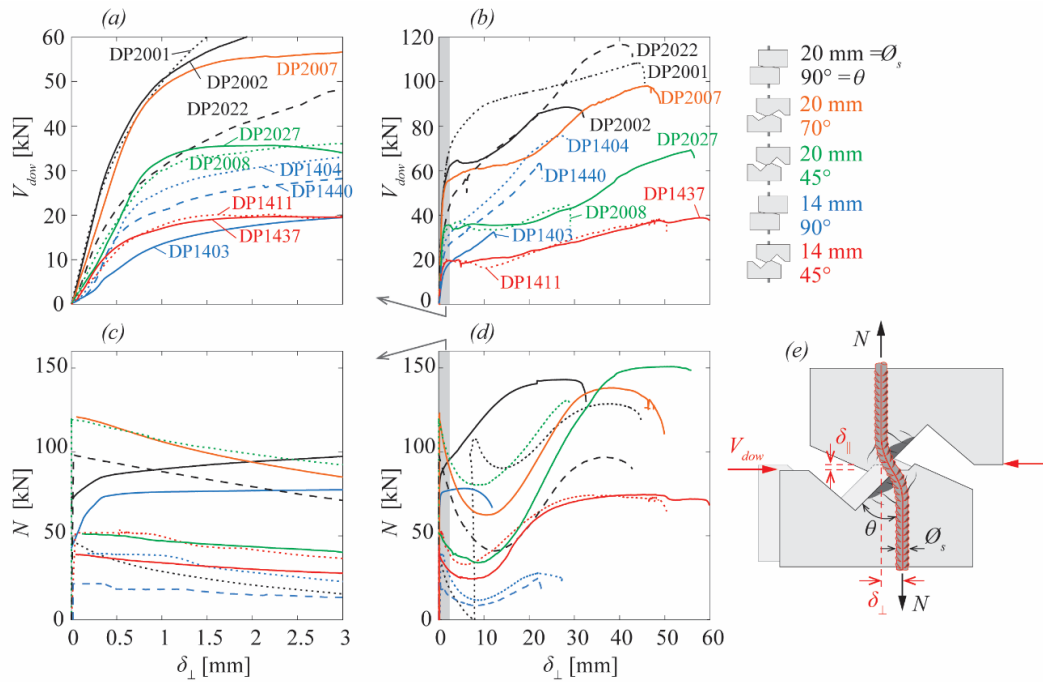


Figure 3.7: Monotonic test results - dowel force V_{dow} and global axial force N as a function of the transverse displacement for: (a,c) elastic and plastic response up to a displacement $\delta_{\perp} = 3 \text{ mm}$ and (b,d) complete response up to failure; (e) main crack kinematic parameters and forces.

For large transverse displacements, the dowel resistance results from two components. The first-order component (V_{dowI}), is related to a shear force in the reinforcing bar while the catenary action ($V_{dow,cat}$) corresponds to the transverse component of the inclined local axial force in the rotated bar in the plane of the crack (N' , Fig. 3.8f). It can be calculated using the equilibrium of forces on the deformed bar configuration (rotation ψ , Fig. 3.8f). It can be observed that the local axial force in the bar frequently reaches the axial yield strength ($N_p = \pi \varnothing_s^2 f_y/4$) between the plastic hinges. This occurs due to the elongation related to the large transverse displacement of the catenary action. Consequently, in this configuration, the cross-section of the bar is not able to resist any bending moment (Fig. 3.8c) and the dowel resistance is provided by the sole catenary action.

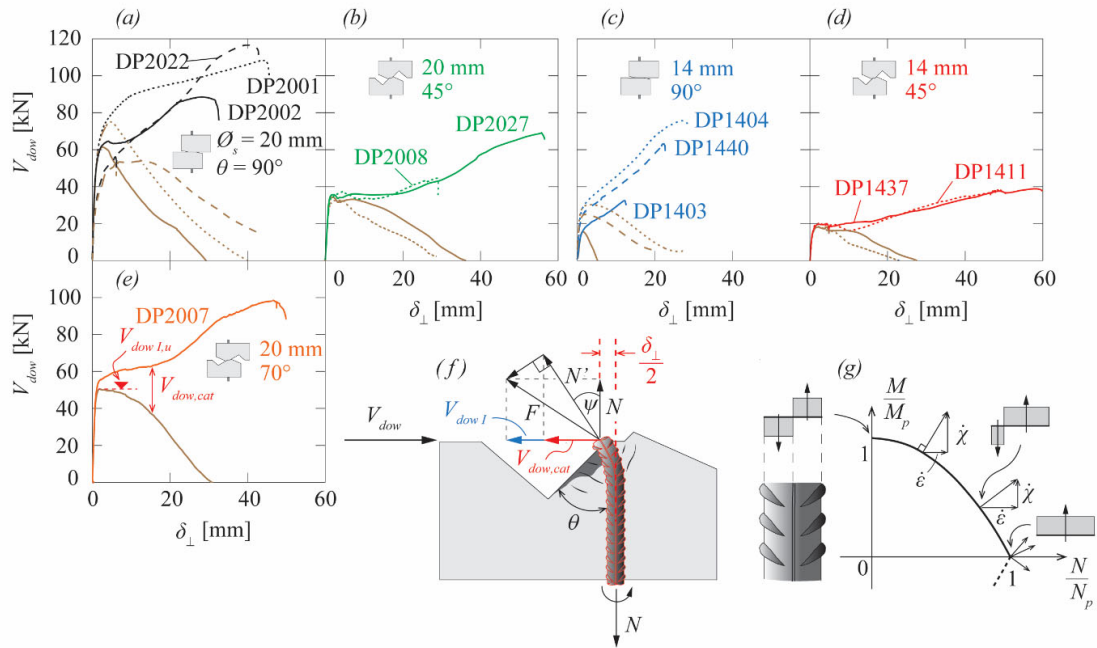


Figure 3.8: (a-f) Catenary action in monotonic tests as a function of transverse displacement and (g) yield domain of a round cross-section of a reinforcing bar.

Effect of the angle between the bar and the crack

To underline the influence of the angle between the bar and the crack, the responses of three specimens with the same bar diameter (20 mm), displacement protocol ($\alpha \approx 0$), but variable angles ($\theta = 45^\circ$, 70° and 90°) are shown in Fig. 3.9. The results are shown in terms of the average shear stress as a function of the normalized transverse displacement. Tests DP2001 and DP2007 experienced a rupture of the bar due to catenary action whereas the test DP2008 experienced a premature failure triggered by the rupture of the anchorage at the end of the bar. These experiments show that the angle of the crack has a significant influence on the initial stiffness and on the final dowel resistance. Cracks perpendicular to the bar correspond to a stronger and stiffer concrete embedment under the bar, which limits concrete cracking and crushing. On the contrary, smaller angles cause a decrease in both dowel resistance and initial stiffness.

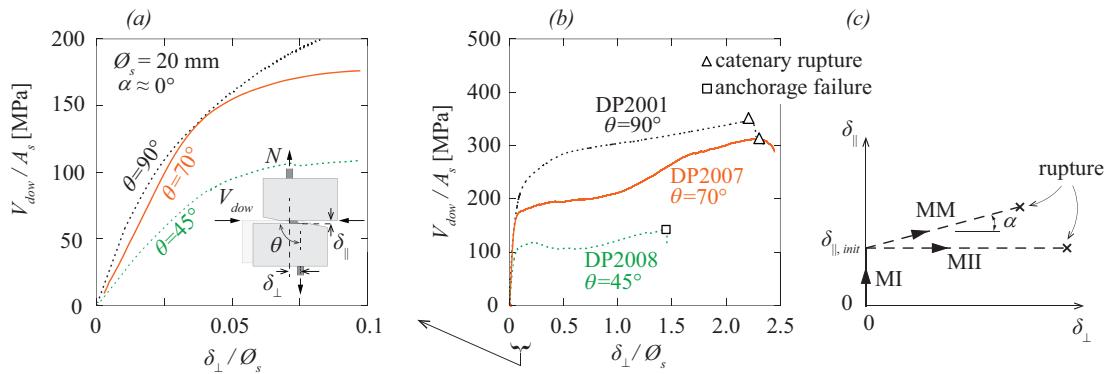


Figure 3.9: Monotonic tests: shear stress in the reinforcing bar as a function of the normalized transverse displacement for three specimens with various angles between the bar and the crack: (a) initial stiffness; (b) complete behaviour up to failure and (c) displacement protocol for monotonic tests.

Effect of the bar diameter

Figure 3.10 shows a comparison between two comparable specimens with different bar diameters ($\phi_s = 14$ mm, 20 mm). It appears that the 20 mm and the 14 mm bar exhibit a similar behaviour for small displacements in the normalized representation of Fig. 3.10a (the difference for small transverse displacements may be due to measurement inaccuracies), but the normalized resistance of the 14 mm bar is larger, showing a clear size effect.

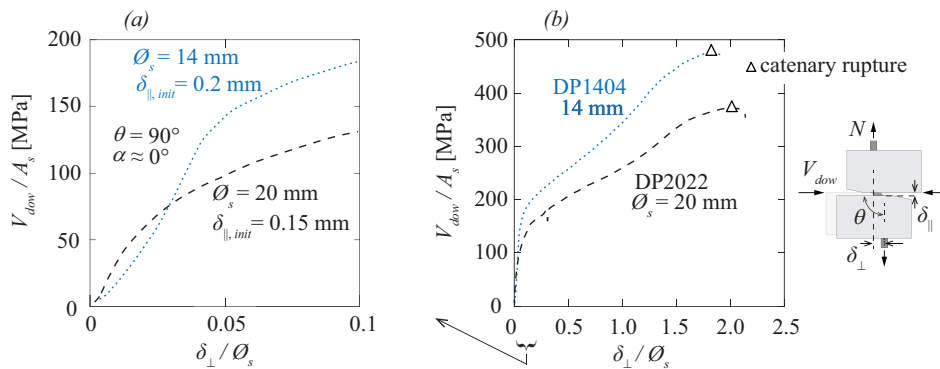


Figure 3.10: Monotonic tests: shear stress in the reinforcing bar as a function of the normalized transverse displacement for two specimens with various bar diameters ($\phi_s = 14$ mm and 20 mm); (a) initial stiffness and (b) complete behaviour.

Optical fibre measurements

Optical fibres glued on both sides of the bar (Fig. 3.6a and 3.11a) allowed for the continuous monitoring of the longitudinal strains in the monotonic tests. Figure 3.11 shows the measurement of the DP2027 test ($\varnothing_s = 20$ mm, $\theta = 45^\circ$), while the results of the other tests are shown in Appendix 3.B. Optical fibre measurements allow calculating the distribution of internal forces in the bar (assuming a bilinear stress-strain relationship for steel according to Fig. 3.11j, see results in Fig. 3.11c,d,e), the contact pressure on the concrete embedment exerted by the bar (by double derivation of the moment in the bar, see results in Fig. 3.11f), the curvature (difference of the strains on both sides divided by the distance between fibres, see results in Fig. 3.11g), the rotation (by integrating the curvature, see Fig. 3.11h) and the deformed shape of the reinforcing bar (by integrating the rotation, Fig. 3.11i). The results are shown for five different load levels including the ultimate dowel force $V_{dow\ L,u}$. In some graphs, the raw data is presented together with smoothed values over a length of around 0.5 to 2 bar diameters [Can20, Cor23].

In the presented test, the local axial force remains approximately constant for all the considered load stages (average tensile stress around 190 MPa). The normalized axial stress due to bending (Fig. 3.11d assuming elastic behaviour) reaches a peak value in tension larger than 500 MPa, indicating yielding of the bar. The distribution of the concrete pressure is calculated as the first-order derivative of the shear force and assumed to be constant over the bar diameter (Fig. 3.11f). The peak pressure is located at a distance of approximately one bar diameter from the crack plane and has a value of around 62 MPa ($\sim 1.70 f_{cm}$).

Figure 3.11i shows the transverse displacement δ_\perp calculated by double integration of the curvature assuming zero rotation at bottom extremity and neglecting the shear deformation of the bar (solid line). The calculated transverse displacement is compared with the DIC measurements (dashed lines, Fig. 3.11i) for various load levels. The agreement between the two measurements is fairly good, showing that the procedure is reliable and that the shear deformation of the bar is negligible.

The results clearly show the two critical cross-sections with the largest bending moments in the bar (Fig. 3.11b). They are observed to be symmetrical with respect to the crack for the same concrete properties on both crack sides. The distance between the crack and the critical cross-section is approximately $1.5\varnothing_s$. This distance appears to be slightly smaller for perpendicular cracks than for inclined ones (Fig. 3.11l), due to the stiffer and stronger concrete embedment under the bar. Figure 3.11k shows that there is no evident size effect with respect to the bar diameter.

Large local axial forces in the reinforcing bar lead to reaching the yielding strain for smaller transverse displacements. On the other hand, larger local axial forces cause second-order effects for a larger imposed transverse displacement, which slightly reduce the longitudinal stresses due to the bending in the bar.

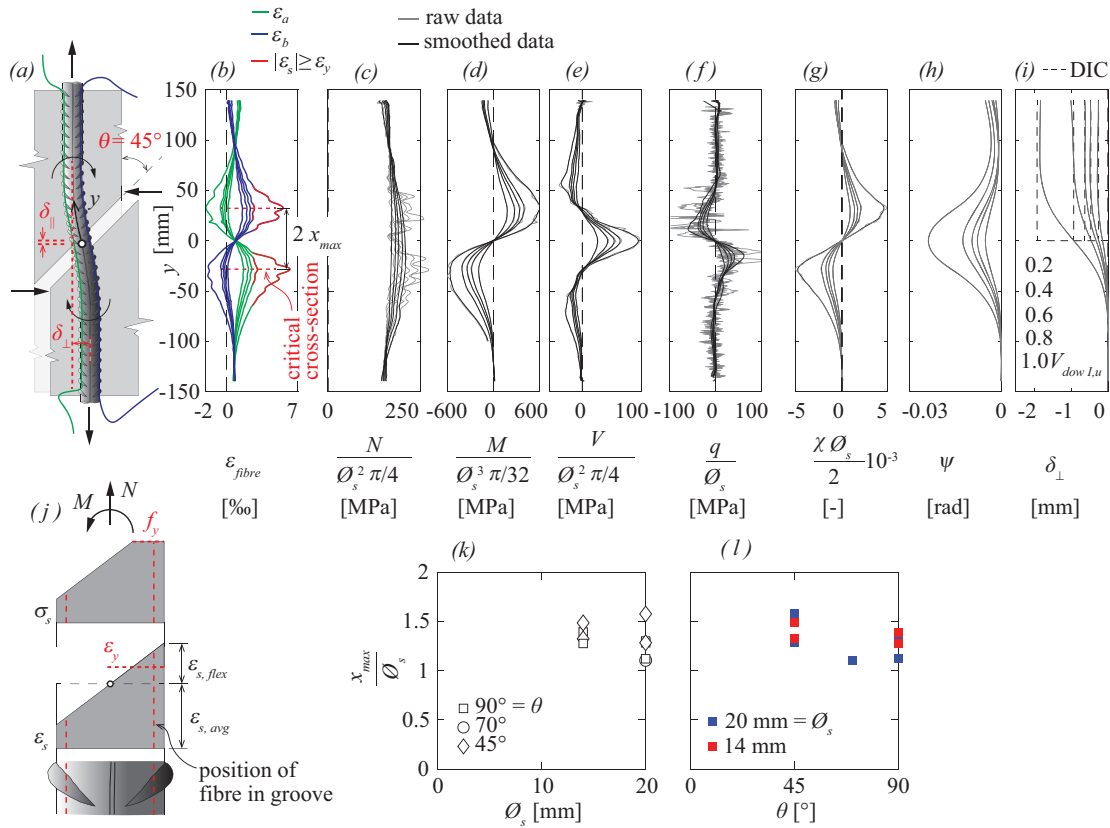


Figure 3.11: Optical fibre measurements: (a) bar deformation and parameter definitions; (b) measured strains; (c) normalized local axial force; (d) normalized moment (stress assuming an elastic behaviour); (e) average shear stress; (f) pressure between bar and concrete (averaged over the bar diameter); (g) normalized curvature; (h) bar rotation; (i) transverse displacement (dashed lines show the results of the DIC measurement); (j) assumption for calculating the internal forces; (k) distance between the crack and the critical cross-section as a function of the bar diameter and (l) as a function of angle between the crack and the bar (test DP2027 with $\Omega_s = 20$ mm, $\theta = 45^\circ$, see Appendix 3.B for the other tests).

Figure 3.12 shows the interaction diagram of the normalized bending moment and the normalized local axial force at the critical bar cross-section (position of the maximum bending moment, derived from the optical fibre measurements). The plastic bending moment of the bar with a circular cross-section can be calculated as $M_p = \Omega_s^3 f_y / 6$. The dots refer to the calculated values for steps of $0.2 V_{dow I,u}$, the last one referring to the first-order ultimate force $V_{dow I,u}$ (except for DP2007 for which optical fibres measured up to $0.9 V_{dow I,u}$). The local axial force tends to increase or to be approximately constant for small transverse displacements while it appears to slightly decrease when the critical cross-section is almost fully plasticized. It can be observed that regardless of the specimen configuration, for $V = V_{dow I,u}$, the most stressed cross-

section reaches or is relatively close to the plasticity domain at the first-order ultimate shear force. For larger imposed transverse displacement ($V > V_{dow\ I,u}$), the fibre measurement were lost, but one can assume that the local axial force increased again (see increase of the global axial force in Fig. 3.7d), so that the local internal forces had to follow the plasticity domain of Fig. 3.12 toward the limit $N = N_p$; $M = 0$.

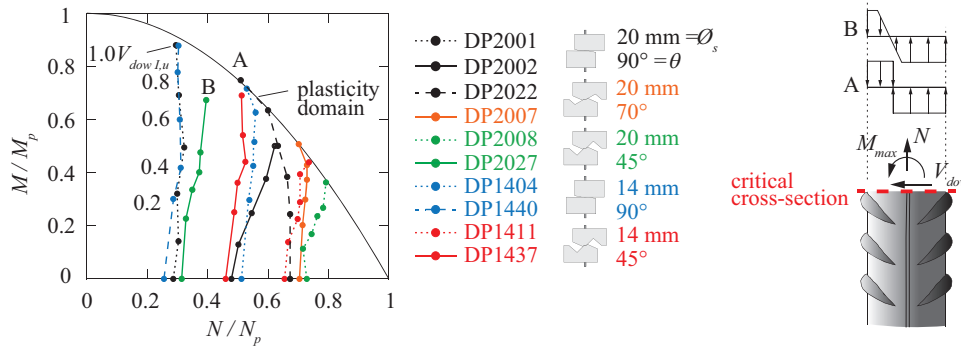


Figure 3.12: M-N interaction diagram of the critical cross-section.

Figure 3.13a shows the peak values of the contact pressure between the bar and the concrete (q_{max} / \varnothing_s) along the bar, calculated by double derivation of the bending moments from the optical fibre measurements as a function of the normalized transverse displacement for various load levels up to the first-order ultimate force $V_{dow\ I,u}$ ($0.9 V_{dow\ I,u}$ DP2007). Figure 3.13b displays their normalized values $q_{max} / (\varnothing_s \cdot f_{cm})$. It is important to note that the specimens with $\theta = 90^\circ$ have the largest peak values of the concrete pressure. The specimen with the slightly inclined crack ($\theta = 70^\circ$) shows almost the same peak pressure values along the bar, except at the ultimate load, for which the pressure is smaller. More inclined cracks ($\theta = 45^\circ$) exhibit reduced values of the normalized pressure, approximately half of those observed in specimens with $\theta = 90^\circ$.

Figure 3.13c shows the normalized stiffness, calculated as the secant slope of the pressure curves normalized with the ratio of the bar diameter to modulus of elasticity of the concrete \varnothing_s / E_c . The specimens with $\theta = 90^\circ$ have on average the largest normalized stiffness for initial load stages. However, this stiffness reduces as concrete begins to crack (due to splitting) and crush under the bar. The degradation of concrete becomes more pronounced at around $0.4 - 0.6 V_{dow\ I,u}$. Interestingly, the degradation rate of the normalized stiffness is similar for all considered specimens. Figure 3.13c shows that both bar diameters exhibit, on average, similar normalized stiffnesses.

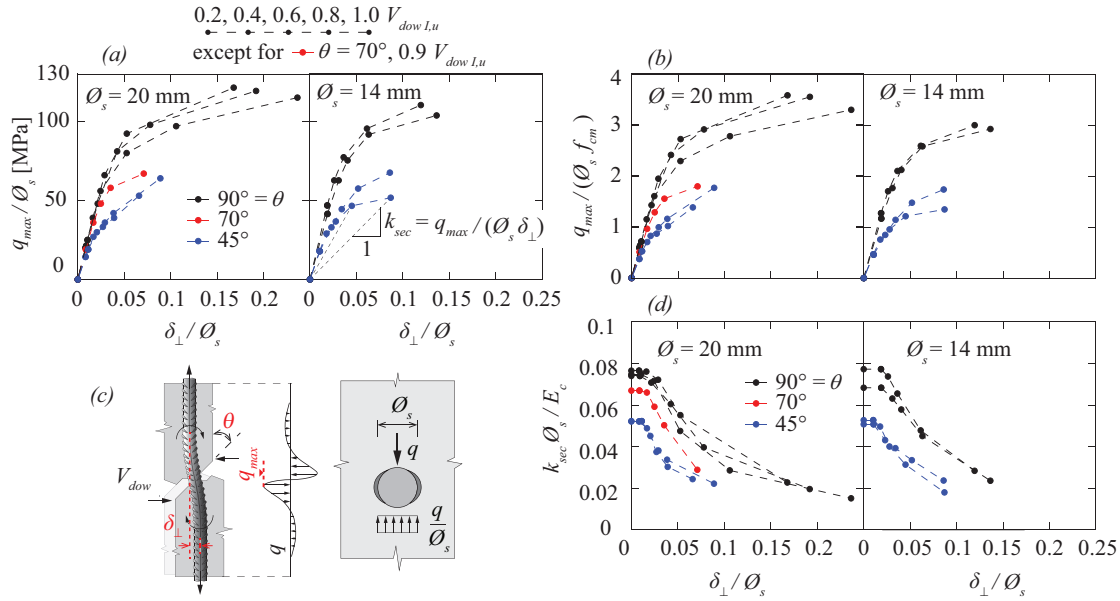


Figure 3.13: Local pressure and local stiffness of concrete derived from optical fibre measurements: (a) peak pressure; (b) pressure normalized with respect to the uniaxial concrete strength; (c) scheme with definitions; and (d) normalized secant stiffness of peak pressure curves.

3.3.2 Cyclic dowel tests

The cyclic dowel tests were conducted under force control. The majority of the tests were performed through three phases (Fig. 3.14a). In the first phase, the initial axial force N was imposed (mode I). After that, the initial shear force V_{dow} was applied (mode II). Eventually, the third phase included various combinations of the shear forces V_{dow} and axial forces N (with the minimum and maximum values $V_{dow, min/max}$ and $N_{min/max}$ within each cycle combination, Fig. 3.14a,b). In some cases, instead of the three phases, only mode II (V_{dow}) was imposed, without applying any initial axial force N (Fig. 3.14b). In this case, the bar was not attached to the test machine, ensuring no axial force was applied. The magnitudes of the forces were chosen to cause only elastic stresses in the reinforcement steel. After the application of initial forces, several groups of typically 5 to 10 cycles with a small stress amplitude were imposed to each test specimen.

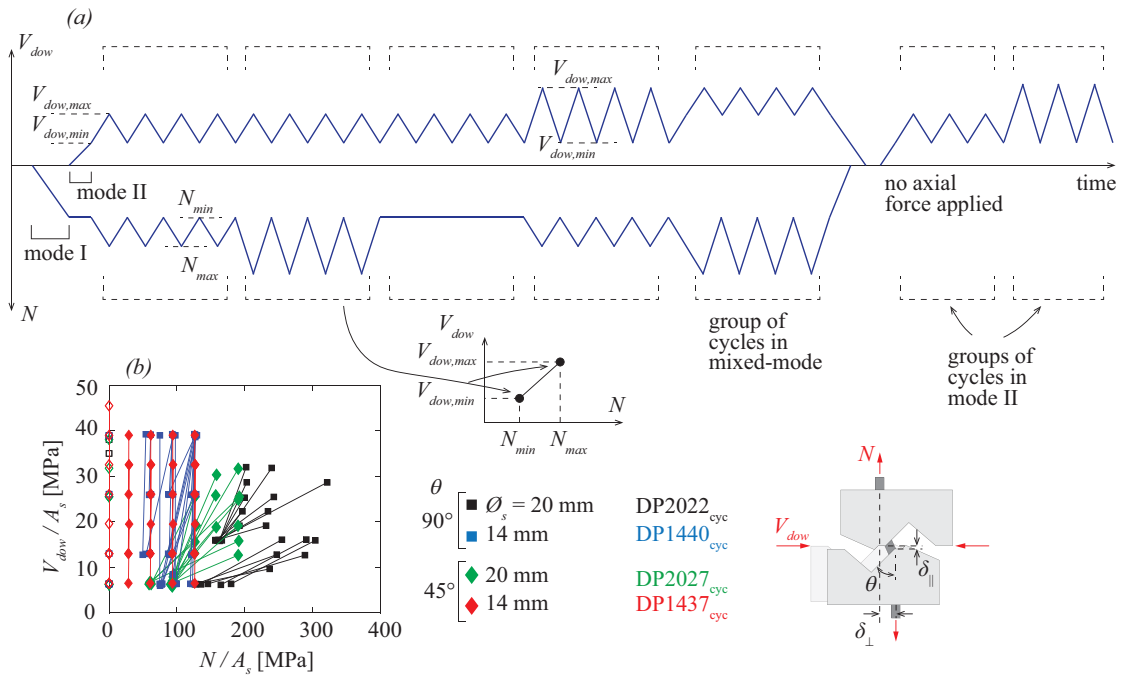


Figure 3.14: Cyclic tests: (a) protocol principle (rectangles indicate groups of typically 5-10 cycles with constant V_{dow} / N ratios) and (b) maximum and minimum values within performed V_{dow} / N cycle groups (each group of cycles as presented in (a) is shown in (b) by a segment connecting two points).

Figure 3.15 shows the optical fibre measurements of a cyclic test performed on the specimen DP2027_{cyc} due to the cycle combination with the minimum / maximum shear force $V_{dow, min/max} = 2 / 8$ kN and the axial force $N_{min/max} = 20 / 40$ kN (specimen with identical geometry and materials as DP2027 used for the monotonic test). For small stress amplitude cycles, the reinforcing bars typically remain elastic. The strains are composed of the average axial stress ($\sigma_{s, avg}$, Fig. 3.15c) and the nominal longitudinal bending stress at the edge of the bar cross-section ($\sigma_{s, flex}$ Fig. 3.15d). The critical cross-section (Fig. 3.15b) sustains average axial stresses of 63 / 135 MPa due to the minimum and maximum axial force $N_{min/max}$ within the cycle combination. The nominal axial stresses due to bending reach the values of 82 / 186 MPa due to the minimum and maximum shear force $V_{dow, min/max}$. Due to the same shear forces, the peak pressure on the concrete (Fig. 3.15f) along the bar is 9 / 24 MPa ($\sim 0.25 / 0.66 f_{cm}$). Again, the bar deformation derived from the optical fibre measurements (Fig. 3.15i) corresponds well to the DIC measurement on the concrete surface.

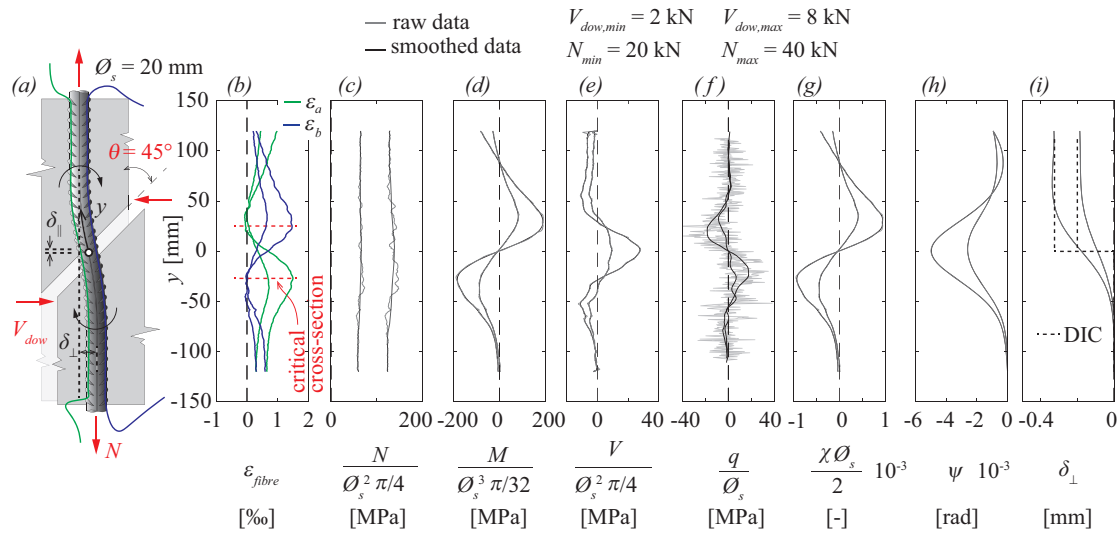


Figure 3.15: Optical fibre measurements: (a) main parameters and installed optical fibres; (b) measured strains and (c-i) derived results (specimen DP2027_{cycle}, see Fig. 3.11 for description).

The peak longitudinal stresses at the critical cross-section ($\sigma_{s,flex}$ due to bending and $\sigma_{s,avg}$ due to local axial force, Fig. 3.15) are shown as a function of the two components of the displacement (δ_{\parallel} and δ_{\perp}) in Fig. 3.16a. The figure identifies the three phases of the test protocol: pure tension (MI) in which the axial force N is imposed, pure shear (MII) in which the dowel force V_{dow} is imposed and a group of cycles in mixed-mode (MM).

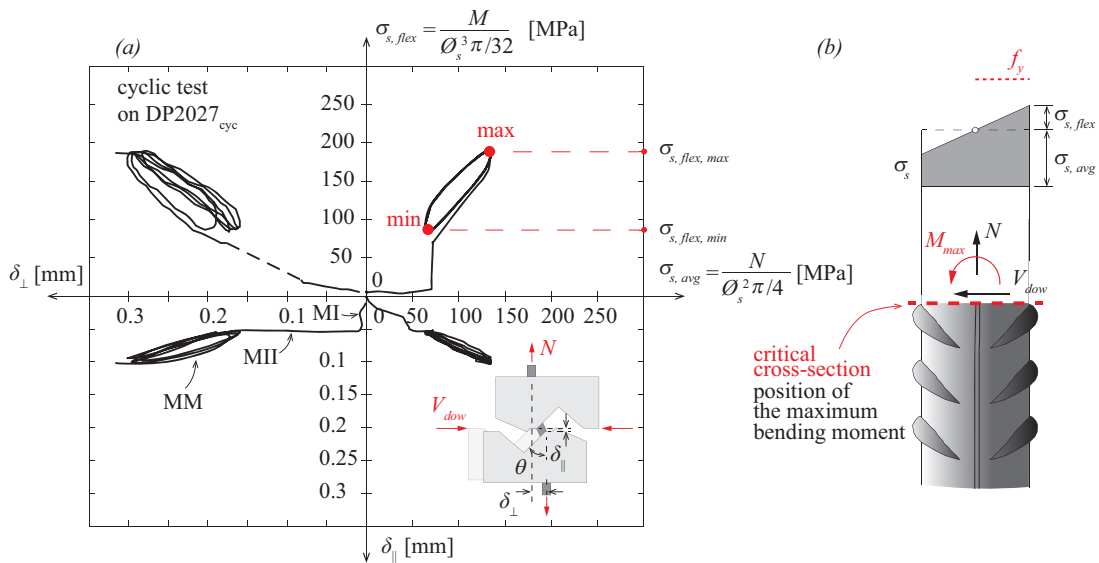


Figure 3.16: Cyclic test results for specimen DP2027_{cyc}: (a) relationship between stress and kinematic components in mode I, mode II and mixed-mode and (b) internal forces at the critical cross-section.

Figure 3.17 shows the optical fibre measurements at the critical cross-section for all cyclic tests. Only values corresponding to the minimum and maximum shear force $V_{dow, min/max}$ and the axial force $N_{min/max}$ within cycle groups are presented (see Fig. 3.14). Again, the measured longitudinal stresses are decomposed into the average stress $\sigma_{s, avg}$ and the bending stress $\sigma_{s, flex}$. Figure 3.17a-c show the nominal elastic stresses due to bending (associated to $V_{dow, min/max}$) and due to the axial force $N_{min/max}$ as a function of the normalized transverse displacement for all cyclic tests (tests in which both shear force V_{dow} and axial force N are applied are identified by solid markers and tests in mode II only, with $N = 0$, are identified by empty markers). Figure 3.17a shows that the longitudinal stress due to bending (associated to $V_{dow, min/max}$) increases approximately linearly with the transverse displacement. The stiffness of this response increases with the bar diameter and with the crack-bar angle. In addition, there appears to be a slightly larger measured transverse displacement associated with smaller average local axial stresses. Figure 3.17c shows that the reinforcing bars subjected to the pure shear (MII with no initial axial force) do not sustain any average axial stresses at the critical cross-section. However, these stresses increase for the somewhat larger shear force (this occurs because the bar elongates as it is anchored by the concrete embedment). Figure 3.17d shows the average elastic stresses due to the minimum and maximum axial force $N_{min/max}$ within each group of cycles at the critical cross-section as a function of the normalized longitudinal displacement δ_{\parallel} for two different bar diameters. These results encompass both pure tension tests (mode I, empty markers) and tests in which both shear force V_{dow} and axial force N are applied (full markers). The relationship between longitudinal stress due to axial force and longitudinal displacement is approximately linear.

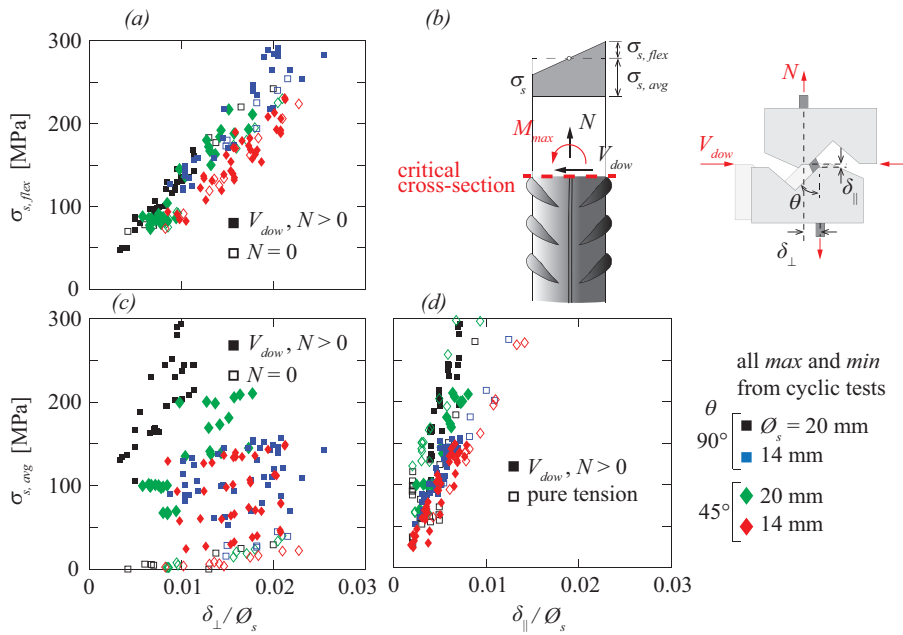


Figure 3.17: Calculated longitudinal stresses of all cyclic tests corresponding to the minimum and maximum shear force $V_{dow, min/max}$ and axial force $N_{min/max}$ within group of cycles at the critical cross-section based on optical fibre measurements: (a) axial stress due to bending as a function of the normalized transverse displacement, (b) definitions; average axial stress as a function of (c) the normalized transverse displacement; and (d) of the normalized longitudinal displacement component δ_{\parallel} .

3.3.3 CP test series

The CP test series examined the concrete stiffness and strength underneath a rebar subjected to a concentrated load perpendicular to the bar axis. The position of the force is denoted as distance a from the concrete edge (representing the crack surface in dowel tests, Fig. 3.18). In Fig. 3.18a, the relationship between the applied force F and the penetration δ of the bar at concrete edge is shown (colours indicating various distances a). Both the initial stiffness and the peak force increase with the distance a between the concrete edge and the point load, due to the larger concrete area carrying the applied force. However, the post-peak branches exhibit similar rates of decrease for all load positions.

For comparison, Fig. 3.18b shows the local shear force in the bar for three corresponding dowel tests (DP series, black curves, all of them with bar diameter $\varnothing_s = 20$ mm and $\theta = 90^\circ$, δ assumed to correspond to $\delta_{\perp}/2$). It can be observed that the CP tests can reproduce the behaviour of the comparable dowel tests for the load position $a = 0.9 \varnothing_s = 18$ mm (red curves). This match occurs because this force position approximately corresponds to the position of the resultant of the

pressure distribution along the bar in the dowel tests. It is interesting to note that in the CP tests, after reaching the peak load, a softening behaviour associated with the development of splitting cracks perpendicular to the concrete surface and spalling cracks associated with concrete crushing can be observed. A similar softening behaviour can also be observed in the considered dowel tests if the contribution of the catenary action is removed (Fig. 3.18b, brown curves). On the contrary, when the catenary action is accounted for, the dowel tests exhibit a hardening behaviour in the depicted range. This observation seems to indicate that the shear force contribution of the catenary action is transferred to concrete at larger distances from the crack surface. Moreover, the spalling patterns at the free surface are similar in the CP tests and the DP tests (see Appendices 3.A and 3.C).

DIC measurements on the lateral surface of the welded steel piece allowed to determine the displacement profiles of the bar which are shown in Fig. 3.18c at the peak load F_u for various load positions a . In most cases, the bars do not bend and only rotate because they are stiffened by the welded steel profile. However, bars subjected to a centric load (orange curves) exhibit slight bending underneath the point load due to the larger forces and lever arms involved.

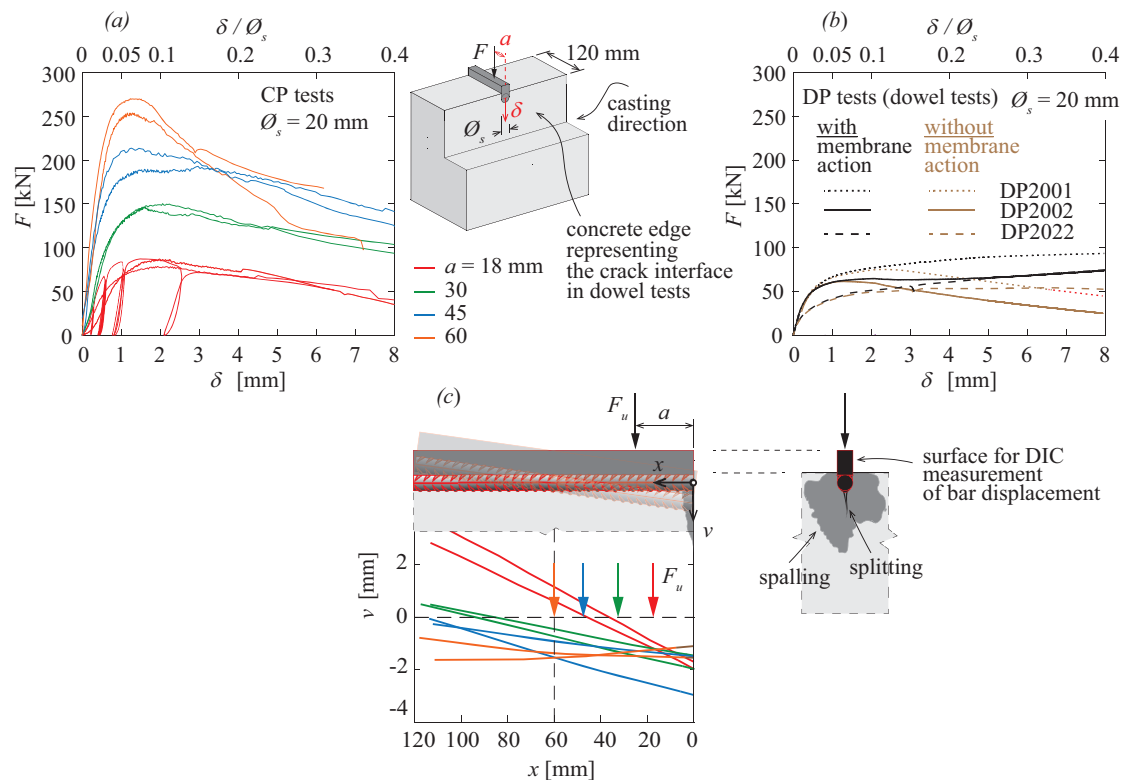


Figure 3.18: CP test results: force-penetration relationships for (a) CP tests; (b) DP tests and (c) deformed shape of the bar at peak load for different load positions (same colours as in (a)).

Figure 3.19a shows the relationship between the measured peak force F_u and the distance a . The peak force increases approximately linearly with its distance from the edge of the bar.

If the compressive stress in concrete under the bar is assumed to be uniformly distributed and symmetrical with respect to the point of application of the load, a nominal concrete plastic stress can be calculated: $\sigma_{c,pl} = F_u / (\varnothing_s \cdot 2a)$. Figure 3.19b shows the values of the plastic stress normalized by the uniaxial concrete strength as a function of the normalized force distance. All the values are close to four due to the confinement effect of the concrete embedment. It must be noted that the stress $\sigma_{c,pl}$ shown in Fig. 3.19b is affected by several assumptions which are a rough simplification of the reality. In addition, the load introduction device did not allow for sufficiently exact definition of the position of the force. These two effects can explain the larger normalized strengths for small distances a which is counterintuitive (for very small distances a , the biaxial stress state at the surface should become governing).

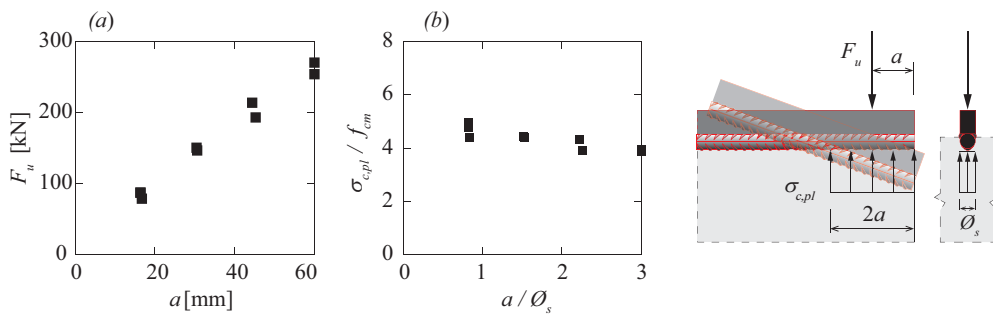


Figure 3.19: CP test results: (a) peak force as a function of the distance from the bar end to the load and (b) plastic concrete stress normalized by uniaxial concrete strength as a function of the load position.

The concrete near the edge crushes and gradually spalls due to the penetration of the bar. Figure 3.20 shows the values of concrete spalling (out-of-plane displacement, w) at discrete points along the vertical axis under the bar end. Significant spalling commonly occurs within a depth of two to three bar diameters (spalling failure patterns at peak load are given in Appendix 3.C). The depth of spalling is an indicator of the stiffness degradation, which starts at approximately half a peak force. The amplitude of the measured spalling displacement w (several mm at peak load) suggests that in the dowel tests of series DP, where the imposed longitudinal displacements were significantly smaller, spalling is partially prevented, which leads to a larger strength and/or a less brittle behaviour (this effect could also explain the different behaviour of the DP and CP tests shown in Fig. 3.18).

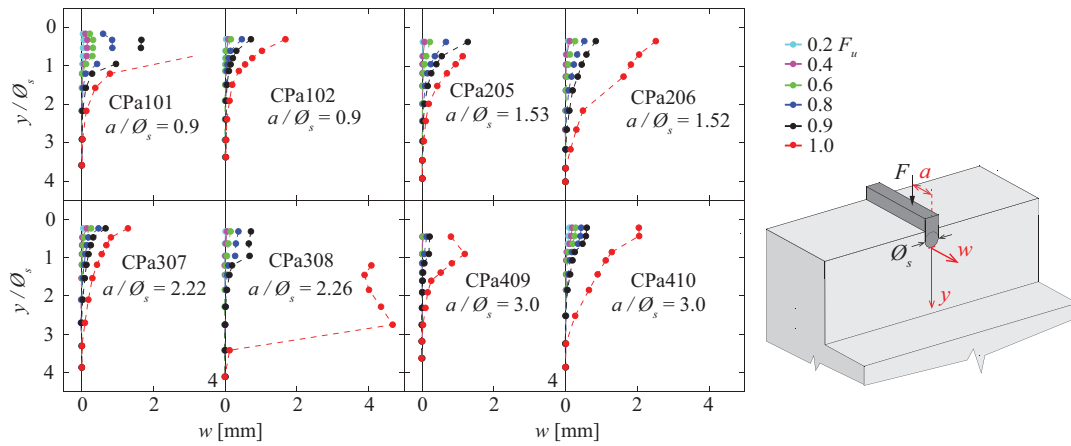


Figure 3.20: Out-of-plane displacement (spalling, w) of the concrete face under the bar for various specimens at various load stages measured by DIC.

3.4 Comparison with existing models

3.4.1 Concrete stiffness at the serviceability limit state

The existing formulae that predict the concrete stiffness under the bar were typically derived empirically. In this section, two analytical expressions are compared to the experimental results presented in this work. The first is the formula by Soroushian et al. [Sor87] which was fitted on numerous tests involving compressed concrete under the bar (similar to the series CP described above). The expression defines the stiffness k_c (contact pressure between bar and concrete divided by the transverse displacement δ) as a function of the bar diameter \varnothing_s and the uniaxial compressive concrete strength f_c :

$$k_c = \frac{127\sqrt{f_c}}{\varnothing_s^{\frac{2}{3}}} \quad (3.1)$$

where k_c is expressed in MPa/mm, f_c in MPa and \varnothing_s in mm (the exponent on the bar diameters relates to a size effect). This expression solely predicts the initial concrete stiffness under the bar.

The second considered expression by Brenna et al. [Bre90] is also empirical. It was fitted on multiple dowel tests using the beam-on-the-elastic-foundation model [Tim25, Fri38, Win67, Zim88]. This expression accounts for the degradation of the concrete stiffness with increasing transverse displacement, but has no size effect:

$$k_c = 400 \frac{f_c^{0.7}}{\varnothing_s} \left[\left(0.66 - \frac{f_c}{80.5} \right) + 0.487 \left(1 + \frac{f_c}{116} \right) \sqrt{1 + 0.023 \left(\frac{2 + f_c/116}{1 + f_c/116} \right)^2 \left(1 - \frac{f_c}{30.7} + 174 \frac{\delta_{\perp}}{\varnothing_s} \right)^2} \right]^{\frac{4}{3}} \quad (3.2)$$

In Fig. 3.21, a comparison is presented between the two predictions and the local concrete stiffness derived from the optical fibre measurements of test series DP. The stiffness derived from these measurements is calculated as the ratio between the peak pressure q_{max} / \varnothing_s and the transverse displacement $\delta_{\perp, q}$ at the point of maximum pressure. The stiffness results are normalized (dimensionless values) and presented as a function of the normalized transverse displacement. The predictions are shown by envelopes, accounting for the variability of governing test parameters. Soroushian's expression generally underestimates the concrete stiffness except for large transverse displacements, where the initial underestimation is compensated by the neglected concrete degradation. This discrepancy arises because Soroushian's expression was calibrated on tests involving relatively long bars laterally loaded against concrete, which is different from dowels that transmit stresses to concrete over a smaller area, resulting in a larger stiffness. The concrete stiffness predicted by Brenna et al. [Bre90] corresponds well with the results of the tests with $\theta = 90^\circ$, while it tends to overestimate the stiffness for $\theta = 45^\circ$. However, this prediction effectively captures the degradation rate of the concrete stiffness.

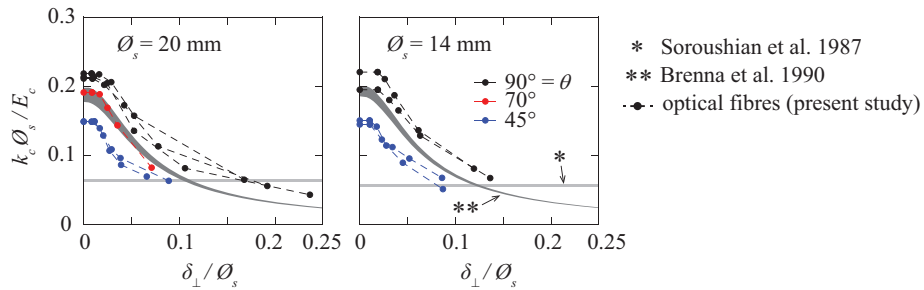


Figure 3.21: Comparison of the existing empirical expressions with the derived stiffness based on optical fibres measurements in dowel tests.

3.4.2 Ultimate resistance

The first-order dowel resistance $V_{dow l, u}$ can be predicted using the model proposed by Rasmussen [Ras62] which was derived on the basis of the limit analysis approach (plastic behaviour of the dowel bar, with a bending resistance $M_p = f_y \varnothing_s^3 / 6$, and a uniformly distributed contact pressure between concrete and bar. The expression for the case where the point of contraflexure in the bar is at the concrete edge (crack) is given by:

$$V_{dow\ I,u} = \varnothing_s^2 \sqrt{\frac{\eta_3 f_c f_y}{3}} \quad (3.3)$$

where η_3 is a coefficient accounting for the concrete strength increase due to the triaxial stress state in concrete under the dowel (calibration parameter according to the Rasmussen's approach) and f_y is the yield strength of the bar. Figure 3.22 shows the comparison between the model's predictions and a database of 121 dowel tests with $\theta = 90^\circ$. For tests where the point of contraflexure in the bar does not correspond to the concrete edge, Equation 3.3 is adapted according to the original model by Rasmussen [Ras62]. Three values of the coefficient η_3 are used for this comparison. The first value (Fig. 3.22a), $\eta_3 = 5.1$ as proposed by Rasmussen based on his tests, provides slightly unconservative results (average value of the measured-to-predicted resistance ratio of 0.91) and a relatively large scatter (CoV = 19.9%). In Fig. 3.22b, the comparison is conducted assuming $\eta_3 = 3.0$ (in accordance with Tanaka et al. [Tan11]). In this case, the coefficient of variation is reduced to 16.8% and the average value of the measured-to-predicted resistance ratio is 1.14. Assuming $\eta_3 = 4.0$ as observed in the CP test series of this work (see Fig. 3.19b), the statistical values become CoV = 18.1% and avg = 1.00 (see Fig. 3.22c for comparison). It must be noted that this model was originally developed for bars perpendicular to cracks (or concrete edges, $\theta = 90^\circ$) and without applied axial force.

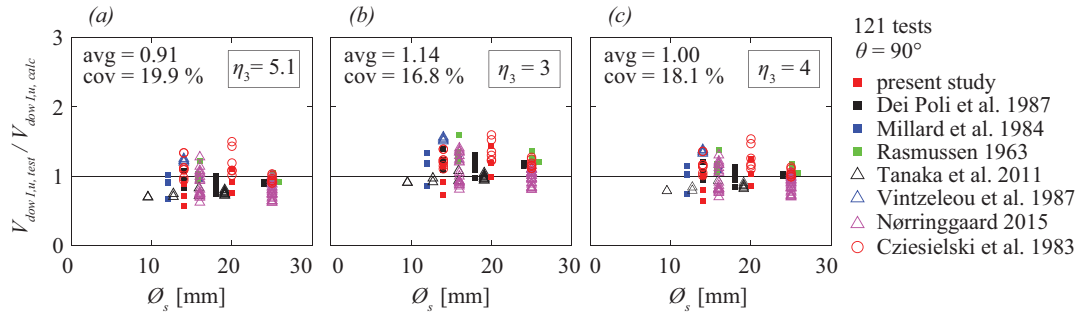


Figure 3.22: Comparison of Rasmussen's model with the considered database of dowel tests with $\theta = 90^\circ$.

For other crack angles ($\theta < 90^\circ$), the first-order dowel resistance $V_{dow\ I,u}$ can be predicted using the expression proposed by Dulacska [Dul72]:

$$V_{dow\ I,u} = \varnothing_s^2 k_N k_{cal} f_y \eta_3 \cos \theta \left(\sqrt{1 + \frac{f_{c,cube}}{3 k_N k_{cal}^2 f_y \eta_3 \cos^2 \theta}} - 1 \right) \quad (3.4)$$

where $k_N = 1 - (N / N_p)^2$ is a parameter which accounts for the axial force in the bar (with N being the axial force and N_p being the axial resistance), $k_{cal} = 0.05$ is a calibration coefficient proposed by Dulacska based on their tests, $\eta_3 = 4$ and $f_{c,cube}$ is the concrete strength measured on 150 mm cubes. Figure 3.23 shows the comparison between the predictions and 21 dowel tests with $\theta < 90^\circ$. The expression provides fairly good results, with an underestimation of resistances for tests with relatively large axial forces in the bar (few tests from the present study). The average

value of the measured-to-predicted resistance ratio is 1.09 and the coefficient of variation is 21.3%.

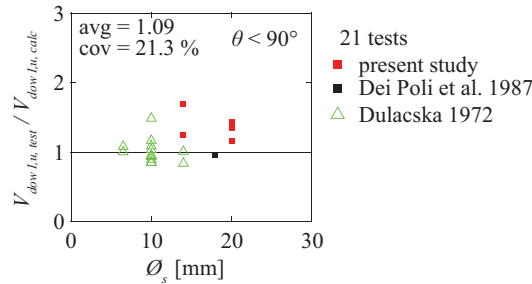


Figure 3.23: Comparison of Dulacska’s model [Dul72] with the considered dowel tests with $\theta < 90^\circ$.

The plastic dowel response including the activation of the catenary action can be predicted by the model proposed by Sørensen et al. [Sor17] which is also based on the limit analysis approach. Figure 3.24a shows a comparison of this model with the experimental responses of the present study. The model’s prediction is accompanied by an envelope accounting for the various test variables. Its lower and upper boundaries account for the prediction considering the bar’s yield and tensile strength, respectively. Figure 3.24b shows the main parameters of the model. For the concrete confinement coefficient, $\eta_3 = 4.0$ is assumed. The model’s prediction shows a relatively good agreement with the final catenary load stages. It is important to note that also this model was developed for the bars perpendicular to cracks or concrete faces.

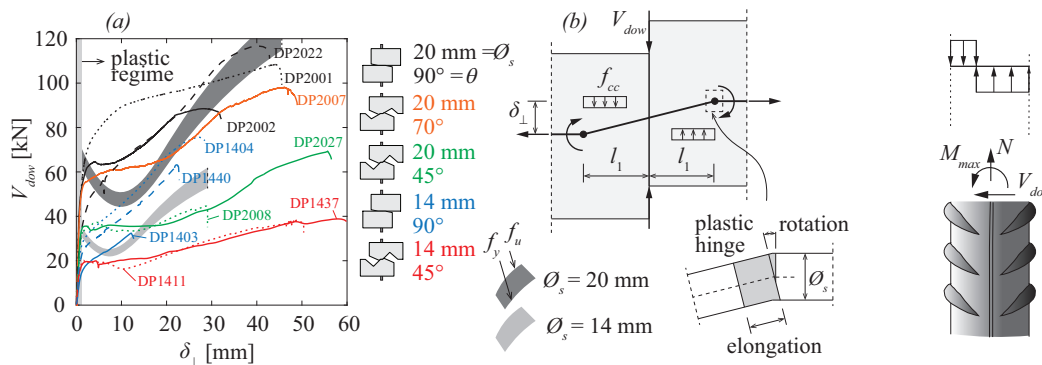


Figure 3.24: (a) Comparison of the model proposed by Sørensen et al. [Sor17] with the performed dowel tests and (b) model’s hypotheses.

3.5 Conclusions

This chapter presents an experimental investigation of the dowel action in steel reinforcing bars using refined measurements: digital image correlation and distributed optical fibres. Dowel action (DP test series) was studied for various angles between the crack and the bar, bar diameters and imposed crack kinematics with monotonic or cyclic loadings. The chapter also investigates the behaviour of concrete under a rebar (CP test series). Several models are evaluated against these tests. The majority of the findings observed in this study align closely with or provide further support for the conclusions from previous research. The main conclusions are:

1. The observed dowel response is significantly influenced by the angle between the bar and the crack, the bar diameter and the applied crack kinematics. A bar nearly perpendicular to the crack and a larger bar diameter correspond to a stiffer dowel response and a larger first-order ultimate load. The imposed crack kinematics determine both the linear and non-linear regime of the dowel response.
2. Large shear forces in the bar associated to large imposed transverse displacements result in concrete crushing under the bar near the crack. Yielding of the bar is caused by the combination of bending and axial force in the bar.
3. The dowel resistance under large transverse displacements consists of two components: the first-order ultimate dowel force associated with a shear force in the bar and the second-order catenary force associated with the axial force and the rotation of the bar in the crack region.
4. According to optical fibre measurements, the section of the bar with maximum longitudinal stresses (combined local axial force and bending) is located approximately at 1.5 times the bar diameter \varnothing_s from the crack.
5. The angle between crack and reinforcement has a significant influence on the behaviour.
6. A substantial degradation of the concrete stiffness under the bar occurs at approximately 40% to 60% of the first-order ultimate load (shear resistance before activating the catenary action). The degradation rate remains approximately constant across all specimen configurations with respect to the normalized transverse displacement.
7. The dowel response remains comparable under monotonic and low-stress amplitude cyclic loading within the studied service-load domain. Furthermore, several low-stress cycles do not reduce significantly the stiffness.
8. The existing models considered provide reasonably accurate predictions of the concrete stiffness under the bar, the first-order dowel resistance and the dowel plastic response. Yet, there remains room for improvement, particularly regarding the influence of the angle between the crack and the bar as well as the influence of the axial force.

Appendix 3.A: Failure pattern of DP test series

The monotonic dowel tests which experienced the rupture of the reinforcing bar allowed observing the concrete spalling patterns. They are shown in Fig. 3.25 in a crack plan view in terms of normalized coordinates.

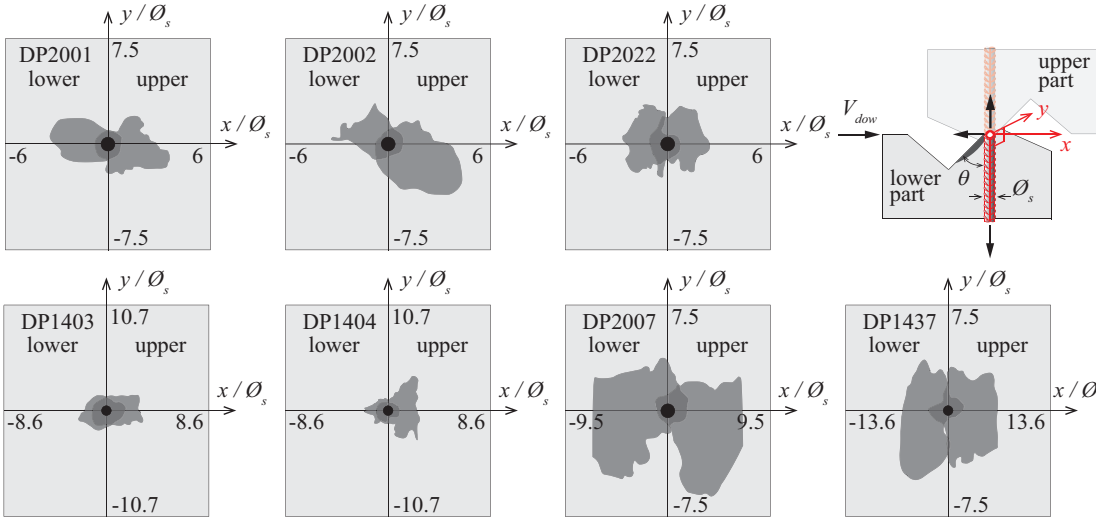
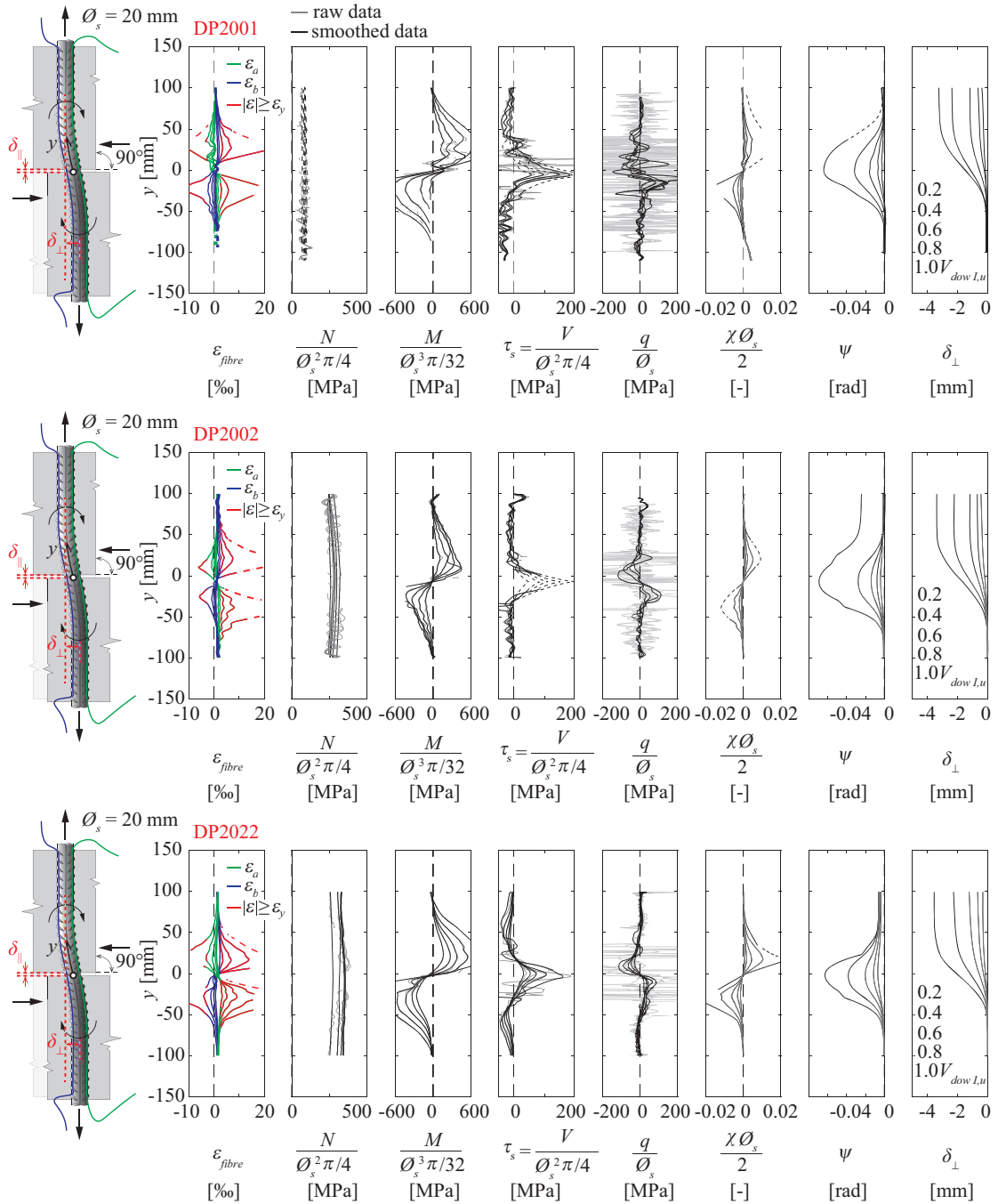
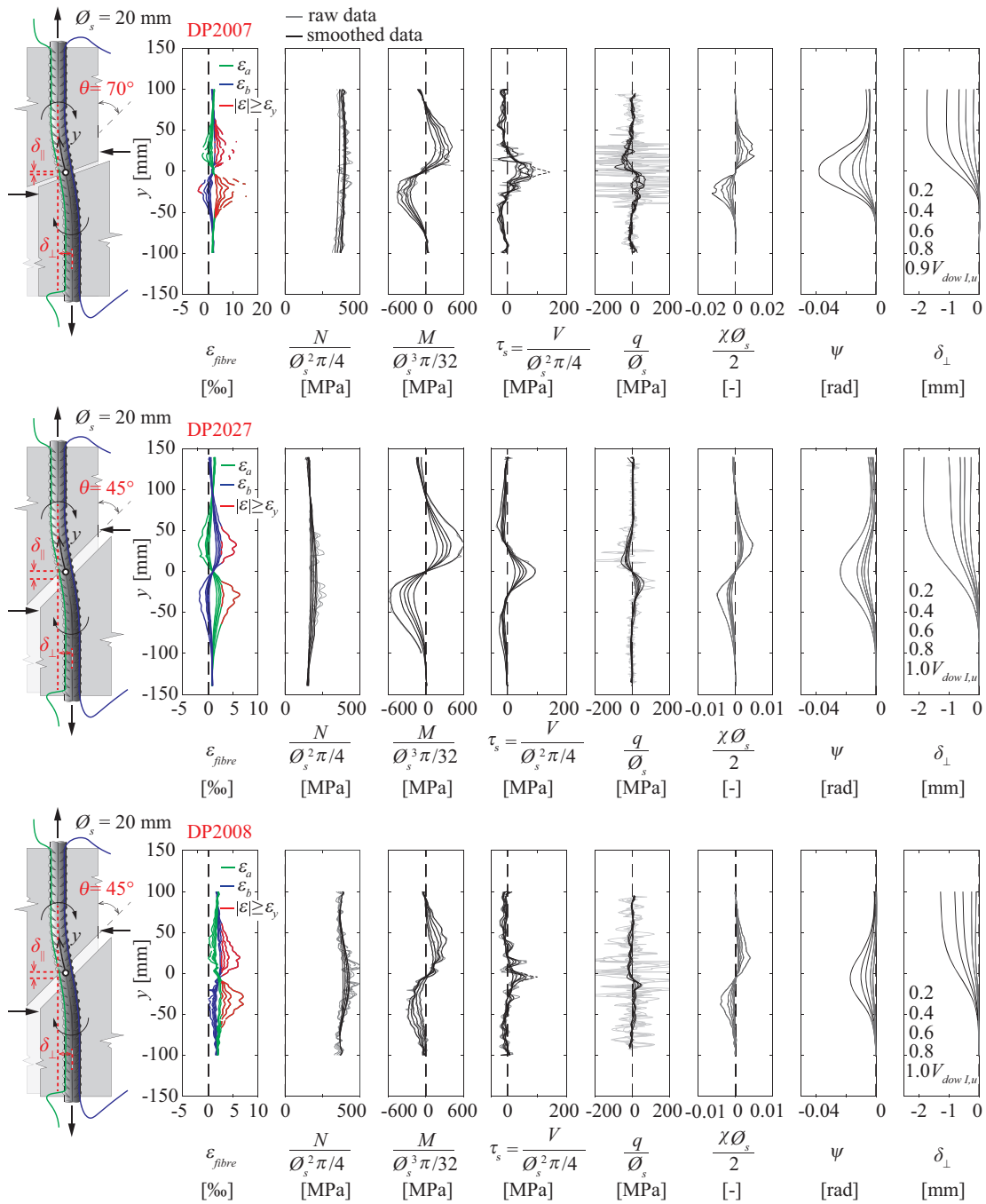


Figure 3.25: Concrete spalling patterns of monotonic dowel tests after catenary rupture.

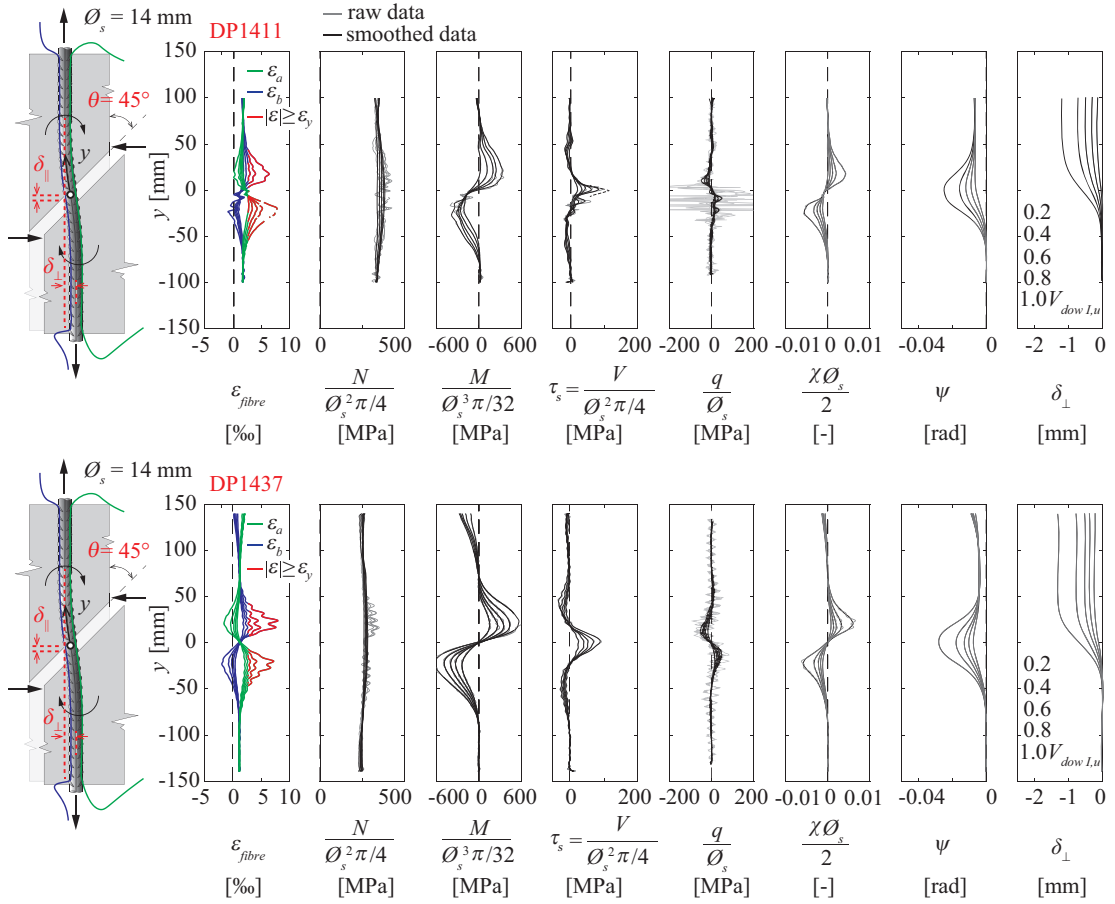
Appendix 3.B: Optical fibre measurements of DP series



Experimental investigation of dowel action in reinforcing bars using refined measurements



Appendix 3.B: Optical fibre measurements of DP series



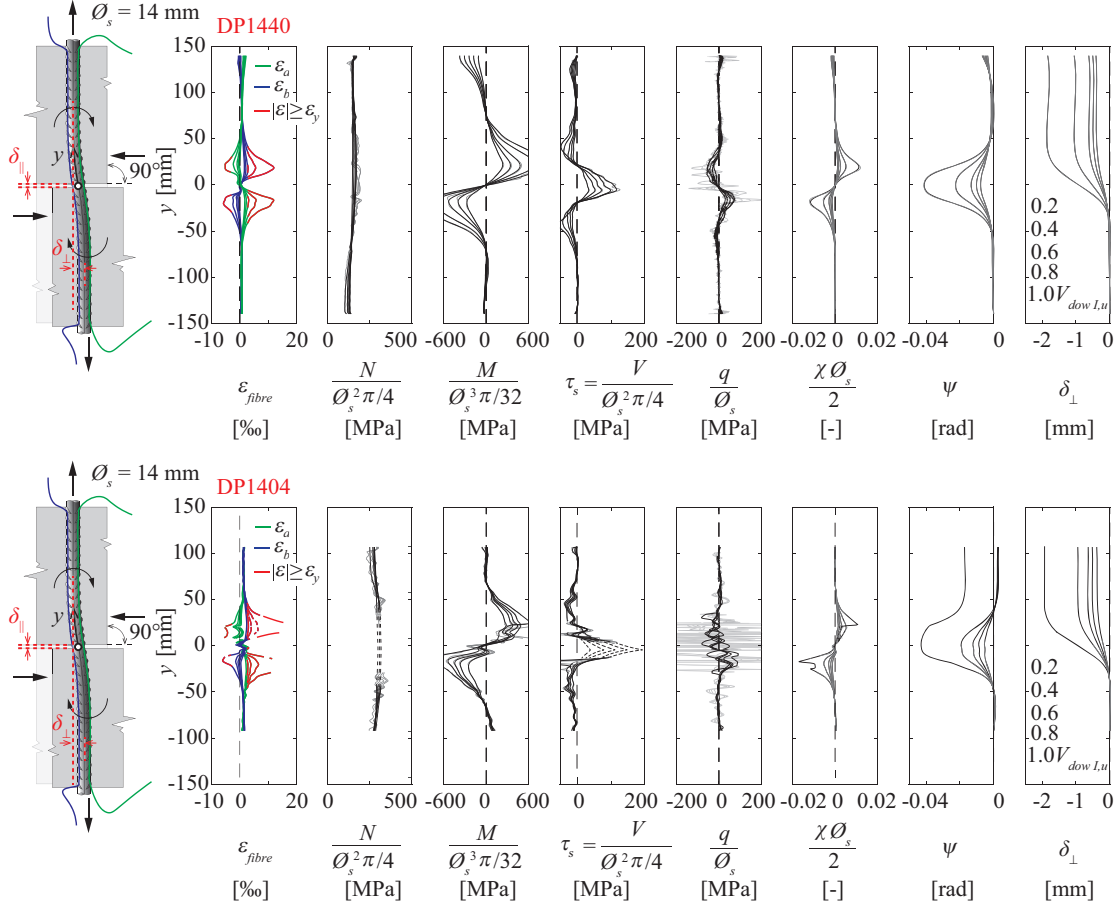


Figure 3.26: Optical fibre measurements and derived parameters in monotonic dowel tests.

Appendix 3.C: Spalling pattern at peak load in CP tests

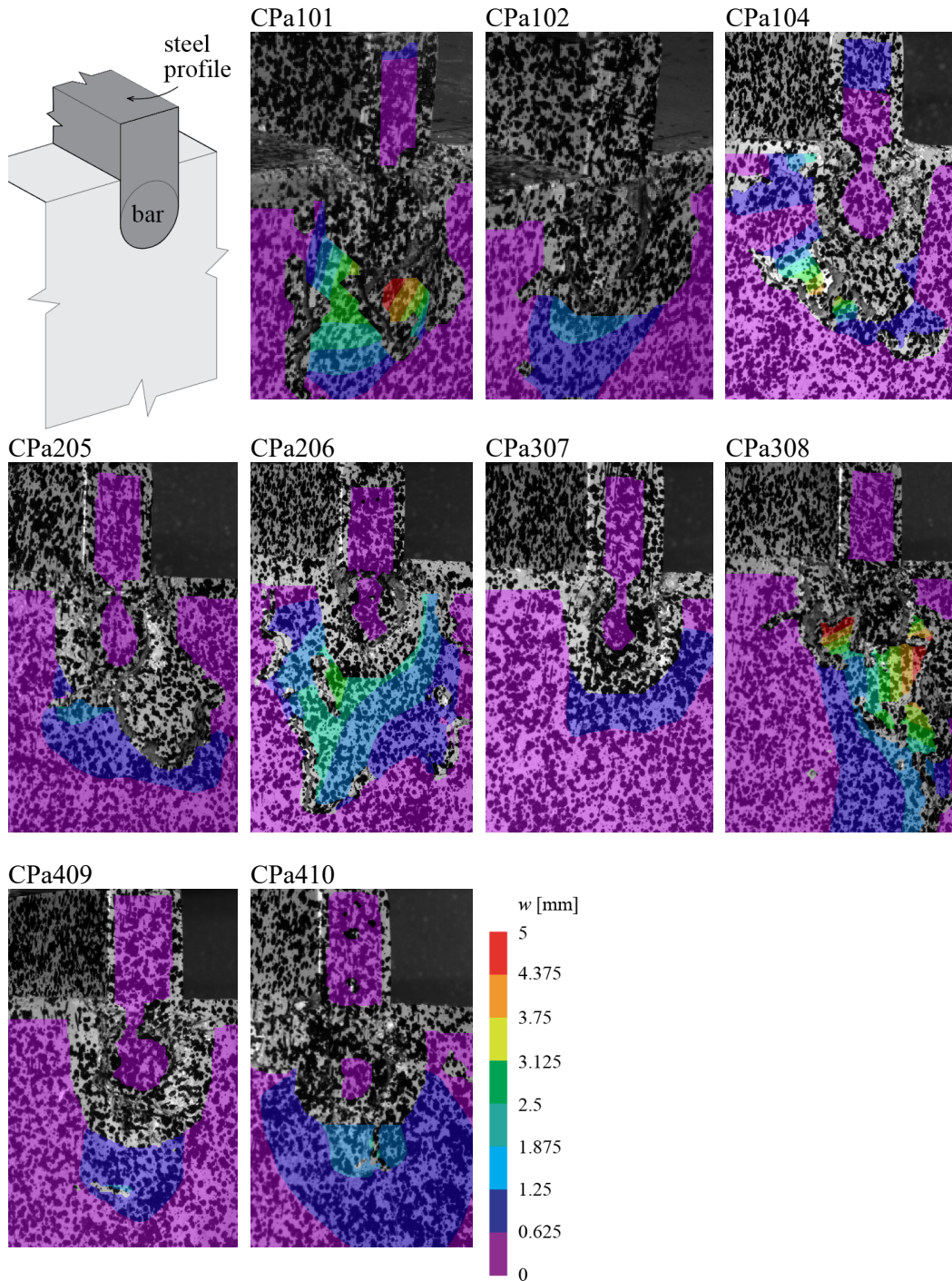


Figure 3.27: Spalling pattern at peak load in CP tests: front face of specimens where the penetration of the bar is reported with respect to the applied force in Fig. 3.18a.

Nomenclature

Latin characters: lower case

a	distance of the concentrated load from the bar end
$f_{c,cube}$	uniaxial concrete strength measured on cubes
f_{cm}	mean uniaxial compressive concrete strength on day of testing
f_u	tensile strength of the rebar
f_y	yield strength of the rebar
k_c	concrete stiffness under a rebar
k_{cat}	constant in accordance with Dulacska's model
k_N	= $1 - (N / N_p)^2$ in Dulacska's model
k_{sec}	secant slope of pressure curves
q / \varnothing_s	contact pressure between concrete and the rebar
q_{max} / \varnothing_s	peak contact pressure between concrete and the rebar
w	out-of-plane displacement (spalling)
x_{max}	position of the critical cross-section in the rebar

Latin characters: upper case

A_s	area of the bar cross-section
E_c	elastic modulus of concrete
E_s	elastic modulus of the rebar
F	point load in CP tests
F_u	peak force in CP tests
M	bending moment in the rebar
M_{max}	maximum bending moment in the rebar
M_p	plastic bending moment of the rebar
N	global axial force
N'	inclined local axial force in rebar
N_{init}	initial global axial force
$N_{min / max}$	minimum / maximum axial force within a cyclic combination
N_p	axial resistance of the rebar
V	shear force in the rebar
V_{dow}	dowel force
$V_{dow I}$	first-order dowel force
$V_{dow I,u}$	ultimate first-order dowel force
$V_{dow, min / max}$	minimum / maximum shear force within a cyclic combination
$V_{dow,cat}$	catenary action

Greek characters: lower case

α	angle defining the applied crack kinematics in monotonic dowel tests
δ	penetration of the bar end in concrete
$\delta_{ }$	crack opening component in the direction of the rebar
$\delta_{ , init}$	initial crack opening component in the direction of the rebar
$\delta_{ min / max}$	minimum / maximum crack opening component in the direction of the rebar
δ_{\perp}	transverse displacement
$\delta_{\perp,q}$	transverse displacement corresponding to the position of the peak pressure
$\delta_{\perp min / max}$	minimum / maximum transverse displacement
$\varepsilon_{fibre / a / b}$	strains measured by optical fibres on both sides of the rebar
ε_s	strain in the rebar
$\varepsilon_{s,avg}$	average longitudinal strain in the rebar
$\varepsilon_{s,flex}$	longitudinal strain in the the rebar due to bending
ε_y	yield strain in the rebar
η_3	concrete confinement factor
θ	angle between the crack and the rebar
$\sigma_{c,pl}$	plastic stress in concrete
σ_s	stress in the rebar
$\sigma_{s,avg}$	average axial stress in the rebar
$\sigma_{s,flex}$	nominal longitudinal stress due to bending at the edge of the bar cross-section
χ	curvature of the rebar
ψ	rotation of the rebar

Others

CP	tests of the concrete behaviour under a rebar
DIC	Digital Image Correlation
DP	dowel tests
MI	Mode I
MII	Mode II
MM	Mixed-Mode
\varnothing_s	diameter of the dowel bar

Experimental investigation of dowel action in reinforcing bars using refined measurements

Chapter 4

Steel stresses and shear forces in reinforcing bars due to dowel action

This chapter represents the following publication:

Pejatović M., Muttoni A., *Steel stresses and shear forces in reinforcing bars due to dowel action*, 2024. [publication in preparation]

The authors of this publication are Marko Pejatović (PhD candidate) and Prof. Aurelio Muttoni (thesis director, École Polytechnique Fédérale de Lausanne, Switzerland).

This work was conducted by the first author (Marko Pejatović) under the supervision of Prof. Aurelio Muttoni who consistently offered the constructive feedback, proofreading and manuscript revisions.

The main contributions of Marko Pejatović to this publication and chapter are the following:

- Collection and analysis of various experimental data to establish the concrete bearing stiffness formulation to be introduced in Winkler's model.
- Elaboration of the proposed formulation for the concrete bearing stiffness.
- Collection of the data of dowel test results and the validation of the model with the proposed formulation of the concrete bearing stiffness.
- Elaboration of the figures and tables included in the chapter.
- Manuscript preparation of the chapter.

Abstract

Reinforcing bars in structural concrete are typically designed to carry longitudinal axial forces. Nevertheless, due to their bending stiffness, they can also carry transverse forces. This transverse force is often referred to as dowel action which induces stress concentrations in the reinforcing bars due to bending related to the relative displacements of two lips of a crack (or two concrete parts cast at different times) transverse to bar axis. Such a displacement component can occur due to the sliding of a crack perpendicular to the bar and/or to the opening and sliding of a crack inclined with respect to the bar. Due to the relatively large deformation capacity of steel, the bending stresses in the reinforcing bars due to dowel action are not detrimental at the ultimate limit state. However, for the fatigue verification, it is crucial to accurately estimate these stresses as a function of the imposed transverse displacements or of the imposed shear force. The traditional Winkler's model (beam on elastic foundation) can be used to describe the dowel behaviour. In this model, the bearing stiffness of concrete under the bar is typically formulated to account for only few parameters such as the bar diameter and the concrete strength. However, the actual behaviour is much more complex and, therefore, this model can be improved by accounting for other effects present in actual structures. To that purpose, this chapter introduces a new formulation for the bearing stiffness to be used in Winkler's model, which is calibrated based on mechanical considerations and measurements with optical fibres. Besides the bar diameter and the concrete strength, the proposed formulation accounts for the following effects: angle between the crack and the bar, casting conditions, thickness of the concrete cover, number of load cycles and the softening effect of local secondary cracks in concrete near the ribs due to the axial force. A comparison between the model's prediction with the proposed bearing stiffness and considered monotonic and cyclic dowel tests shows a good agreement, both in terms of the shear force-transverse displacement response and of the peak longitudinal stress in the reinforcing bar.

Keywords: dowel action, cracks, shear, fatigue of reinforcing bars, concrete bearing stiffness, stress variation, existing structures

4.1 Introduction

Reinforcing bars in structural concrete, which are usually designed for longitudinal axial forces, can also carry transverse shear forces due to their bending stiffness. In some cases, this transverse force (also known as dowel action) is beneficial and can be accounted for in the dimensioning at the ultimate limit state (e.g., to carry shear forces along interfaces between two concrete parts cast at different times or in refined mechanical models for shear and punching, where a portion of the shear force can be carried by the longitudinal reinforcement). On the other side, the dowel action, which develops due to an imposed deformation, can be detrimental in case of fatigue due

to the associated additional longitudinal bending stresses in the reinforcing bars. These stresses develop in case of transverse relative displacements due to the sliding of a crack perpendicular to the bar or to the opening and sliding of a crack inclined with respect to the bar (e.g., for an inclined shear crack which crosses the longitudinal and shear reinforcement, see Fig. 4.1a). In general, the transverse component of the displacement between the two lips of the crack can be calculated from the opening and the sliding of the crack and the angle between the bar and crack (see component δ_{\perp} in Fig. 4.1b).

The fatigue verification to account for this phenomenon can be based on an estimate of the crack kinematics and a model of the dowel action which allows estimating the stress variations as a function of the imposed deformations, accounting for the interaction between the reinforcing bar and the surrounding concrete. For the assessment of existing structures, a possibility could consist in measuring directly the strain variations on the reinforcement surface due to variable actions using strain gauges or fibre [Can20, Mon22, Cor23, Bad21]. Nevertheless, if the strain gauges are not installed before casting, this would require a removal of the concrete cover which would significantly affect the local behaviour near the crack, compromising the results. An interesting alternative consists in measuring the crack kinematics on the concrete surface using image recognition [Rez20, Dor18] and correlation techniques [Can21, Can20, Geh22]. In this case also, a model which allows calculating the stress variations on the basis of the measured crack kinematics is required.

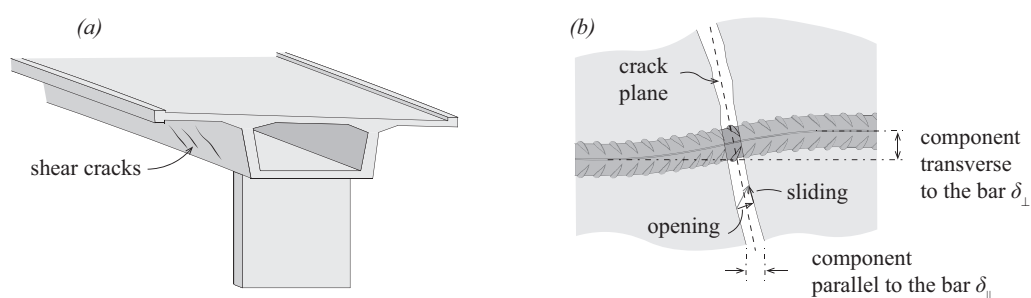


Figure 4.1: (a) Schematic representation of shear cracks in an existing reinforced concrete structure and (b) components of the crack kinematics.

The dowel force, and thus also the steel stresses, can be limited by spalling of the concrete cover, primarily occurring when the concrete cover (net distance between concrete surface and bar) is thin compared to the bar diameter [Vin86]. Alternatively, in cases with sufficient cover, the dowel force can be limited by localized concrete crushing near the interface combined with yielding of the bar in bending (development of a plastic hinge in the bar). Focusing on the latter case with sufficient cover, failure is characterized by a relatively ductile behaviour due to the potentially significant steel plastic strains. Consequently, many authors have evaluated the dowelling resistance of a steel bar by using the limit analysis approach (see Rasmussen [Ras62] and [Sor86, Dul72, Dei87, Dei92, Tan11, Pru88, Nør15, Vin87]). This approach assumes that the plastic hinge develops in the bar at a certain distance from the crack which crosses the bar.

In the limit analysis approach, the contact pressure between the bar and concrete activated by dowel action is typically assumed to be constant. This pressure can reach a value significantly larger than the uniaxial concrete strength due to the local tri-axial stress state. The ratio between the confined concrete strength and the uniaxial concrete strength (measured on cylinders) is often referred to as a confinement factor. Its values were typically determined from dowel tests with interfaces perpendicular to the bar, with a range between approximately 3 and 5 [Tan11, FIB08, Ras62]. For angles between the bar and the crack smaller than 90° , the dowel resistance was observed to decrease [Dul72]. The resistance was also observed to decrease in presence of an axial force in the reinforcing bars [Sor86, FIB13].

The behaviour of dowels under cyclic loads has also been experimentally investigated in the past [Ele74, Sta77, Jim79]. These experiments commonly indicated an increased shear displacement with cycles (in case of imposed shear forces), a considerable stiffness degradation, and a reduction in hysteresis loop areas over cycles. Vintzeleou et al. [Vin87] conducted an extensive parametric experimental investigation of dowels under cyclic loads, emphasizing the influence of the concrete cover. They observed an increased stiffness degradation in cases involving fully reversed deformations. Using these findings, they proposed a model addressing the failure due to steel yielding and concrete crushing [Vin86]. Soltani et al. [Sol08] developed a path-dependent mechanical model for deformed reinforcing bars at the concrete interface under the coupled cyclic shear and axial force. This model considered the bond-slip strain relationship, the three-dimensional yield criterion, and the cyclic stiffness deterioration. Tests by Kato et al. [Kat73] showed no substantial response degradation in the reinforcing steel due to cyclic loads. Consequently, the degradation in the dowel response is primarily associated with the degradation of concrete. Li et al. [Li18] conducted dowel tests to investigate the response deterioration due to fatigue and to identify fatigue failure modes. Their study highlighted that the accumulated fatigue damage significantly reduced the dowel resistance measured under monotonic loads. Based on these findings, they proposed a nonlinear bond model for numerical applications, accounting for the effect of the fatigue damage.

Regarding service loads, the model developed by Winkler [Win67] and Zimmermann [Zim88] already in the 19th century with the elastic analysis solution of slender beams resting on a cohesionless foundation can be adapted to describe the interaction between the reinforcing bar and the surrounding concrete for moderate dowel forces. In this case, the concrete can be modelled as linear springs smeared along the bar. The mathematical solution for a bar with an infinite length was reported by Timoshenko et al. [Tim25], subsequently applied by Friberg [Fri38] for the case of dowel bars between concrete pavement segments. The uncertainty in the prediction relies on estimating the concrete stiffness under the bar, which remains a challenge due to the complexity of the problem related to the development of local cracking. Many authors have attempted to estimate this stiffness through empirical expressions, typically accounting for the bar diameter and the concrete strength [FIB08, Sor87]. These expressions were usually calibrated to fit the load-displacement curves using the shear force or the transversal displacement as indicators of the concrete degradation [Bre90, Dei92, Sol08],

particularly for larger loads. However, the stiffness is significantly influenced by other factors such as casting conditions due to the plastic settlement and bleeding of the fresh concrete [Moc20], thickness of the concrete cover [Mon21], angle between the crack and the bar, number of cyclic loadings, and secondary cracks induced by the axial force [Got71].

This chapter introduces a new formulation for the concrete bearing stiffness under the reinforcing bar to be used in Winkler's model (beam on elastic foundation) to estimate the bending stresses in the reinforcing bar and the activated dowel shear force as a function of the imposed transverse displacement δ_{\perp} (see Fig. 4.1b). The formulation accounts for the aforementioned phenomena and is calibrated based on mechanical considerations and measurements with optical fibres described in another publication by the authors [Pej22]. In addition, the case of unsymmetric behaviour on both sides of the crack, which can be typically observed due to bleeding and settlement of fresh concrete as well as the presence of a free concrete surface near the bar, is also investigated analytically.

4.2 Steel stresses and shear force in the bar according to Winkler's model

4.2.1 Analytic solution for the symmetric case

As described above, Winkler's model [Tim25, Fri38] can be used to investigate in the elastic domain a reinforcing bar embedded in concrete which is subjected to an imposed transverse displacement at its end which corresponds to half the crack slip δ_{\perp} (Fig. 4.2a, or transverse component of the crack opening in case of cracks not perpendicular to the bar).

For this purpose, one can assume that (1) at interface between reinforcing bar and concrete, no tensile forces can be carried and that (2) on the compression side, the contact pressure between the bar and the concrete can be smeared over the bar diameter \varnothing_s (Fig. 4.2c), so that the average value of the pressure can be calculated from the distributed bearing force q (in N/mm) between the bar and the concrete: q/\varnothing_s (in MPa).

According to Winkler's assumption, the pressure q/\varnothing_s is proportional to the local relative transverse displacement $\tilde{\delta}_{\perp}$: $q/\varnothing_s = k_c \tilde{\delta}_{\perp}$, where k_c is the bearing stiffness (in MPa/mm) which will be treated in the following. The differential equation of Winkler's model for our case without external action on the bar thus becomes:

$$E_s I_s \frac{d^4 \tilde{\delta}_{\perp}}{dx^4} + k_c \varnothing_s \tilde{\delta}_{\perp} = 0 \quad (4.1)$$

Steel stresses and shear forces in reinforcing bars due to dowel action

where x is the bar's axis, E_s is the elastic modulus of the reinforcing bar and $I_s = \pi\varnothing_s^4/64$ is the moment of inertia of the rebar. The solution of Eq. 4.1 in terms of the local relative transverse displacement $\tilde{\delta}_\perp$ is:

$$\tilde{\delta}_\perp = e^{\beta x} (C_1 \cos\beta x + C_2 \sin\beta x) + e^{-\beta x} (C_3 \cos\beta x + C_4 \sin\beta x) \quad (4.2)$$

where

$$\beta = \left(\frac{k_c \varnothing_s}{4E_s I_s} \right)^{1/4} = \frac{2}{\varnothing_s} \left(\frac{k_c \varnothing_s}{\pi E_s} \right)^{1/4} \quad (4.3)$$

in mm^{-1} is a parameter which expresses the relative stiffness between the bar and the surrounding concrete, and C_1 to C_4 are constants which can be found based on given boundary conditions. For $x > 0$, since the effect of the imposed crack displacement at $x = 0$ must decrease with increasing x , coefficients C_1 and C_2 must be zero. The constant C_4 can be calculated using the condition of the zero-bending moment at the crack location ($x = 0$):

$$M(x=0) = -E_s I_s \tilde{\delta}_\perp'' = -2\beta^2 E_s I_s e^{-\beta x} (C_3 \sin\beta x - C_4 \cos\beta x) = 0 \rightarrow C_4 = 0 \quad (4.4)$$

and the constant C_3 can be calculated from the displacement condition for $x = 0$:

$$\tilde{\delta}_\perp(x=0) = \frac{\delta_\perp}{2} = C_3 \quad (4.5)$$

The shear force along the bar is thus:

$$V = -E_s I_s \tilde{\delta}_\perp''' = \beta^3 E_s I_s \delta_\perp e^{-\beta x} (\sin\beta x - \cos\beta x) \quad (4.6)$$

which allows calculating the dowel force V_{dow} for $x = 0$:

$$V_{dow} = \beta^3 E_s I_s \delta_\perp \quad (4.7)$$

The position of the maximum bending moment along the bar (Fig. 4.2d) can be calculated from the condition $V(x_{max}) = 0$. The solution of $\tan(\beta x_{max}) = 0$ gives:

$$x_{max} = \frac{\pi}{4\beta} = \frac{\pi}{8} \varnothing_s \left(\frac{\pi E_s}{k_c \varnothing_s} \right)^{1/4} \approx 0.52 \varnothing_s \left(\frac{E_s}{k_c \varnothing_s} \right)^{1/4} \quad (4.8)$$

After replacing the position of the peak moment into:

$$M(x) = -E_s I_s \tilde{\delta}_\perp'' = -\beta^2 E_s I_s \delta_\perp e^{-\beta x} \sin\beta x \quad (4.9)$$

the maximum bending moment can be calculated as:

$$M_{max} = \frac{\beta^2 E_s I_s \delta_\perp}{\sqrt{2}} e^{-\pi/4} = \frac{V_{dow}}{\sqrt{2}\beta} e^{-\pi/4} \quad (4.10)$$

so that the maximum stress in the bar (Fig. 4.2e) becomes:

$$\sigma_{s,flex} = \frac{32M_{max}}{\varnothing_s^3 \pi} \approx 0.37 \sqrt{k_c E_c E_s} \frac{\delta_{\perp}}{\varnothing_s} \quad (4.11)$$

where $\bar{k}_c = k_c \varnothing_s / E_c$, with E_c being the elastic modulus of concrete.

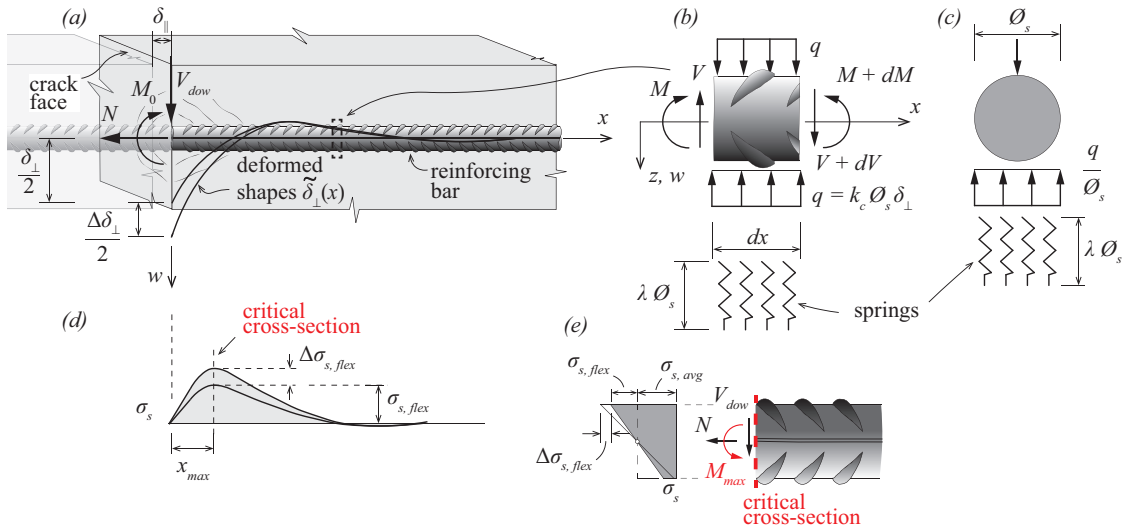


Figure 4.2: (a) Reinforcing bar subjected to the crack kinematic components δ_{\perp} and δ_{\parallel} ; (b) forces on a portion of the bar in the longitudinal section and (c) cross-section; (d) longitudinal stress $\sigma_{s,flex}$ and its variation $\Delta \sigma_{s,flex}$ due to bending along the bar's axis and (e) stress $\sigma_{s,flex}$ and its variation $\Delta \sigma_{s,flex}$ at the critical cross-section.

Equations 4.7 and 4.11 show that the bearing stiffness k_c is a crucial parameter for the accuracy of the model's prediction. Several empirical formulations for k_c have been proposed in the past (see subchapter 4.2.2), typically accounting for the bar diameter and the concrete strength. In the following, a new expression for the bearing stiffness k_c is proposed, based on mechanical considerations and measurements with optical fibres (chapter 4.3).

4.2.2 Existing models for the bearing stiffness of concrete

The existing formulae that predict the concrete bearing stiffness under the bar were typically derived empirically. In this subchapter, two analytical expressions are compared to the experimental results presented in [Pej22]. The first is the formula by Soroushian et al. [Sor87] which was fitted on numerous tests involving compressed concrete under a bar. The expression defines the bearing stiffness k_c as a function of the bar diameter \varnothing_s and the uniaxial compressive concrete strength f_c :

$$k_c = \frac{127\sqrt{f_c}}{\varnothing_s^{\frac{2}{3}}} \quad (4.12)$$

where k_c is expressed in MPa/mm, f_c in MPa and \varnothing_s in mm (the exponent 2/3 on the bar diameters relates to a size effect). This expression solely predicts the initial concrete stiffness under the bar.

The second considered expression by Brenna et al. [Bre90] is also empirical. It was fitted on dowel tests on the basis of the Winkler's model. This expression accounts for the degradation of the concrete stiffness with increasing transverse displacement, but has no size effect:

$$k_c = 400 \frac{f_c^{0.7}}{\varnothing_s} \left[\left(0.66 - \frac{f_c}{80.5} \right) + 0.487 \left(1 + \frac{f_c}{116} \right) \sqrt{1 + 0.023 \left(\frac{2 + f_c/116}{1 + f_c/116} \right)^2 \left(1 - \frac{f_c}{30.7} + 174 \frac{\delta_{\perp}}{\varnothing_s} \right)^2} \right]^{\frac{4}{3}} \quad (4.13)$$

In Fig. 4.3, a comparison is presented between the two predictions and the bearing stiffness derived from the optical fibre measurements of a test series presented in [Pej22]. These results (a representative test is shown in Fig. 4.4a-d) allow to calculate the local values of the bearing stiffness k_c by dividing the measured concrete pressure q/\varnothing_s (Fig. 4.4b) by the corresponding transverse displacement of the bar (Fig. 4.4c). In Fig. 4.4d, the distribution of the calculated values of \bar{k}_c (bearing stiffness k_c normalised by the ratio \varnothing_s/E_c) is presented along the bar. It can be observed that the derived local bearing stiffness increases farther from the crack interface, reaching a plateau approximately half a diameter away from the crack. The average stiffness values taken from the plateau are presented for several tests in Fig. 4.3 as a function of the transverse displacement δ_{\perp} . One can observe that for small transverse displacements δ_{\perp} , the normalised value of k_c is almost constant. In Fig. 4.3, the predictions are shown by envelopes, accounting for the variability of governing test parameters. Soroushian's expression generally underestimates the concrete stiffness except for large transverse displacements, where the initial underestimation is compensated by the neglected concrete degradation. The concrete stiffness predicted by Brenna et al. [Bre90] corresponds well with the results of the tests with $\theta = 90^\circ$, while it tends to be overestimated for $\theta = 45^\circ$. However, this prediction effectively captures the degradation rate of the concrete stiffness. This means that current expressions can be improved accounting for parameters and effects which have not been considered in the empirical evaluation.

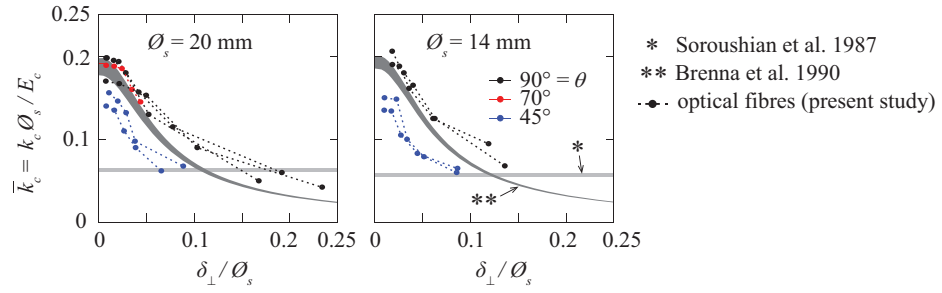


Figure 4.3: Comparison of the existing empirical expressions with the derived stiffness based on optical fibres measurements in dowel tests [Pej22].

4.3 Improved expression for the bearing stiffness

4.3.1 General formulation, influence of angle θ and of imposed displacement

The bearing stiffness, which is defined in Winkler's model as the ratio between pressure and local displacement ($k_c = q/(\varnothing_s \cdot \tilde{\delta}_{\perp})$) as described above), can be calculated assuming as a first approximation from the case of a strip load applied to a concrete half-space according to Boussinesq [Bou78]. For a strip with the width \varnothing_s (Fig. 4.2c), the bearing stiffness is related to the concrete elastic modulus and the bar diameter:

$$k_c = \frac{E_c}{\lambda \varnothing_s} \quad (4.14)$$

where the product $\lambda \varnothing_s$ can also be seen as the length of an idealized spring (see Fig. 4.2b and c). It can also be noted that Eq. 4.14 is similar to the normalised stiffness \bar{k}_c described above, where λ is the reciprocal of \bar{k}_c .

Since the case of the reinforcing bar submitted to dowel action is significantly different from the strip load according to Boussinesq (half-space limited vertically by the crack, circular shape of the bar), the factor λ can be calibrated on the basis of the bearing stiffness calculated from optical fibre measurements.

The angle θ between the crack and the reinforcing bar can be accounted for by applying to the bearing stiffness according to Eq. 4.14 a coefficient η_{θ} defined in Eq. 4.15:

$$\eta_{\theta} = \left(\frac{\theta}{90^\circ} \right)^{3/5} \quad (4.15)$$

As shown in Fig. 4.4e, the normalised bearing stiffness is suitably corrected with the coefficient η_θ defined in Eq. 4.15. For all cases, the normalised value of k_c for small transverse displacements δ_\perp is approximately 0.2, which means $\lambda = 5$ can be assumed. Interestingly, as shown in Figure 4.5, similar results can be obtained from the compression tests (series CP from [Pej24]).

Fig. 4.4e also shows that the bearing stiffness k_c starts to gradually decrease when the transverse displacement δ_\perp reaches a critical value due to the development of splitting cracks, local concrete crushing and spalling near the crack. This reduction can be accounted for by applying a reduction factor η_δ fitted based on the available data as a function of the transverse displacement δ_\perp according to Eq. 4.16:

$$\eta_\delta = \frac{1.5}{1 + 25 \frac{\delta_\perp}{\varnothing_s}} \leq 1.0 \quad (4.16)$$

The transverse displacement δ_\perp for which the stiffness starts to decrease is therefore

$$\delta_\perp = \frac{1.5 - 1}{25} \varnothing_s = 0.02 \varnothing_s .$$

Figure 4.4e shows the comparison with the tests results accounting for both coefficients η_θ and η_δ showing fine agreement.

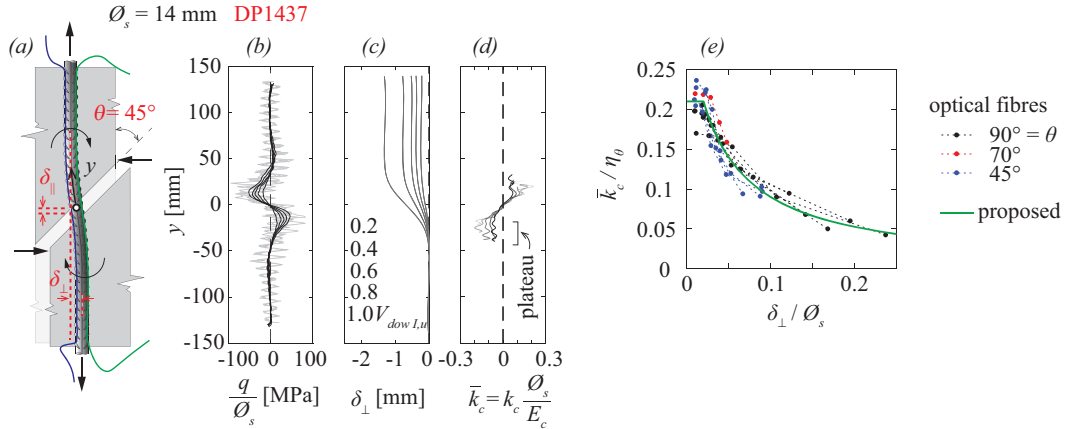


Figure 4.4: Calibration of the concrete stiffness under the reinforcing bar based on optical fibre measurements: (a) representative specimen with main parameters; (b) pressure between concrete and the bar; (c) transverse displacement of the bar; (d) normalised concrete stiffness and (e) comparison between the measured and the calculated bearing stiffness accounting for coefficients η_θ and η_δ (data from [Pej22]).

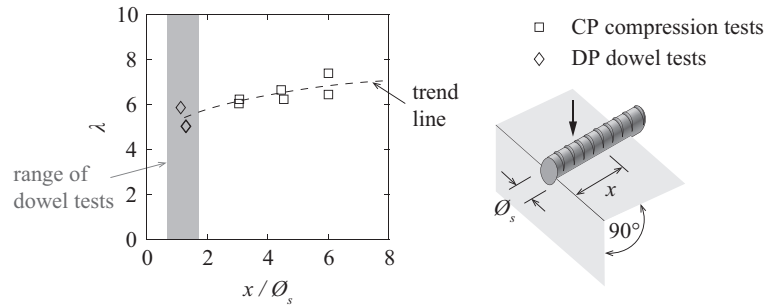


Figure 4.5: Coefficient λ as a function of the x / \varnothing_s ratio for the dowel (DP series from [Pej22]) and compression tests (CP series from [Pej24]).

To account for other effects, Eq. 4.14 is adapted by introducing additional coefficients as shown in Eq. 4.17:

$$k_c = 0.2 \frac{E_c}{\varnothing_s} \eta_\theta \cdot \eta_\delta \cdot \eta_c \cdot \eta_{cast} \cdot \eta_{fc} \cdot \eta_{bond} \cdot \eta_{cyc} \quad (4.17)$$

where η_c accounts for the presence of a free surface near to the bar; η_{cast} for presence of pores and cracks due to the bleeding and settlement of fresh concrete (Monney et al. [Mon21], Moccia et al. ([Moc20])); η_{fc} for the concrete strength; η_{bond} for the presence of local cracks induced by bond activated by a longitudinal component of the crack opening and η_{cyc} for cyclic

loading. Each of these factors is calibrated based on various test results (the details are presented in following subchapters).

4.3.2 Influence of the casting conditions, concrete cover, and direction of the dowel force

It is well known from other researchers (see for instance Moccia et al. [Moc20]) that fresh concrete behaves just after casting in a manner similar to a saturated soil with resulting settlements and bleeding (migration of mixing water toward the top part of the concrete element). These phenomena can cause settlement cracks near the top reinforcement bars as well as voids (due to settlement) and pores (once the bleeding water is evaporated) under the top bars as shown in Fig. 4.6a. These cracks, voids and pores typically have a detrimental effect on the bond behaviour of reinforcing bars located in the top parts of concrete elements (also known as top-bar effect, or poor casting conditions, see for instance Moccia et al. [Moc21]) which is accounted for in most codes of practice when calculating the anchorage and laps lengths. With respect to the dowel action, this effect has not been investigated yet, but some results of tests carried out to investigate the bond and other problems can be used to estimate the bearing stiffness in the Winkler's formulation. Figure 4.6b shows the 8 cases which need to be distinguished and the covers c_x and c_y which can have an influence on the behaviour. Since in actual structures, different cases occur on either side of a crack (namely A with D, B with C, E with H and F with G), the bearing stiffness on either side of the crack can be different. This effect is treated in subchapter 4.3.6 and Appendix 4.A.

For the cases A, B, E and F, the results of the tests conducted by Monney et al. ([Mon21], Fig. 4.7) can be used to calibrate the coefficients η_c and η_{cast} . In these tests, a reinforcing bar was pressed into concrete prisms in a similar manner to the tests of series CP [Pej24]. The cover c_x (Fig. 4.7c) was varied from $c_x / \varnothing_s = 0$ to 3 and two bar diameters were used ($\varnothing_s = 14$ mm and 20 mm). In a series, the reinforcing bar was supported on the top of the lateral formworks during casting (poor casting conditions). In a second series, the reinforcing bar was placed on the bottom formwork during casting and tested upside-down (good casting conditions). Figure 4.7a shows the uniform pressure under the bar ($\sigma_{c,avg}$, averaged across the bar width and length) normalised by the uniaxial concrete strength f_c as a function of the bar penetration in the concrete δ normalised by the bar diameter \varnothing_s . The blue and red curves correspond to good and poor casting conditions, respectively, while different shades represent various cover-to-bar diameter ratios c_x / \varnothing_s . As expected, the stiffness is smaller for poor casting conditions than for good conditions.

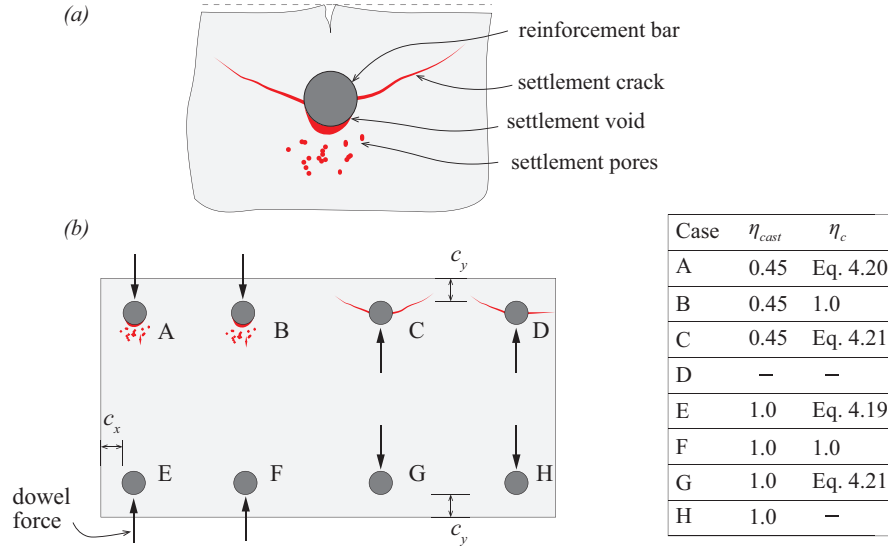


Figure 4.6: (a) Consequences of settlement and bleeding of fresh concrete around top bars (adapted from Moccia et al. [Moc20]); and (b) investigated cases and proposed coefficients η_c (influence of cover) and η_{cast} (influence of casting condition).

Figure 4.7b shows the initial slope of the stress-bar penetration curves as a function of the cover-to-diameter ratio c_x / \varnothing_s . The results, which can be associated to the bearing stiffness k_c , are normalised by the values for good casting conditions and large cover c_x , so that they can be associated to the product $\eta_c \cdot \eta_{cast}$. The results show that the normalised stiffness increases with the c_x / \varnothing_s ratio, gradually reaching its maximum value for approximately $c_x / \varnothing_s = 3$. One can observe a similar increasing trend for both casting conditions and bar diameters, but the reduction for thin covers is larger for poor bond conditions than for good ones. Based on these results, empirical expressions for coefficients η_c (influence of cover) and η_{cast} (influence of casting condition) are proposed (Fig. 4.7b, dashed curves):

$$\eta_{cast} = 1.0 \quad \text{for good and} \quad \eta_{cast} = 0.45 \quad \text{for poor casting conditions} \quad (4.18)$$

$$\eta_c = 1 - \frac{0.2}{1 + (c_x / \varnothing_s)^2} \quad \text{for good casting conditions} \quad (4.19)$$

$$\eta_c = 1 - \frac{0.45}{1 + (c_x / \varnothing_s)^2} \quad \text{for poor casting conditions} \quad (4.20)$$

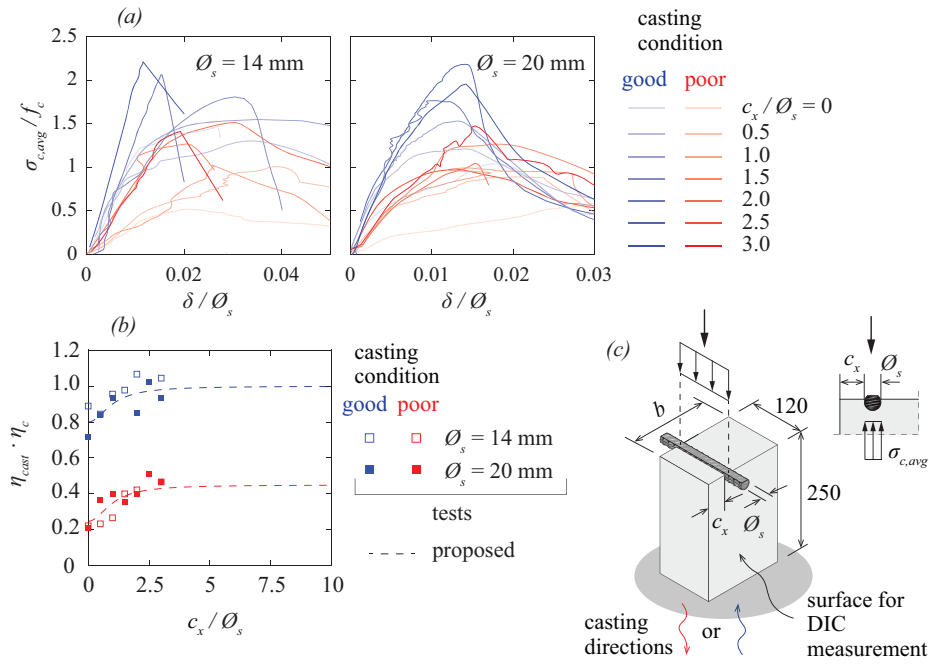


Figure 4.7: (a) Normalised average stress under a bar as a function of the bar penetration-to-diameter ratio; (b) coefficients η_c (influence of cover) and η_{cast} (influence of casting condition) for cases A, B, E and F in Figure 4.6b; and (c) specimen (adapted from [Mon21]).

The tests conducted by Moccia et al. ([Moc21], Fig. 4.8) can be used to investigate the influence of the casting conditions and the cover for the cases C and G shown in Figure 4.6b (dowel force pushing perpendicularly against a free surface). The cases of corner bars D and H are not considered due to the lack of experimental evidence. In the tests by Moccia et al., a pressure was applied in cylindrical openings (diameter 20 mm) located at various distances c_y from the free surface (ratios c_y / \varnothing_s ranging from 0.25 to 2.5). Casting with the opening on top of the formwork was associated with poor conditions, while casting with the opening at the bottom corresponded to good conditions.

Figures 4.8a,b show the internal pressure p in the opening as a function of the displacement δ measured on the free concrete surface for both poor and good casting conditions. The shades correspond to various c_y / \varnothing_s ratios. The initial slope of the curves (bearing stiffness k_c) shown in Fig. 4.8c is normalised by the value for good casting conditions and relatively large cover, so that it represents the product $\eta_c \cdot \eta_{cast}$. Based on these results, the same coefficient η_{cast} as for the other cases can be used (namely 1.0 and 0.45 for good and poor casting conditions, respectively), whereas for coefficient η_c , the following empirical expression can be proposed (Fig 4.8c, dashed curves):

$$\eta_c = \frac{1}{1 + (c_y / \varnothing_s)^{-2}} \quad (4.21)$$

It has to be noted that Eq. 4.21 describes only the influence of the cover on the initial stiffness. The development of spalling cracks (subparallel to the free surface, also called delamination cracks) is not considered with this expression and should be accounted for in case of imposed transverse displacements sufficiently large to trigger the development of this type of cracks. Here again, there is a need for further research to cover this case which can be governing in practice.

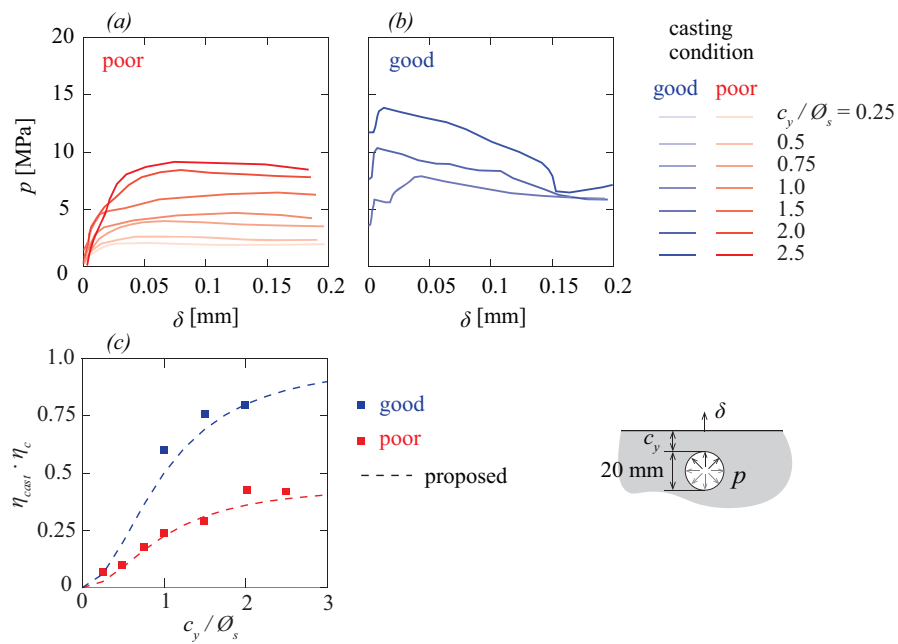


Figure 4.8: (a) Internal pressure as a function of the cover-to-diameter ratio c_y / \varnothing_s from tests conducted by Moccia et al. [Moc21] for poor and (b) good casting conditions; and (c) coefficients η_c (influence of cover) and η_{cast} (influence of casting condition) for cases C and G in Figure 4.6b.

4.3.3 Influence of the concrete strength

The influence of the concrete strength should be theoretically accounted for by its elastic modulus which, if not measured on specific tests, can be derived from the concrete strength using the relationships defined in codes of practice. In this work, the comparisons are conducted with an average value of:

$$E_c = 10'000 f_c^{1/3} \quad (4.22)$$

Nevertheless, the expressions proposed by Soroushian et al. [Sor87] and Brenna et al. [Bre90] described in subchapter 4.2.2 which were fitted on their tests give larger values of the bearing stiffness for higher strength concrete (see comparison in Figure 4.9). This is also confirmed by the results of tests by Monney et al. [Mon21] described above (two series with concrete strengths of about 34 and 76 MPa). In Figure 4.9, the bearing stiffness by Monney et al. corrected with the coefficients η_c and η_{cast} defined above are compared to the analytical solutions by Soroushian et al. [Sor87] and Brenna et al. [Bre90]. The results by Monney et al. lie between the two analytical solutions, so that the following expression for the correction factor η_{fc} to account for the influence of the concrete strength can be proposed:

$$\eta_{fc} = \left(\frac{f_c}{30} \right)^{2/5} \quad (4.23)$$

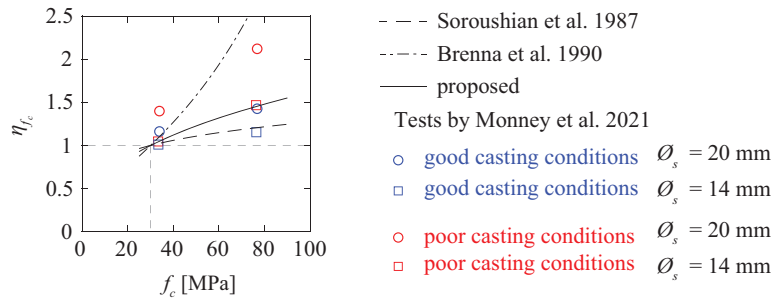


Figure 4.9: Concrete stiffness as a function of the concrete strength, tests by Monney et al. [Mon21] compared to the analytical solutions by Soroushian et al. [Sor87] and Brenna et al. [Bre90] (normalised to provide identical results for $f_c = 30$ MPa, analytical solution by Brenna et al. shown for initial stiffness with $\delta_{\perp} = 0$).

It must be noted that this expression is based on a small number of tests and a phenomenological explanation is still missing. For this reason, this effect deserves to be investigated more in detail in the future.

4.3.4 Interaction with bond

From a phenomenological point of view, the development of secondary cracks near the ribs of reinforcing bars due to bond (Figure 4.10a, see also Goto [Got71]), can reduce the bearing stiffness related to the dowel action. To investigate this effect, a cyclic test reported in [Pej22] ($\varnothing_s = 14$ mm and $\theta = 90^\circ$) has been repeated using plain bars. Figure 4.10b shows the maximum and minimum shear force $V_{dow, min/max}$ as a function of the corresponding transverse displacement δ_\perp for constant V_{dow}/N cycle groups for approximately constant crack opening components parallel to the bar ($\delta_\parallel \approx 0.08$ mm and 0.1 mm). One can observe that the response of the ribbed bar (red markers) is slightly less stiff than for smooth bar (blue markers). Based on this comparison, the following coefficient η_{bond} to reduce the bearing stiffness in Winkler's model to account for the interaction with bond can be proposed:

$$\eta_{bond} = \left(\frac{1}{1 + \delta_\parallel / 0.2} \right)^{1/6} \quad (4.24)$$

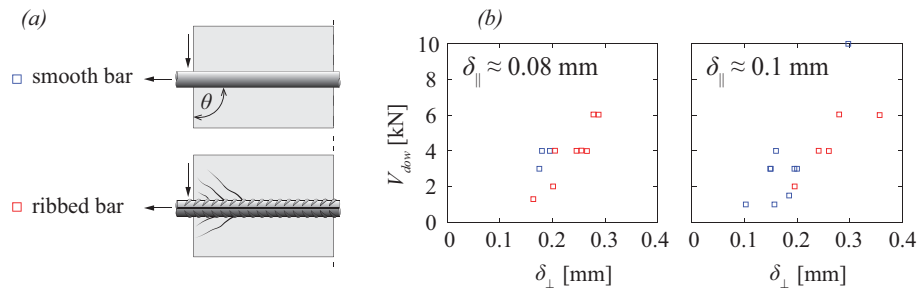


Figure 4.10: (a) Presence of secondary cracks due to bond around ribs in reinforcing bars compared to plain bars and (b) shear force as a function of the transverse displacement δ_\perp for constant δ_\parallel in cyclic tests [Pej22] ($\varnothing_s = 14$ mm and $\theta = 90^\circ$).

Here again, this coefficient is fitted on a very small number of tests, so that additional investigations are needed in the future to verify and probably enhance this relationship.

4.3.5 Influence of the number of cycles

For cyclic loading, a stiffness degradation in the dowel response can also be observed as a function of the number of cycles and of the amplitude of cyclic loads. The dowel tests conducted by Li et al. [Li18] ($\varnothing_s = 12, 20$ and 25 mm and $\theta = 90^\circ$) are analysed to investigate this effect. Figure 4.11a shows the dowel force as a function of the transverse displacement δ_\perp for two identical specimens, one tested under a monotonic load and the other under cyclic loading (colours correspond to the response after the various numbers of cycles N). In all considered

tests, the minimum and maximum cyclic load was 0.5% and 55% of the dowel resistance measured in the monotonic test, respectively. One can observe an increase of the transverse displacement and a considerable degradation of the stiffness with an increasing number of cycles N . Figure 4.11b shows the secant stiffness of the dowel response after the N^{th} cycle normalised to the stiffness at the first cycle with the exponent of 4/3 according to Eq. 4.7, which corresponds to the coefficient η_{cyc} . The results show a larger stiffness degradation for smaller bar diameters. Based on these results, the following coefficient η_{cyc} to account for the number of cycles can be proposed:

$$\eta_{cyc} = 1 - \log N \frac{\phi_s}{200} \quad (4.25)$$

where N is the number of cycles and ϕ_s is the bar diameter.

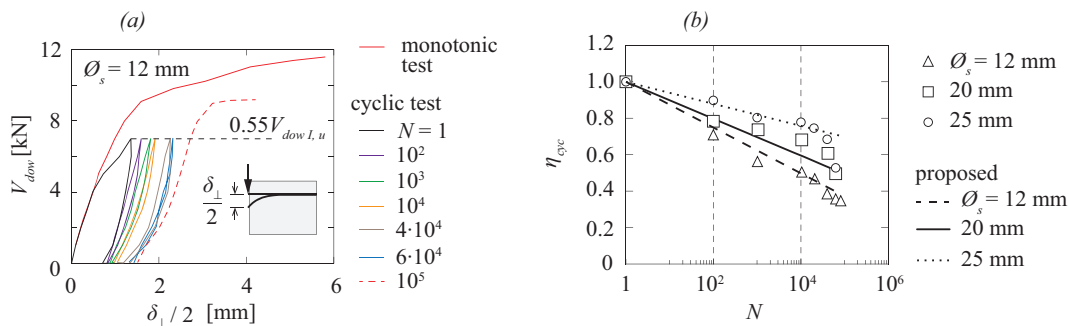


Figure 4.11: (a) Monotonic and corresponding cyclic dowel test after different numbers of cycles N (adapted from Li et al. [Li18]) and (b) proposed coefficient η_{cyc} as a function of the number of cycles (the abscissa is in logarithmic scale).

It must be noted that this expression is based on a small number of tests, so that an additional investigation including a larger range of cyclic conditions is needed in the future.

4.3.6 Solution of Winkler’s equation for different bearing stiffness on opposite sides of the crack

It has been shown in subchapter 4.3.2 that the presence of a free surface near the bar and the direction of the dowel force with respect to the free surface can affect the bearing stiffness and thus the dowel behaviour. As described above, since in actual structures, different cases occur on either side of a crack (namely A with D; B with C; E with H; and F with G), the bearing stiffness on the two sides of the crack can be different. Figure 4.12 shows a case where the bearing stiffness is expected to be smaller on the side where the bar pushes against the concrete cover (case G in Fig. 4.6b) compared to the opposite side where the bar pushes away from the cover (case F in Fig. 4.6b). This asymmetry in the bearing stiffness results in different dowel

behaviours on either side of the crack, leading to different distributions of the bending moment and the corresponding stress $\sigma_{s,flex}$ along the bar (Fig. 4.12).

To predict the dowel behaviour in this case, Winkler's model can be adapted by considering two different bearing stiffnesses k_c^* and k_c on either side of the crack, where $k_c^* \leq k_c$, to be used in the parameters $\beta^* = \sqrt[4]{k_c^* \varnothing_s / (4E_s I_s)}$ and $\beta = \sqrt[4]{k_c \varnothing_s / (4E_s I_s)}$, respectively. The ratio between the two parameters is defined as $k_\beta = \beta^* / \beta$. In this case, the transverse displacement at the crack interface of the bar with the larger bearing stiffness of concrete (Fig. 4.12) becomes $\delta_\perp k_\beta^2 / (1 + k_\beta^2)$, where δ_\perp is transverse component of the relative displacement of the two crack lips (see development in Appendix 4.A). The distance between the crack and the position of the maximum bending moment along the bar, which occurs on the side with the largest bearing stiffness (Fig. 4.12) can be calculated as:

$$x_{\max} = \frac{\arctan k_\beta}{\beta} \quad (4.26)$$

The maximum bending moment along the bar can thus be calculated as:

$$M_{\max} = 2E_s I_s \beta^2 \delta_\perp e^{-\arctan k_\beta} \frac{k_\beta^2}{1 + k_\beta} \frac{1}{\sqrt{1 + k_\beta^2}} \quad (4.27)$$

which can be approximated by:

$$M_{\max} \approx \frac{\beta \beta^* E_s I_s \delta_\perp}{\sqrt{2}} e^{-\pi/4} \quad (4.28)$$

This means that the maximum moment, and thus the maximum steel bending stress, can be calculated using the same equations as for the symmetric case (Eq. 4.10) by replacing the parameter β by the geometric average of parameters β and β^* .

The dowel force can be calculated for $x = 0$ with:

$$V_{dow} = \beta^{*3} E_s I_s \delta_\perp \frac{2}{1 + k_\beta} \frac{2}{1 + k_\beta^2} \quad (4.29)$$

which can be approximated as:

$$V_{dow} \approx \beta \beta^{*2} E_s I_s \delta_\perp \quad (4.30)$$

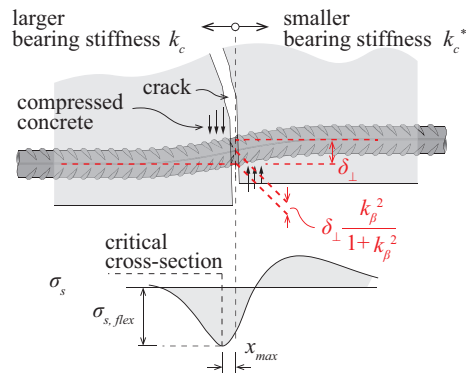


Figure 4.12: Asymmetric dowel behaviour due to the different bearing stiffnesses on opposite sides of the crack.

4.4 Validation of the enhanced expression for the bearing stiffness k_c

In Fig. 4.13, the proposed bearing stiffness k_c according to Eq. 4.17 is compared to the stiffness derived using Winkler's model calculated to fit with the experimental $V_{dow} - \delta_{\perp}$ curves (brown solid line). The results, normalised by the ratio \varnothing_s / E_c , are shown for the dowel tests of series DP from [Pej22], Brenna et al. [Bre90] and Soltani et al. [Sol08] as a function of the transverse displacement δ_{\perp} . The considered tests had various geometrical and material properties (bar diameter, angles θ , etc.). One can observe a satisfactory agreement between the fitted curves from the experimental data and the proposed prediction for the depicted range of the transverse displacement δ_{\perp} .

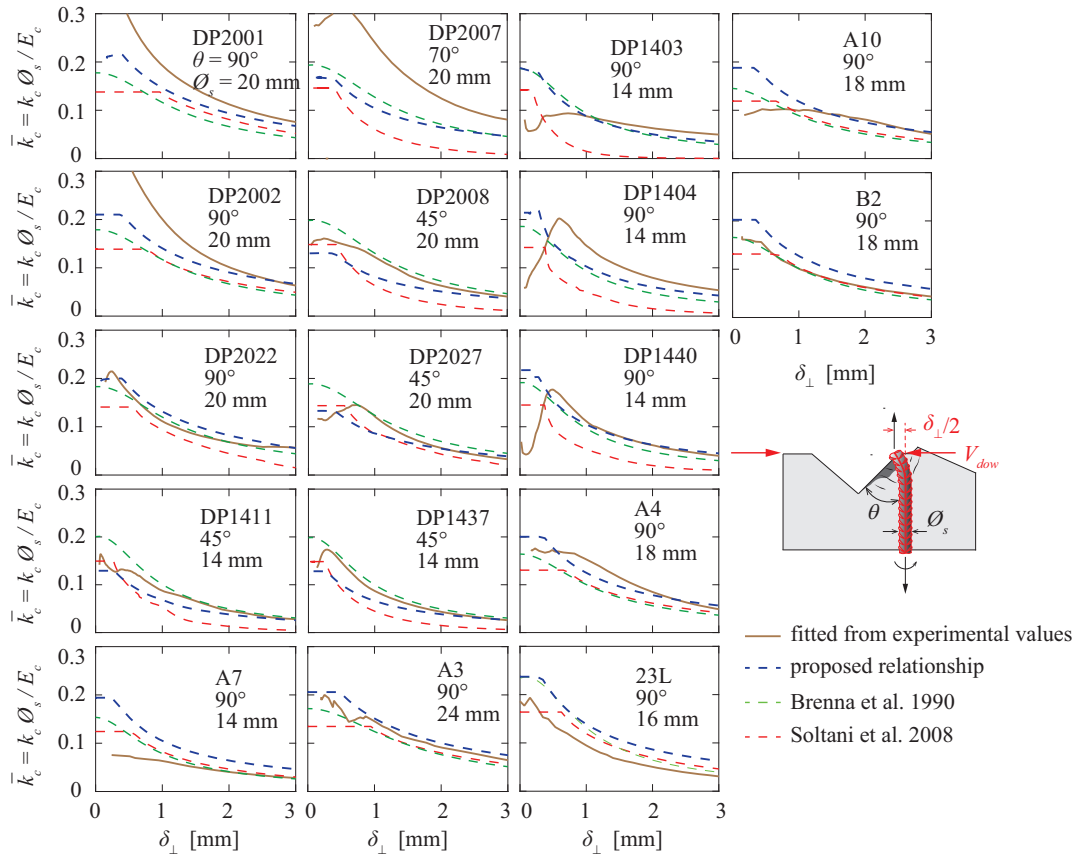


Figure 4.13: Comparison between the predicted and experimental bearing stiffness (fitted from the experimental $V_{dow} - \delta_{\perp}$ curves).

Figure 4.14 shows, for the same tests, the experimental curves ($V_{dow} - \delta_{\perp}$) and the curves according to various models. The first yielding of the reinforcing bar, measured by optical fibres, is identified with a red solid marker. One can observe again a relatively good agreement between the test results and the prediction according to Eq. 4.17 for all tests.

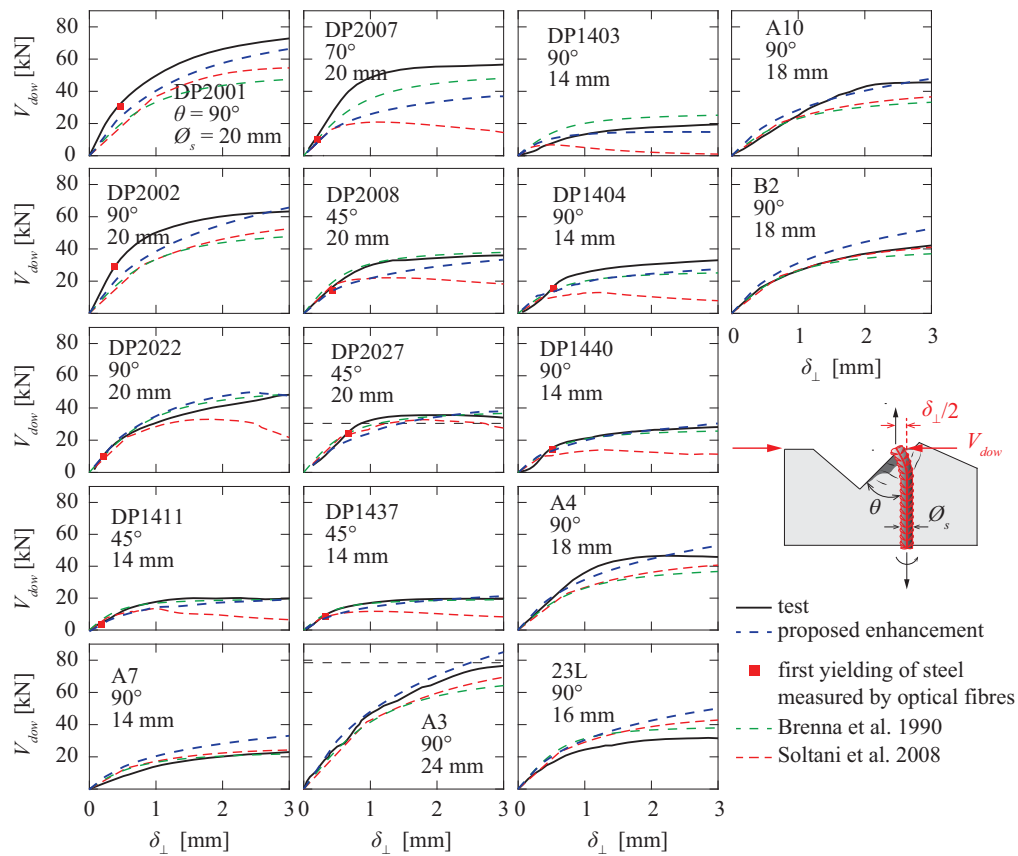


Figure 4.14: Comparison between experimental and predicted $V_{dow} - \delta_{\perp}$ curves.

Figure 4.15 compares the model’s prediction with the proposed stiffness to the optical fibre measurements for test DP2027 from [Pej22]: the normalised axial stress due to bending (Fig. 4.15c, assuming elastic behaviour), the normalised curvature (Fig. 4.15d), the rotation (Fig. 4.15e) and the deformed shape of the reinforcing bar (Fig. 4.15f). The results are shown for five different load levels including the dowel resistance $V_{dow l,u}$. The enhanced model shows a good agreement with the presented measurements for all considered parameters.

Figures 4.15g,h show the comparison between the predicted and measured distance x_{max} between the crack and the most stressed cross-section as a function of the angle θ and the bar diameter \varnothing_s . Again, one can observe a good correspondence between the model and the test results.

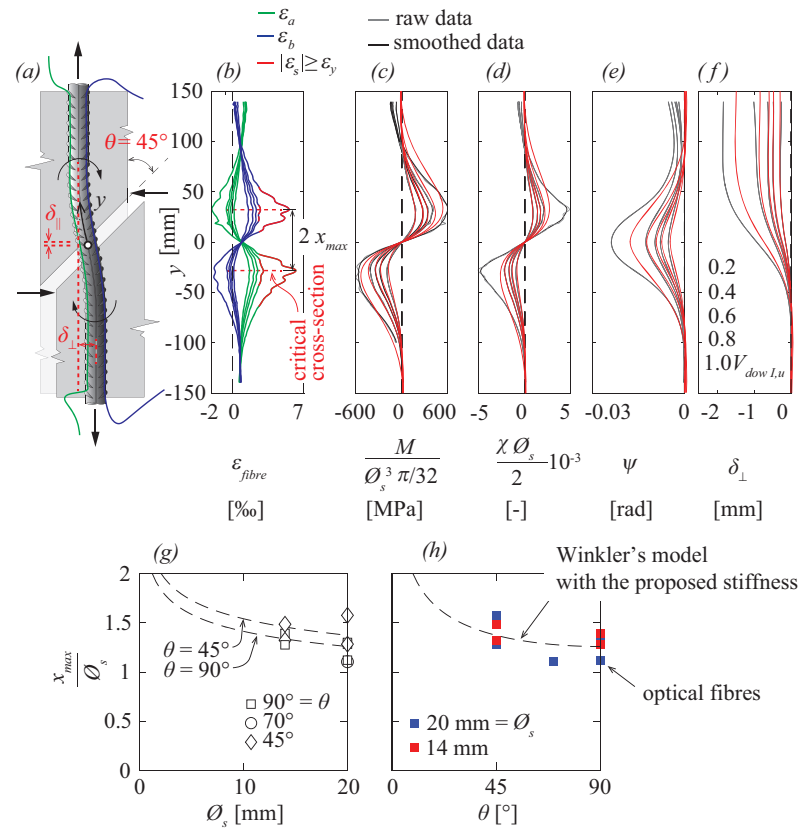


Figure 4.15: Comparison between the optical fibre measurements and the prediction by Winkler's model with the proposed concrete stiffness: (a) bar deformation and parameter definitions; (b) measured strains; (c) normalised moment (stress assuming an elastic behaviour; red line indicates the prediction); (d) normalised curvature; (e) bar rotation; (f) transverse displacement; (g) distance between the crack and the critical cross-section as a function of the bar diameter and (h) as a function of angle between the crack and the bar ((a)-(f): test DP2027 with $\varnothing_s = 20$ mm and $\theta = 45^\circ$, [Pej22]).

In a similar manner, the enhanced model is also validated against a representative cyclic test in Fig. 4.16. Here again, the model provides accurate estimates of the behaviour.

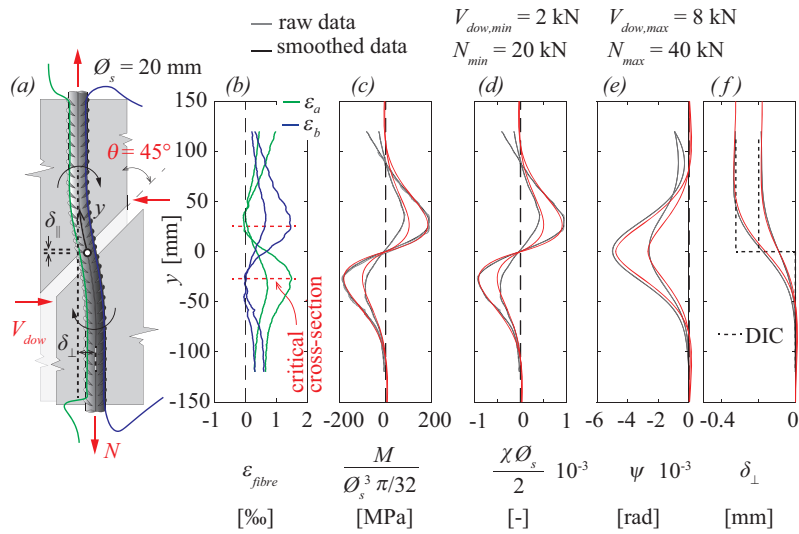


Figure 4.16: Comparison between the enhanced model and the optical fibre measurements: (a) bar deformation and parameter definitions; (b) measured strains; (c-f) derived parameters (specimen DP2027_{cyc} by [Pej22]).

Figure 4.17 compares the predicted peak longitudinal stress $\sigma_{s,flex}$ at the critical cross-section to the fibre measurements normalised with the yield strength f_y . The results are presented for all monotonic tests by [Pej22] at five load levels including the dowel resistance $V_{dow, I,u}$ (with a step of $0.2V_{dow, I,u}$) and for the cyclic tests for the minimum and maximum load levels within a constant V_{dow} / N cycle combination. One can observe a good agreement between the prediction and the measurements with an average of the measured-to-predicted stress ratio of 0.95 and a coefficient of variation $CoV = 12.8\%$ for the considered tests.

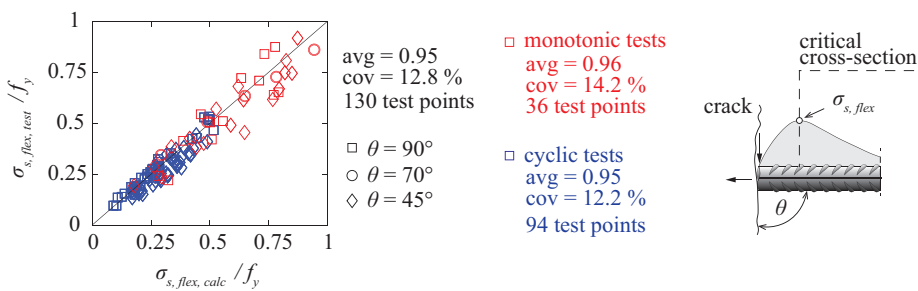


Figure 4.17: Comparison between the predicted and measured peak longitudinal stress $\sigma_{s,flex}$ at the critical cross-section (red markers represent monotonic tests and blue markers cyclic tests).

4.5 Conclusions

This chapter presents a new formulation for the bearing stiffness of concrete under the reinforcing bar to be used in Winkler's model to calculate the steel stresses due to local bending and the maximum shear force in a reinforcing bar due to dowel action related to an imposed transverse displacement. The formulation for the bearing stiffness accounts for various effects and is calibrated based on mechanical considerations and optical fibres measurements. The main conclusions are:

1. The new formulation for the bearing stiffness of concrete in Winkler's model is proposed to account for various effects: angle between the reinforcing bar and the crack, concrete strength, casting conditions, concrete cover and reduction of the stiffness due to a large number of cycles, as well as due to secondary cracks caused by bond.
2. The bearing stiffness under a ribbed bar in case of an imposed crack sliding (transverse displacement) was observed to be slightly smaller than under a smooth bar. This difference is likely due to the secondary cracks which develop near ribs due to bond generated by the imposed crack opening.
3. Like for bond (top bar effect), casting conditions have an influence on the bearing stiffness. Compared to good casting conditions, the bearing stiffness is reduced by more than 50% in case of poor casting conditions, leading to smaller steel stresses due to local bending and smaller dowel forces activated for a given imposed transverse displacement.
4. In case of bars near a free surface, the bearing stiffness increases with the cover-to-bar diameter ratio c / \varnothing_s . The stiffness reaches its maximum value for approximately $c / \varnothing_s = 3$.
5. The analysed cyclic tests have shown an increased shear displacement and a substantial stiffness reduction due to the accumulated damage with an increasing number of cycles.
6. The enhanced bearing stiffness formulation to be used in Winkler's model gives good predictions when compared to tests with respect to shear force-transverse displacement response ($V_{dow} - \delta_{\perp}$) and the peak longitudinal stress $\sigma_{s,flex}$ due to bending measured in the monotonic and low-stress cyclic tests presented in another work by the authors [Pej22].

Appendix 4.A: Solution of Winkler's model for an asymmetric case with different bearing stiffness on opposite sides of the crack

In the case of the different concrete bearing stiffness on opposite sides of the crack, Winkler's model can be adapted by considering two different bearing stiffnesses k_c^* and k_c , where $k_c^* \leq k_c$ (Fig. 4.18), to be used in the parameters $\beta^* = \sqrt[4]{k_c^* \mathcal{O}_s / (4E_s I_s)}$ and $\beta = \sqrt[4]{k_c \mathcal{O}_s / (4E_s I_s)}$, respectively. The ratio between the two parameters is denoted as $k_\beta = \beta^* / \beta$. In this case, the local relative transverse displacement $\tilde{\delta}_\perp$ is described by (Fig. 4.18):

$$\tilde{\delta}_\perp = e^{\beta^* x} (C_1 \cos \beta^* x + C_2 \sin \beta^* x) \quad \text{for } x \leq 0 \quad (4.31)$$

$$\tilde{\delta}_\perp = e^{-\beta x} (C_3 \cos \beta x + C_4 \sin \beta x) \quad \text{for } x \geq 0 \quad (4.32)$$

The constants C_1 to C_4 are calculated based on the four conditions:

- the relative transverse displacement: $\delta_\perp = C_3 - C_1$
- the continuity of the bar rotation at $x = 0$: $k_\beta (C_1 + C_2) = -C_3 + C_4$
- the continuity of the bending moment at $x = 0$: $k_\beta^2 C_2 = -C_4$
- the continuity of the shear force at $x = 0$: $k_\beta^3 (-C_1 + C_2) = C_3 + C_4$

Solving this system of equations upon the unknown constants C_1 to C_4 , one obtains:

$$C_1 = -\frac{\delta_\perp}{1+k_\beta^2} ; C_2 = \frac{\delta_\perp}{1+k_\beta^2} \frac{1-k_\beta}{1+k_\beta} ; C_3 = \delta_\perp \frac{k_\beta^2}{1+k_\beta^2} ; C_4 = -\delta_\perp \frac{k_\beta^2}{1+k_\beta^2} \frac{1-k_\beta}{1+k_\beta} \quad (4.33)$$

Consequently, the bar rotation ψ , the bending moment M and the shear force V in the bar, assuming the elastic behaviour, can be calculated as:

$$\begin{aligned} \psi &= \tilde{\delta}_\perp' = \beta^* e^{\beta^* x} [(C_1 + C_2) \cos \beta^* x + (-C_1 + C_2) \sin \beta^* x] \quad \text{for } x \leq 0 \\ \psi &= \tilde{\delta}_\perp' = \beta e^{-\beta x} [(-C_3 + C_4) \cos \beta x + (-C_3 - C_4) \sin \beta x] \quad \text{for } x \geq 0 \end{aligned} \quad (4.34)$$

$$\begin{aligned} -\frac{M}{E_s I_s} &= \tilde{\delta}_\perp'' = 2\beta^{*2} e^{\beta^* x} (-C_1 \sin \beta^* x + C_2 \cos \beta^* x) \quad \text{for } x \leq 0 \\ -\frac{M}{E_s I_s} &= \tilde{\delta}_\perp'' = 2\beta^2 e^{-\beta x} (C_3 \sin \beta x - C_4 \cos \beta x) \quad \text{for } x \geq 0 \end{aligned} \quad (4.35)$$

$$\begin{aligned}
 -\frac{V}{E_s I_s} = \tilde{\delta}_\perp''' &= 2\beta^{*3} e^{\beta^* x} [(-C_1 + C_2) \cos \beta^* x + (-C_1 - C_2) \sin \beta^* x] \quad \text{for } x \leq 0 \\
 -\frac{V}{E_s I_s} = \tilde{\delta}_\perp''' &= 2\beta^3 e^{-\beta x} [(C_3 + C_4) \cos \beta x + (-C_3 + C_4) \sin \beta x] \quad \text{for } x \geq 0
 \end{aligned}
 \tag{4.36}$$

It must be noted that if the concrete bearing stiffness is the same on both sides of the crack ($k_\beta = 1$), the solution becomes symmetric.

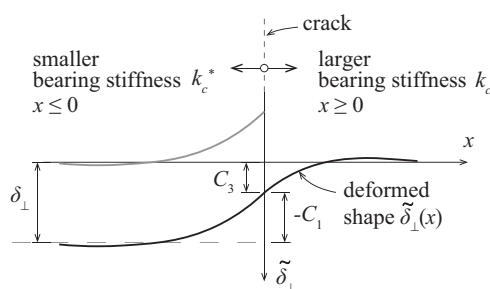


Figure 4.18: Deformed shape of the bar with the different bearing stiffness on opposite crack sides.

For comparison, Figure 4.19 shows the Winkler's model solution for both identical (dashed curves) and different bearing stiffness (solid curves) on opposite sides of the crack. The values on the ordinates are normalised with respect to the maximum values of the case with identical bearing stiffness on both sides of the crack. The ratio of the stiffness parameters is assumed $k_\beta = 0.6$. One can observe that the solution with the different stiffnesses yield smaller peak values of the bar rotation (Fig. 4.19c), bending moment (Fig. 4.19b) and shear force (Fig. 4.19d) in the bar for the same transverse displacement δ_\perp compared to the case with the identical stiffness. This is due to the fact that on one side of the crack, the bearing stiffness is reduced compared to the symmetric case.

Steel stresses and shear forces in reinforcing bars due to dowel action

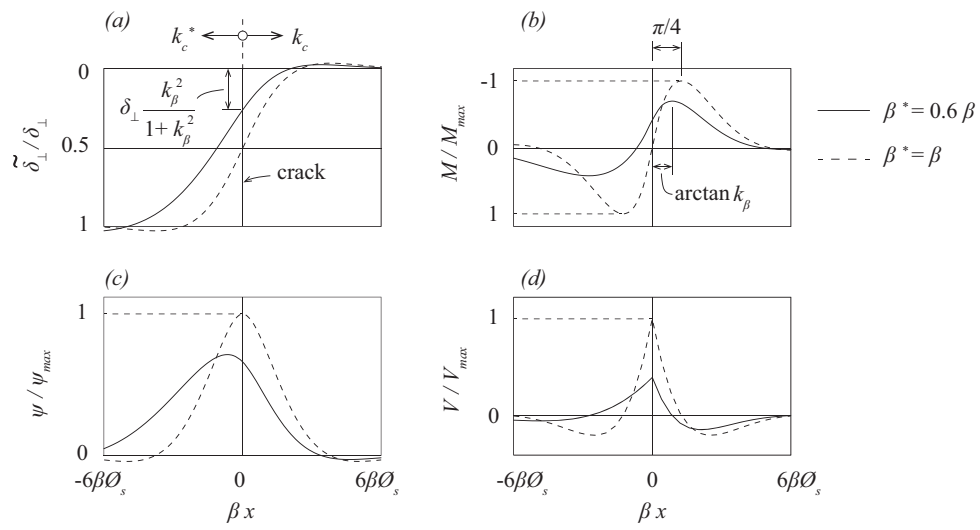


Figure 4.19: Comparison between the Winkler's model solution with the identical (dashed curves) and different bearing stiffness (solid curves) on opposite crack sides of the bar: (a) relative transverse displacement; (b) bending moment; (c) rotation and (d) shear force (normalised values).

Nomenclature

Latin characters: lower case

c	concrete cover
$c_{x,y}$	concrete cover in two orthogonal directions
f_c	uniaxial compressive concrete strength
f_y	yield strength of the rebar
\bar{k}_c	$= k_c \varnothing_s / E_c$
k_c, k_c^*	bearing concrete stiffness under the rebar
k_β	ratio between two stiffness parameters
p	internal pressure
q / \varnothing_s	contact pressure between concrete and the rebar
x	length of the loaded area under the bar
x_{max}	position of the critical cross-section in the rebar

Latin characters: upper case

$C_1 - C_4$	constants
E_c	elastic modulus of concrete
E_s	elastic modulus of the rebar
I_s	moment of inertia of the rebar
M	bending moment in the rebar
M_{max}	maximum bending moment in the bar
N	axial force in the rebar; number of cyclic loads
$N_{min / max}$	minimum / maximum axial force within a cyclic combination
V	shear force in the rebar
V_{dow}	dowel force
$V_{dow I,u}$	first-order dowel resistance
$V_{dow, min / max}$	minimum / maximum shear force within a cyclic combination

Greek characters: lower case

β, β^*	stiffness parameter in Winkler's model
δ	measured displacement
$\delta_{ }$	crack opening component in the direction of the rebar
δ_{\perp}	transverse displacement
$\tilde{\delta}_{\perp}$	local transverse displacement
$\Delta\delta_{\perp}$	variation of the transverse displacement
$\Delta\sigma_{s,flex}$	variation of the longitudinal stress in the rebar due to bending at the critical cross-section

Steel stresses and shear forces in reinforcing bars due to dowel action

$\varepsilon_{fibre/a/b}$	strains measured by optical fibres on both sides of the rebar
η_{bond}	coefficient accounting for secondary cracks due to the axial force
η_c	coefficient accounting for the thickness of the concrete cover
η_{cast}	coefficient accounting for the casting conditions
η_{cyc}	coefficient accounting for the number of cyclic loads
η_{fc}	coefficient accounting for the concrete strength
η_δ	coefficient accounting for the bearing stiffness reduction due to the transverse displacement
η_θ	coefficient accounting for the angle between the bar and the crack
θ	angle between the crack and the rebar
λ	coefficient accounting for the spring length
$\sigma_{s,flex}$	longitudinal stress in the rebar due to bending at the critical cross-section
χ	curvature of the rebar
ψ	rotation of the rebar
<i>Others</i>	
\varnothing_s	diameter of the dowel bar

Chapter 5

A contribution to predicting the dowel resistance

This chapter contributes to predicting the dowel resistance by extending Rasmussen's model to cases where the angle between the bar and the concrete interface is smaller than 90° . Additionally, it demonstrates the application of the upper bound approach of limit analysis for estimating the dowel resistance. No publication related to this chapter has been produced.

This work was conducted by Marko Pejatović under the supervision of Prof. Aurelio Muttoni who consistently offered the constructive feedback, proofreading and manuscript revisions.

The main contributions of Marko Pejatović to this chapter are the following:

- Collection of the database with 142 dowel tests.
- Calibration of the concrete confinement factor based on optical fibre measurements and the collected dowel tests.
- Elaboration of the figures included in the chapter.
- Manuscript preparation of the chapter.

5.1 Rasmussen's model

5.1.1 Solution of Rasmussen's model

Rasmussen's model [Ras62] was developed based on limit analysis to predict the dowel resistance $V_{dow I,u}$ as follows:

$$V_{dow I,u} = \alpha_e \varnothing_s^2 \sqrt{\frac{\eta_3 f_c f_y}{3}} \quad (5.1)$$

where η_3 is a confinement factor accounting for the increase of concrete strength under the bar due to the triaxial stress state, f_c is the uniaxial compressive concrete strength, \varnothing_s is the bar diameter, f_y is the yield strength of the bar and α_e is a coefficient accounting for the distance between the point of contraflexure in the bar and the crack interface (eccentricity e , position of the applied force). The coefficient α_e is given by:

$$\alpha_e = \sqrt{1 + c_e^2 \frac{\eta_3}{3}} - c_e \sqrt{\frac{\eta_3}{3}} \quad (5.2)$$

where c_e is calculated as:

$$c_e = 3 \frac{e}{\varnothing_s} \sqrt{\frac{f_c}{f_y}} \quad (5.3)$$

For the case of a reinforcing bar crossed by a crack or an interface between concrete cast at different times, the eccentricity e can be neglected so that the coefficient α_e becomes 1.

The original Rasmussen's model assumed the full bending resistance M_p in the bar without any axial force N applied (Fig. 5.1a). To account for the reduction of the bending resistance due to the axial force, the model can be adapted [Sor86, FIB13] according to the plastic domain of the reinforcing bar (Fig. 5.1b), so that the Eq. 5.2 becomes:

$$\alpha_e = \sqrt{1 - \frac{N^2}{N_p^2} + c_e^2 \frac{\eta_3}{3}} - c_e \sqrt{\frac{\eta_3}{3}} \quad (5.4)$$

where $N_p = \pi \varnothing_s^2 / 4 f_y$ is the axial resistance accounting for the yield strength of the bar f_y .

Figure 5.1c,d compare the predictions of both the original and the adapted Rasmussen's model to account for the axial force with the dowel tests including an axial force applied and a 90°-angle between the crack interface and the bar (series DP from [Pej24], and Millard et al. [Mil84]). The confinement factor is assumed as $\eta_3 = 3.0$. The results are presented as a function of the axial force N relative to the axial resistance $N_p = \pi \varnothing_s^2 / 4 f_y$. The original model, according to Eq. 5.1 and 5.2, shows relatively good predictions with a tendency to overestimate the resistance for large axial forces applied for tests considered. In this case, an

average value of the measured-to-predicted resistance ratio of 1.04 with a scatter of $CoV = 22.6\%$. This result can be improved using the adapted model (Eq. 5.1 and 5.4) accounting for the axial force, yielding the statistical values of $avg = 1.30$ and $CoV = 17.1\%$. It must be noted that the resistance, for the test with the largest axial force (Fig. 5.1b), is calculated using the tensile strength f_u ($N_u = \pi \varnothing_s^2 / 4 f_u$, accounting for the stress increase due to strain hardening). For comparison, Figure 5.1e shows the comparison between the tests and the prediction of the adapted model where the yield strength f_y is replaced by the tensile strength f_u in Eq. 5.4. In this case, the statistical values are slightly improved: $avg = 1.25$ and $CoV = 16.7\%$.

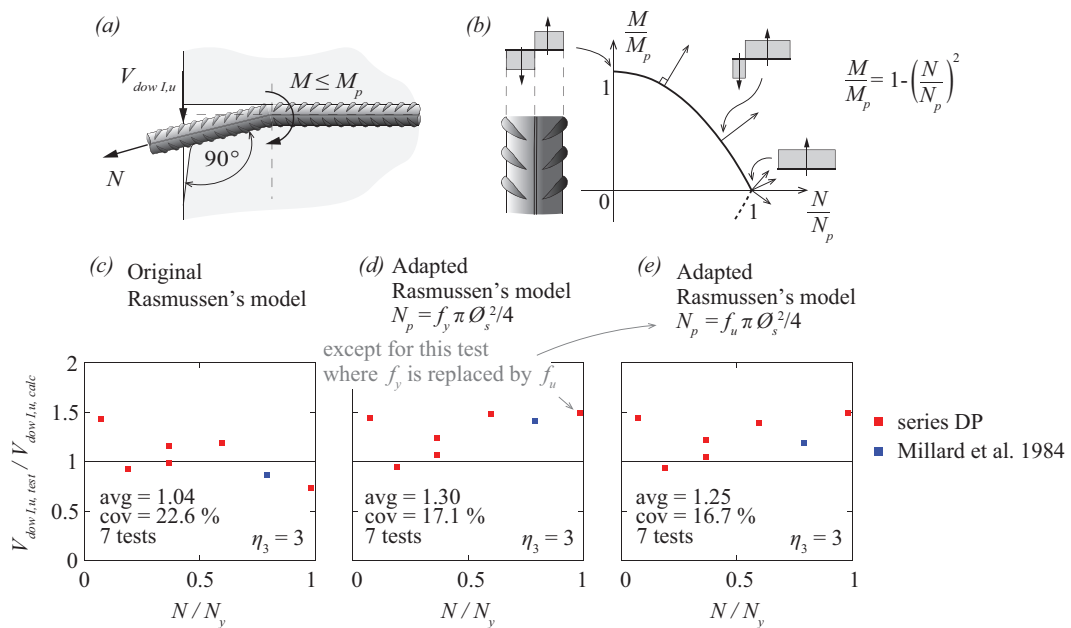


Figure 5.1: (a) Dowel bar with the axial force in the bar with $\theta = 90^\circ$; (b) plastic domain of the reinforcing bar; (c) comparison between the measured and predicted dowel resistance using the original Rasmussen's model; (d) using the adapted Rasmussen's model accounting for the axial force, assuming that the axial resistance of the bar is calculated using the yield strength f_y and (e) using the tensile strength f_u . Note that for all comparisons, the confinement factor is assumed as $\eta_3 = 3.0$.

5.1.2 Enhancement of Rasmussen's model and validation

Rasmussen's model was originally derived for $\theta = 90^\circ$. For this case, several values of the confinement factor η_3 were proposed, $\eta_3 = 5.1$ according to Rasmussen [Ras62], $\eta_3 = 3.0$ according to Tanaka et al. [Tan11], etc. If angles $\theta < 90^\circ$, the concrete confinement under the bar reduces. To account for this reduction, the factor η_3 can be calculated using two different approaches.

In the first approach, the factor η_3 is calculated by integrating the contact pressure between the concrete and the bar (Fig. 5.2a) measured by optical fibres presented in [Pej24]. This way, the equivalent stress over the length x_{max} is calculated with the pressure equal to $\eta_3 f_c$ (Fig. 5.2a).

In the second approach, the factor η_3 is calculated using Rasmussen's model (Eq. 5.1) and the measured dowel resistances $V_{dow\ I,u,test}$ as follows:

$$\eta_3 = \frac{3}{f_c f_y} \frac{V_{dow\ I,u,test}^2}{\varnothing_s^4} \quad (5.5)$$

The calculated factor η_3 is shown in Fig. 5.2b,c as a function of the angle θ . One can observe that η_3 increases with the angle θ in the studied range. Based on these results, the expression for η_3 is proposed:

$$\eta_3 = (\theta/45^\circ)^2 \leq 3 \quad (5.6)$$

Due to the lack of experiments for $\theta > 90^\circ$, the upper limit of $\eta_3 = 3$ is adopted.

Figure 5.2d compares the prediction with the proposed factor η_3 with 16 dowel tests with $\theta < 90^\circ$ without axial force. The results are in good agreement, with an average of measured-to-predicted resistance of 1.12 and a coefficient of variation of 14.0%. For comparison, Figure 5.2e shows that Dulacska's model [Dul72] yielding similar results with the statistical values $avg = 1.0$ and $CoV = 15.8\%$.

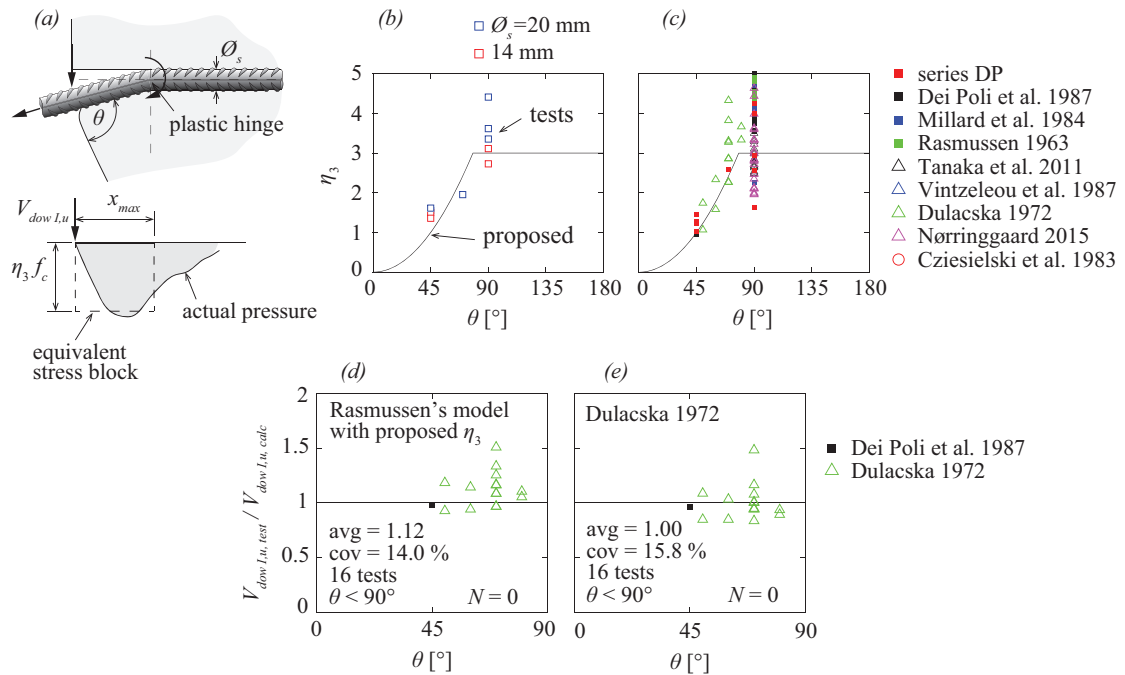


Figure 5.2: (a) Dowel action and pressure between the bar and the concrete at ultimate load; (b) concrete confinement factor η_3 : proposed and derived values from optical fibre measurements [Pej24] assuming the uniform stress between the crack and the plastic hinge; (c) from Rasmussen's model as a function of the angle θ ; (d) prediction of enhanced Rasmussen's model accounting for the proposed η_3 and (e) prediction of Dulacska's expression as a function of the angle θ .

Finally, Figure 5.3 shows a comparison between Rasmussen's model accounting for both the axial force and the proposed confinement factor η_3 , and 142 dowel tests. The results give an average value of measured-to-predicted resistance of 1.15 and a coefficient of variation of $CoV = 16.3\%$.

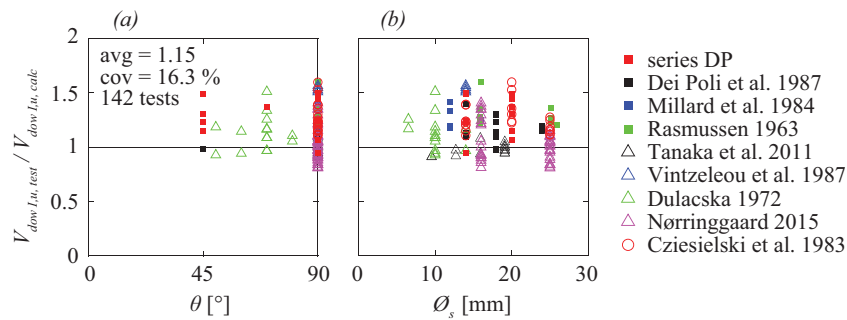


Figure 5.3: Comparison between dowel tests and the prediction by Rasmussen's model accounting for the axial force and the proposed confinement factor η_3 as a function of (a) the angle θ and (b) the bar diameter.

5.2 Conclusions

This chapter presents the extension of Rasmussen's model to cases when the angle between the bar and the crack is smaller than 90° . It also verifies the existing adaptation of the model in case of the axial force applied. The main conclusions are:

1. The existing adaptation of the Rasmussen's model to account for the axial force in the bar shows satisfactory predictions of the dowel resistance when compared to considered dowel tests.
2. The dowel resistance reduces with the decreasing angle between the crack and the bar θ .
3. The confinement factor η_3 accounting for the tri-axial stress state in concrete under a reinforcing bar is calculated based on the optical fibre measurements and measured dowel resistances using Rasmussen's model. Both approaches yield similar results, indicating the reduction of the confinement factor with the decreasing angle θ .
4. Based on these results, the confinement factor to be used in Rasmussen's model is proposed as a function of the angle θ , yielding relatively good predictions of the dowel resistance compared to tests.

Nomenclature

Latin characters: lower case

e	distance between the shear force and the crack
f_c	uniaxial compressive concrete strength
f_y	yield strength of the rebar
f_u	tensile strength of the rebar

Latin characters: upper case

E_s	elastic modulus of the rebar
M_p	bending resistance of the rebar
N	axial force
N_p	plastic resistance of the reinforcing bar
$V_{dow\ 1,u}$	first-order dowel resistance

Greek characters: lower case

α_e	coefficient accounting for the eccentricity of the dowel force
η_3	concrete confinement factor
θ	angle between the crack and the rebar

Others

\emptyset_s	diameter of the dowel bar
---------------	---------------------------

A contribution to predicting the dowel resistance

Chapter 6

Conclusions and Outlook

This chapter summarises the conclusions of all the chapters of this thesis. Additionally, a research outlook addressing recommendations for the future work is included.

6.1 Conclusions

Codes of practice can be too conservative, particularly for the shear resistance of shear reinforced concrete members with considerable direct strutting, due to large loads applied near supports. This thesis introduces a design approach for reinforced concrete members with shear reinforcement based on the stress field method, aiming at providing accurate values for the design or verification of both slender and squat members. Subsequently, the thesis presents a model to better understand the behaviour of steel and concrete due to dowel action in reinforcing bars.

The models based on stress fields, as for example the Variable-Angle Truss models, can be used for the design of slender members with shear reinforcement, as proposed by EN 1992-1-1:2004 or Model Code 2010. However, this approach neglects the direct strut action and thereby underestimates the shear resistance. To account for the direct strut, this type of approach has been empirically adjusted. This thesis presents the design approach of members with shear reinforcement based on stress field which provide a smooth transition between slender and squat members, accounting for direct strutting conditions.

Reinforcing bars are commonly designed to carry axial forces, neglecting their ability to resist transverse forces by dowel action, which can be beneficial for the shear resistance, but detrimental for the fatigue life. To contribute to a better understanding of dowel action, this thesis presents two test series: dowel tests under monotonic or low stress-level cyclic actions with optical fibre and digital image correlation measurements, and tests of the behaviour of concrete underneath the bar.

With respect to the stress prediction in reinforcing bars due to dowel action, this thesis presents a new formulation for the bearing stiffness of concrete under the bar to be used in Winkler's model as a function of the transverse displacement.

The key conclusions of this work, categorized by chapter, are outlined below.

Chapter 2: *Design of slender and squat reinforced concrete members with shear reinforcement*

1. The design of squat members using empirical corrections of the shear resistance of slender members, as proposed by several codes of practice (as EN 1992-1-1:2004 or Model Code 2010) lacks the mechanical background and yields predictions with a larger scatter.
2. The stress field method can be developed for the shear response of squat and slender members resulting in simple and mechanically-sound formulae. This method yields safe results for the design of new structures (lower-bound of the resistance). More refined models are possible to use for the assessment of existing structures, by optimization of the failure load. Such a method can be formulated with increasing level of refinement following a Levels-of-Approximation approach.
3. A method named Stress Fields with a concentrated strut (CSSF) are presented to be used for various shear slenderness, allowing for a smooth transition between members with and without direct strutting conditions. It consists of the combination of an inclined direct strut and two fan regions, and can be interpreted as a simplification of the Elastic-Plastic Stress Field (EPSF) method. The CSSF is simple to use yielding accurate estimates of the shear resistance. This model enables to calculate the efficiency factor ν accounting for cracking in concrete, the inclination of the compression field θ and the tensile strains in the shear reinforcement accounting for compatibility of deformations at a control point (located at centre of the clear shear span).
4. CSSF can be considered using two levels of refinement. The first (LoA I) is intended for simple design of new structures, assuming a constant value of the efficiency factor of concrete ($\nu = 0.5$) and limiting the angle of the compression field as performed for slender members. The second is a more refined approach (LoA II) intended for detailed design or for the assessment of existing structures. It enables to calculate the ν values based on the strain state in the web, without limiting the angle of the compression field.
5. Both the simplified and the refined CSSF method yield more accurate predictions of the shear resistance than those of EN 1992-1-1:2004. This is particularly the case of the refined method. Both of them are implemented in the second generation of Eurocode 2 and in MC2020.

Chapter 3: *Experimental investigation of dowel action in reinforcing bars using refined measurements*

1. The observed dowel response shows a strong dependency on the angle between the bar and the crack, the bar diameter and the applied crack kinematics. Larger angles between the bar and the crack and larger bar diameters lead to a stiffer dowel response and a larger first-order ultimate load. The linear and non-linear regime of the dowel response are governed by the imposed crack kinematics.
2. Large shear forces in the bar associated to large imposed transverse displacements lead to concrete crushing under the bar near the crack. The combination of bending and axial force in the bar cause yielding of the bar.
3. The dowel resistance due to large transverse displacements consists of two contributions: the first-order ultimate dowel force associated with a shear force in the bar and the second-order catenary force associated with the axial force and the rotation of the bar in the crack region.
4. As observed from the optical fibre measurements, the largest bending stress in the bar is located approximately 1.5 times the bar diameter \varnothing_s from the crack.
5. The dowel behaviour is strongly influenced by the angle between the crack and the bar.
6. A considerable degradation of the concrete stiffness under the bar occurs at approximately 40% to 60% of the first-order ultimate load (shear resistance before activating the catenary action). The degradation rate remains approximately constant across all specimen configurations with respect to the normalized transverse displacement.
7. Monotonic and low-stress amplitude cyclic tests show similar dowel responses within the studied service-load domain. Furthermore, several low-stress cycles do not reduce significantly the stiffness.
8. The existing models considered yield reasonably accurate predictions of the concrete stiffness under the bar, the first-order dowel resistance and the dowel plastic response. Several aspects deserve to be improved, particularly regarding the influence of the angle between the crack and the bar as well as the influence of the axial force.

Chapter 4: *Steel stresses and shear forces in reinforcing bars due to dowel action*

1. The new formulation for the concrete bearing stiffness under the bar to be used in Winkler's model is proposed to account for various effects: angle between the reinforcing bar and the crack, concrete strength, casting conditions, concrete cover and reduction of the stiffness due to a large number of cycles, as well as due to secondary cracks caused by bond.

2. The bearing stiffness under a ribbed bar in case of an imposed crack sliding (transverse displacement) was observed to reduce compared to a smooth bar. This reduction is likely due to the secondary cracks which develop near ribs due to bond mobilized by the imposed crack opening.
3. Similar to bond (top bar effect), casting conditions affect the bearing stiffness of concrete. Poor casting conditions lead to more than 50% smaller bearing stiffness than good casting conditions, resulting in smaller steel stresses due to local bending and smaller dowel forces activated for a given imposed transverse displacement.
4. In case of bars near a free surface, the bearing stiffness increases with the cover-to-bar diameter ratio c / \varnothing_s . The stiffness reaches its peak value for approximately $c / \varnothing_s = 3$.
5. The analysed tests under cyclic loading show an increased shear displacement and a considerable stiffness degradation due to the accumulated damage with an increasing number of cycles.
6. The proposed bearing stiffness formulation to be used in Winkler's model gives good predictions when compared to tests in terms of the shear force-transverse displacement response ($V_{dow} - \delta_{\perp}$) and the peak longitudinal stress $\sigma_{s,flex}$ due to bending measured in the monotonic and low-stress cyclic tests.

Chapter 5: *A contribution to predicting the dowel resistance*

1. The adaptation of the Rasmussen's model to account for the axial force in the bar, proposed by other authors, shows satisfactory predictions of the dowel resistance when compared to considered dowel tests.
2. The dowel resistance reduces with the decreasing angle between the crack and the bar θ .
3. The confinement factor η_3 of concrete under a bar is calculated based on the optical fibre measurements and measured dowel resistances using Rasmussen's model. Both approaches give similar results, indicating the reduction of the confinement factor with the decreasing angle θ .
4. Based on these results, the confinement factor to be used in Rasmussen's model is proposed as a function of the angle θ , showing relatively good predictions of the dowel resistance compared to tests.

6.2 Outlook and future works

Several questions regarding the topics in this thesis still remain open. In the following, some aspects that could be further studied are outlined:

Chapter 2: *Design of slender and squat reinforced concrete members with shear reinforcement*

1. The influence of flanges on the load-carrying capacity of non-rectangular reinforced concrete beams could be investigated using stress fields. This could allow refining the design, accounting for beneficial effect of flanges.
2. The research has shown that the strain conditions in slender members are different from those in squat members with considerable direct strutting. The transition between these two cases could be further investigated. To that aim, an experimental campaign should be conducted including shear tests of beams with the various shear slenderness with the detailed measurements on the web surface.
3. The stress fields with the concentrated direct strut and the strut with full spreading could be combined in a single stress field. Such a stress field could allow for a transition between cases with the large and small activation of the web reinforcement.
4. The stress fields accounting for the spread direct strut need to be improved for the cases of members with flanges. To that aim, one should consider a spreading of stresses through the flange which could change the strain conditions in the web.
5. The applicability of the stress fields approach can be arguable in cases of the small amount of shear reinforcement or its small ductility, which could be the case in old structures. A further investigation of such cases could be conducted experimentally and theoretically.

Chapter 3: *Experimental investigation of dowel action in reinforcing bars using refined measurements*

1. This research has shown that the measurement technique using distributed optical fibres is very efficient in studying experimentally the dowel action in small specimens designed to investigate this effect. However, similar investigations could be conducted on large-scale concrete members. Such an investigation could include various parameters such as the bar diameter, the angle between the concrete and the bar, the crack kinematics, the casting conditions, and the concrete cover.
2. Tests of the compressed concrete under the uniformly loaded reinforcing bar show a strong dependence on the concrete cover and casting conditions. However, these effects could be studied directly in dowel tests. This would allow further investigation of their influence on both the dowel resistance and stiffness.

3. The influence of the angle between the concrete and the bar could be further investigated. Additional dowel tests could also include the angles larger than 90° .
4. Low-stress cyclic tests could be extended to large-stress cyclic tests. Refined measurements could provide the important information on the stiffness deterioration due to the non-linear behaviour of both concrete and the reinforcement.
5. Cyclic tests could be performed with a large number of cycles to investigate the potential fatigue failure of dowels. This could cover a wide range of cyclic conditions.
6. Additional dowel tests could be conducted, including visible crack faces for DIC measurements. This could enable the detailed investigation of the concrete behaviour underneath the bar.

Chapter 4: *Steel stresses and shear forces in reinforcing bars due to dowel action*

1. The influence of spalling cracks (also called delamination cracks) on the dowel behaviour due to sufficiently large dowel forces pushing against the concrete cover needs to be further studied. To that aim, an experimental campaign could be performed including the various thicknesses of the concrete cover.
2. The impact of secondary cracks resulting from axial forces in ribbed bars on the bearing stiffness of concrete requires deeper investigation. For this purpose, an experimental campaign should be performed encompassing both smooth and ribbed bars of varying diameters, subject to different imposed crack openings.
3. The influence of cyclic loading on the bearing stiffness needs to be further investigated. To that aim, an experimental campaign should be conducted including cyclic conditions in the range of service loads with a large number of cycles. Various material and geometrical properties could be considered.
4. The influence of the concrete strength on the bearing stiffness needs to be further corroborated with additional tests. These tests could include concrete prisms with various concrete strengths in which short rebars are pressed to reproduce the dowel behaviour as well as dowel tests.
5. Winkler's assumption of the uniform bearing stiffness along the bar could be explored. By considering a non-uniform stiffness distribution, solving the beam equation might yield results that capture the local behaviour of the concrete near the crack.
6. The influence of the casting conditions and the concrete cover on the bearing stiffness and on the dowel resistance need to be investigated more in detail and the case with corner reinforcing bars deserved to be investigated experimentally.

Chapter 5: *A contribution to predicting the dowel resistance*

1. The influence of the large axial forces in the reinforcing bar on the dowel resistance should be further investigated. This is particularly the case for the axial forces close to the axial resistance.
2. The dowel resistance is strongly influenced by concrete crushing and spalling, as well as splitting cracks under the bar. For this reason, these phenomena should be further investigated experimentally and numerically.
3. An actual pressure between the reinforcing bar and concrete at dowel failure can be further investigated numerically. Such analyses would enable to analyse large number of parameters. This would enable to analyse the confinement conditions in concrete under the bar.

Conclusions and Outlook

Bibliography

- [AAS20] **AASHTO**, *AASHTO LRFD Bridge Design Specifications, 9th Edition*, Washington D.C., USA, 2020.
- [ACI08] **ACI**, *ACI 318-08: Building Code Requirements for Structural Concrete*, ACI Committee 318, 467 p., USA, 2008.
- [ACI19] **ACI**, *Building Code Requirements for Structural Concrete (ACI 318-19) and Commentary on Building Code Requirements for Structural Concrete (ACI 318R-19)*, American Concrete Institute, 623 p., Farmington Hills, USA, 2019.
- [ASC98] **ASCE-ACI Committee 445**, *Recent Approaches to Shear Design of Structural Concrete*, ASCE Journal of Structural Engineering, Vol. 124, pp. 1375-1417, USA, 1998.
- [Asi00] **Asin M.**, *The behaviour of reinforced concrete deep beams*, Delft University of Technology, PhD thesis, 188 p., The Netherlands, 2000.
- [Aut23] **Autrup F., Joergensen H. B., Hoang L. C.**, *Dowel action of the tensile reinforcement in RC beams without shear reinforcement: Novel experimental investigation and mechanical modelling*, Engineering Structures, Vol. 279, 115471, pp. 13, 2023.
- [Bac80] **Bach F., Nielsen M. P., Braestrup M. W.**, *Shear Tests on Reinforced Concrete T-Beams - Series V, U, X, B and S*, Structural Research Laboratory, Technical University of Denmark, Report No 120, 87 p., Copenhagen, Denmark, 1980.
- [Bad21a] **Bado M. F., Casas J.-R.**, *A Review of Recent Distributed Optical Fiber Sensors Applications for Civil Engineering Structural Health Monitoring*, Sensors, Vol. 21, No 5, pp. 1-83, 2021.
- [Bad21] **Bado M. F., Casas J.-R., Kaklauskas G.**, *Distributed Sensing (DOFS) in Reinforced Concrete members for reinforcement strain monitoring, crack detection and bond-slip calculation*, Engineering Structures, Vol. 226, 111385, 13 p., 2021.
- [Bau70] **Baumann T., Rüschi H.**, *Schubversuche mit indirekter Krafteinleitung : Versuche zum Studium der Verdübelungswirkung der Biegezugbewehrung eines Stahlbetonbalkens*, Deutscher Ausschuss für Stahlbeton, Heft 210, 83 p., Berlin, Germany, German, 1970.
- [Bet18] **Betschoga C., Tue N. V., Ehmann R., Tung N. D.**, *Shear tests on reinforced concrete beams with low amounts of shear reinforcement*, 5th fib Congress - Proceedings for the 2018 fib Congress: Better, Smarter, Stronger, pp. 3607-3615, 2018.

Bibliography

- [Bir09] **Bircher D., Tuchscherer R., Huizinga M., Bayrak O., Wood S. L., Jirsa J. O.**, *Strength and Serviceability Design of Reinforced Concrete Deep Beams*, Center for Transportation Research, University of Texas, Report No. FHWA/TX-09/0-5253-1, 376 p., Austin, 2009.
- [Bou78] **Boussinesq V.J.**, *Équilibre d'élasticité d'un sol isotrope sans pesanteur, supportant différent poids*, Comptes Rendus, Vol. 86, pp. 1260-1263, Paris, France, 1878.
- [Bra19] **Braut A., Hoult N. A.**, *Distributed Reinforcement Strains: Measurement and Application*, ACI Structural Journal, Vol. 116, No. 4, pp. 115-127, 2019.
- [Bre90] **Brenna A., Dei Poli S., di Prisco M.**, *Dowel action: some experimental and theoretical results regarding special concrete*, Studi e Ricerche, School for the design of R/C structures, Milan University of Technology, pp. 321-380, Italian, 1990.
- [Bre63] **Bresler B., Scordelis A. C.**, *Shear Strength of Reinforced Concrete Beams*, ACI Journal, Vol. 60, No. 1, pp. 51-74, 1963.
- [Can20] **Cantone R., Fernández Ruiz M., Muttoni A.**, *A detailed view on the rebar-to-concrete interaction based on refined measurement techniques*, Engineering Structures, Vol. 226, 19 p., 2020.
- [Can21] **Cantone R., Fernández Ruiz M., Muttoni A.**, *Shear force redistributions and resistance of slabs and wide beams*, Structural Concrete, 22, pp. 2443-2465, 2021.
- [Cla51] **Clark A. P.**, *Diagonal tension in reinforced concrete beams*, Journal Proceedings, Vol. 48, No 10, pp. 145-156, 1951.
- [Cor10] **Correlated Solutions**, *Vic-3D 7 Reference Manual*, 108 p., 2010.
- [Cor23] **Corres E., Muttoni A.**, *Bond of steel reinforcement based on detailed measurements: Results and interpretations*, Structural Concrete, 32 p., 2023.
- [Czi83] **Cziesielski E., Friedmann M.**, *Tragfähigkeit geschweißter Verbindungen im Betonfertigteiltbau*, Ernst & Sohn, DAfStb-Heft 346, 149 p., Berlin, German, 1983.
- [De15] **De Wilder K., Lava P., Debruyne D., Wang Y., De Roeck G., Vandewalle L.**, *Stress Field Based Truss Model for Shear-Critical Prestressed Concrete Beams*, The Institution of Structural Engineers, Vol. 3, pp. 28-42, London, UK, 2015.
- [Dei87] **Dei Poli S., di Prisco M., Gambarova P.**, *In tema di trasmissione del taglio negli elementi di calcestruzzo armato. Alcuni risultati sperimentali attinenti alla cosiddetta azione di spinotto*, Studi e ricerche, 303 p., Italian, 1987.
- [Dei92] **Dei Poli S., di Prisco M., Gambarova P.**, *Shear Response, Deformations, and Subgrade Stiffness of a Dowel Bar Embedded in Concrete*, ACI Structural Journal, Vol. 89, No.6, pp. 665-675, Detroit, USA, 1992.

- [Dei93] **Dei Poli S., di Prisco M., Gambarova P.**, *Cover and Stirrup Effects on the Shear Response of Dowel Bar Embedded in Concrete*, ACI Structural Journal, Vol. 90, No. 4, pp. 441-450, Farmington Hills, USA, 1993.
- [Dor18] **Dorafshan S., Thomas R. J., Maguire M.**, *Comparison of deep convolutional neural networks and edge detectors for image-based crack detection in concrete*, Construction and Building Materials, Vol. 186, pp. 1031-1045, 2018.
- [Dru61] **Drucker D. C.**, *On Structural Concrete and the Theorems of Limit Analysis*, IABSE International Association for Bridge and Structural Engineering, Report No.21, Zürich, Switzerland, 1961.
- [Dul72] **Dulacska H.**, *Dowel Action of Reinforcement Crossing Cracks in Concrete*, ACI Structural Journal, Vol. 69, No 12, pp. 754-757, 1972.
- [Ele74] **Eleiott A. F.**, *An experimental investigation of shear transfer across cracks in reinforced concrete.*, M.S. Thesis, Cornell University, Ithaca, 1974.
- [Eur21] **Eurocode 2**, *Design of concrete structures - Part 1-1: General rules, rules for buildings, bridges and civil engineering structures*, Stable version of the draft of the 2nd generation of prEN 1992-1-1:2021, European Committee for Standardization (CEN), Brussels, Belgium, 2021.
- [Eur04] **Eurocode 2**, *Design of concrete structures-Part 1-1: General rules and rules for buildings*, European Committee for Standardization (CEN), 225 p., Brussels, Belgium, 2004.
- [Fer07] **Fernández Ruiz M., Muttoni A.**, *On Development of Suitable Stress Fields for Structural Concrete*, ACI Structural Journal, Vol. 104, No 4, pp. 495-502, Farmington Hills, USA, 2007.
- [Fer08] **Fernández Ruiz M., Muttoni A.**, *Shear strength of thin-webbed post-tensioned beams*, ACI Structural Journal, Vol.105, No 3, pp. 308-317, USA, 2008.
- [Fer21] **Fernández Ruiz M.**, *The influence of the kinematics of rough surface engagement on the transfer of forces in cracked concrete*, Engineering Structures, 231, 17 p., 2021.
- [FIB08] **FIB**, *Structural connections for precast concrete buildings, fib bulletin No. 43*, 370 p., 2008.
- [FIB13] **FIB**, *fib Model Code for Concrete Structures 2010*, fib, First Edition, UK, 2013.
- [FIB21] **FIB**, *Design and assessment with strut-and-tie models and stress fields: from simple calculations to detailed numerical analysis*, Fédération Internationale du Béton - fib Bulletin n°100, 235 p., Lausanne, Switzerland, 2021.

Bibliography

- [Fos98] **Foster S. J., Gilbert R. I.**, *Experimental Studies on High-Strength Concrete Deep Beams*, ACI Structural Journal, Vol. 95, No 4, pp. 382-390, USA, 1998.
- [Fri38] **Friberg B. F.**, *Design of dowels in transverse joints of concrete pavement*, American Society of Civil Engineers, Vol. 64, No 9, pp. 1809-1828, 1938.
- [Gar08] **Garay-Moran J. D., Lubell A. S.**, *Behaviour of Concrete Deep Beams with High Strength Reinforcement*, Department of Civil and Environmental Engineering, University of Alberta, Structural Engineering Report 277, 283 p., Alberta, Canada, 2008.
- [Geh22] **Gehri N., Mata Falcón J., Kaufmann W.**, *Refined extraction of crack characteristics in large-scale concrete experiments based on digital image correlation*, Engineering Structures, 251-A, 21 p., UK, 2022.
- [Got71] **Goto Y.**, *Cracks Formed in Concrete around Deformed Tension Bars*, ACI Journal, Vol. 68, No 4, pp. 244-251, Japan, 1971.
- [Hof69] **Hofbeck J. A., Ibrahim I. O., Mattock A. H.**, *Shear Transfer in Reinforced Concrete*, ACI Journal Proceedings, Vol. 66, No 2, pp. 119-128, 1969.
- [Hu18] **Hu B., Wu Y.-F.**, *Effect of shear span-to-depth ratio on shear strength components of RC beams*, Engineering Structures, Vol. 168, pp. 770-783, 2018.
- [Jen78] **Jensen J. F., Nielsen M. P., Braestrup M. W., Bach F.**, *Nogle plasticitetsteoretiske bjælkeløsningerne [Some plastic solutions concerning the load-carrying capacity of reinforced concrete beams]*, R-101, 31 p., Copenhagen, Denmark, Danish, 1978.
- [Jen79] **Jensen J. F.**, *Plastic solutions for reinforced concrete beams in shear*, IABSE, Vol. 29, pp. 71-78, Copenhagen, Denmark, 1979.
- [Jen81] **Jensen J. F.**, *Plasticitetsteoretiske løsninger for skiver og bjælker af jernbeton (plastic solutions for disks and beams of reinforced concrete)*, Technical University of Denmark, Structural Research Laboratory, PhD thesis, 153 p., Copenhagen, Danish, 1981.
- [Jim79] **Jimenez R., White R. N., Gergely P.**, *Bond and Dowel Capacities of Reinforced Concrete*, Vol. 76, No.1, pp. 73-92, 1979.
- [Kan64] **Kani G. N. J.**, *The riddle of shear failure and its solution*, ACI Journal, Vol. 61, No 4, pp. 441-467, Detroit, USA, 1964.
- [Kat73] **Kato B., Akiyama H., Yamanoushi Y.**, *Predictable properties of materials under incremental cyclic loading*, International Association for Bridge and Structural Engineering, Reports of the Working Commissions, Symposium on resistance and

- ultimate deformability of structures acted on by well-defined repeated loads, Vol. 13, pp. 119-124, 1973.
- [Kau96] **Kaufmann W., Marti P.**, *Versuche an Stahlbetonträgern unter Normal- und Querkraft*, Institut für Baustatik und Konstruktion, ETHZ, No 226, 141 p., Zürich, Switzerland, German, 1996.
- [Kem77] **Kemp E. L., Wilhelm J.**, *An Investigation of the Parameters Influencing Bond Behaviour with a View Towards Establishing Design Criteria*, Department of Civil Engineering, West Virginia University, Report WVDOH 46-2, 244 p., West Virginia, 1977.
- [Kon98] **Kong P. Y. L., Rangan V.**, *Shear Strength of High-Performance Concrete Beams*, ACI Structural Journal, Vol. 95, No 6, pp. 677-688, Farmington Hills, USA, 1998.
- [Kos09] **Kostic N.**, *Topologie des champs de contraintes pour le dimensionnement des structures en béton armé*, Thèse EPFL, n°4414, 235 p., Lausanne, Switzerland, 2009.
- [Kre66] **Krefeld W., Thurston C. W.**, *Studies of the shear and diagonal tension strength of simply supported reinforced concrete beams*, ACI Journal, Vol. 63, No 4, pp. 451-476, 1966.
- [Lee82] **Lee D.**, *An Experimental Investigation in the Effects of Detailing on the Shear Behavior of Deep Beams*, University of Toronto, Department of Civil Engineering, Master Thesis, 1982.
- [Lem22] **Lemcherreq Y., Galkovski T., Mata Falcón J., Kaufmann W.**, *Application of Distributed Fibre Optical Sensing in Reinforced Concrete Elements Subjected to Monotonic and Cyclic Loading*, Sensors, Vol. 22, No 5, 28 p., Basel, Switzerland, 2022.
- [Leo63] **Leonhardt F., Walther R.**, *Schubversuche an Plattenbalken mit unterschiedlicher Schubbewehrung*, Deutscher Ausschuss für Stahlbeton, Wilhelm Ernst & Sohn, Vol. 156, 84 p., Berlin, Germany, German, 1963.
- [Lev89] **Levi F., Marro P.**, *Shear tests up to failure of beams made with normal and high strength concrete*, Design Aspects of High Strength Concrete, Politecnico di Torino, Bulletin No. 193, pp. 13-23, 1989.
- [Li18] **Li P., Tan N., Wang C.**, *Nonlinear Bond Model for the Dowel Action considering the Fatigue Damage Effect*, Hindawi - Advances in Materials Science and Engineering, 11 p., 2018.
- [Liu19] **Liu J.**, *Kinematics-Based Modelling of Deep Transfer Girders in Reinforced Concrete Frame Structures*, University of Liège, PhD thesis, 140 p., Belgium, 2019.

Bibliography

- [Lun13] **Luna Technologies Inc.**, *Optical Backscatter Reflectometer 4600 User Guide*, 227 p., Blacksburg, VA, 2013.
- [Mad90] **Madsen K.**, *Ny beregningsregel for koncentreret last på uarmeret beton [New design rule for concentrated loads on unreinforced concrete]*, Dansk Beton [J. Danish Concr.], Vol. 3, pp. 10-17, Denmark, Danish, 1990.
- [Mae96a] **Maekawa K., Qureshi J.**, *Computational Model for Reinforcing Bar Embedded in Concrete Under Combined Axial Pullout and Transverse Displacement*, Journal of JSCE: Materials, Concrete Structures and Pavements, Vol. 31, No 538, pp. 227-239, 1996.
- [Mae96] **Maekawa K., Qureshi J.**, *Embedded bar behavior in concrete under combined axial pullout and transverse displacement*, J. Materials, Conc. Struct., Pavements, 30, pp. 183-195, 1996.
- [Mar51] **Marcus H.**, *Load Carrying Capacity of Dowels at Transverse Pavement Joints*, ACI Structural Journal, Vol. 48, No.10, pp. 169-184, 1951.
- [Mat20] **Mata Falcón J., Haefliger S., Lee M., Galkovski T., Gehri N.**, *Combined application of distributed fibre optical and digital image correlation measurements to structural concrete experiments*, Engineering Structures, Vol. 225, Page: 111309, Amsterdam, 2020.
- [Mih10] **Mihaylov B., Bentz E. C., Collins M. P.**, *Behavior of Large Deep Beam Subjected to Monotonic and Reversed Cyclic Shear*, ACI Structural Journal, Vol. 107, No 6, pp. 726-734, 2010.
- [Mih13] **Mihaylov B., Bentz E. C., Collins M. P.**, *Two-Parameter Kinematic Theory for Shear Behavior of Deep Beams*, ACI Structural Journal, Vol. 110, No 3, pp. 447-455, 2013.
- [Mil84] **Millard S. G., Johnson R. P.**, *Shear transfer across cracks in reinforced concrete due to aggregate interlock and to dowel action*, Magazine of Concrete Research, Vol. 36, No.126, 1984.
- [Moc20] **Moccia F., Kubski X., Fernández Ruiz M., Muttoni A.**, *The influence of casting position and disturbance induced by reinforcement on the structural concrete strength*, Structural Concrete, 1, 28 p., 2020.
- [Moc20] **Moccia F., Yu Q., Fernández Ruiz M., Muttoni A.**, *Concrete compressive strength: From material characterization to a structural value*, Structural Concrete, 21 p., 2020.
- [Moc21] **Moccia F., Fernández Ruiz M., Metelli G., Muttoni A., Plizzari G.**, *Casting position effects on bond performance of reinforcement bars*, Structural Concrete, Wiley, 21 p., 2021.

- [Moc21] **Moccia F., Fernández Ruiz M., Muttoni A.**, *Spalling of concrete cover induced by reinforcement*, Engineering Structures, 19 p., 2021.
- [Mon21] **Monney F., Fernández Ruiz M., Muttoni A.**, *Design against splitting failures in reinforced concrete due to concentrated forces and minimum bend diameter of reinforcement*, Engineering Structures, Vol. 245, 112902, 23 p., 2021.
- [Mon22] **Monney F., Fernández Ruiz M., Muttoni A.**, *Influence of amount of shear reinforcement and its post-yield response on the shear resistance of reinforced concrete members*, Structural Concrete, pp. 1-33, 2022.
- [Moo54] **Moody K.G., Viest I. M., Elstner R. C., Hognestad E.**, *Shear Strength of reinforced Concrete Beams - Part 1 : Test of Simple Beams*, ACI Journal Proceedings, Vol. 51, No 12, pp. 317-332, 1954.
- [Mül78] **Müller P.**, *Plastische Berechnung von Stahlbetonscheiben und-balken*, Institut für Baustatik und Konstruktion ETH, Report No. 83, Zurich, Switzerland, German, 1978.
- [Mut90] **Muttoni A.**, *Die Anwendbarkeit der Plastizitätstheorie in der Bemessung von Stahlbeton*, Birkhäuser Verlag, Institut für Baustatik und Konstruktion ETH Zürich, No 176, 164 p., Basel, Switzerland, German, 1990.
- [Mut96] **Muttoni A., Schwartz J., Thürlimann B.**, *Design of Concrete Structures with Stress Fields*, Birkhäuser Verlag, 143 p., Basel, Switzerland, 1996.
- [Mut12] **Muttoni A., Fernández Ruiz M.**, *Levels-of-approximation approach in codes of practice*, Structural Engineering International, Vol. 2, pp. 190-194, Zurich, Switzerland, 2012.
- [Mut16] **Muttoni A., Fernández Ruiz M., Niketic F., Backes M.-R.**, *Assessment of existing structures based on elastic-plastic stress fields - Modelling of critical details and investigation of the in-plane shear transverse bending interaction*, Rapport OFROU, N° 680, 134 p., Switzerland, 2016.
- [Nie11] **Nielsen M. P., Hoang L. C.**, *Limit Analysis and Concrete Plasticity*, CRC Press, 3rd edition, 788 p., Boca Raton, USA, 2011.
- [Nik17] **Niketic F.**, *Development of a consistent approach for design and assessment of structural concrete members using stress fields and strut-and-tie models*, EPFL PhD Thesis, n° 7911, 193 p., Lausanne, Switzerland, 2017.
- [Non13] **Nonis C., Niezrecki C., Yu T.-Y., Ahmed S., Su C.-F.**, *Structural health monitoring of bridges using digital image correlation*, Proceedings of SPIE 8695: Health Monitoring of Structural and Biological Systems, Vol. 8695 869507-1, pp. 1-13, San Diego (California), 2013.

Bibliography

- [Nør15] **Nørringgaard P.**, *Dowel Action in Rebars Embedded in Concrete*, Master Thesis, 112 p., 2015.
- [Pas22] **Pastore M. V. F., Vollum R. L.**, *Shear enhancement in RC beams with stirrups simultaneously loaded within 2d and at 3d from supports*, *Engineering Structures*, Vol. 264, pp. 1-18, 2022.
- [Pej22] **Pejatović M., Muttoni A.**, *Experimental investigation of dowel action using advanced measurement techniques*, 14th fib International PhD Symposium in Civil Engineering, pp. 573-580, Rome, Italy, 2022 (a more detailed description of the experimental programme is presented in [Pej24]).
- [Pej24] **Pejatović M., Muttoni A.**, *Experimental investigation of dowel action in reinforcing bars using refined measurements*, *Structural Concrete*, 2024 (Publication submitted).
- [Pla71] **Placas A., Regan P. E.**, *Shear Failure of Reinforced Concrete Beams*, *ACI Structural Journal*, Vol. 68, No 10, pp. 763-773, USA, 1971.
- [Pru88] **Pruijessers A. F.**, *Aggregate Interlock and Dowel Action Under Monotonic and Cyclic Loading*, PhD thesis, Delft University, Netherland, 165 p., 1988.
- [Pun19] **Pundir M., Tirassa M., Fernández Ruiz M., Muttoni A., Anciaux G.**, *Review of fundamental assumptions of the Two-Phase Model for aggregate interlocking in cracked concrete using numerical methods and experimental evidence*, *Cement and Concrete Research*, Elsevier, 125(105855), 1-17, 2019.
- [Ras62] **Rasmussen B. H.**, *Strength of transversely loaded bolts and dowels cast into concrete*, *Laboratoriet for Bugningastatik*, Denmark Technical University, Meddelelse, Vol. 34, No 2, pp. 39-55, Danish, 1962.
- [Rez20] **Rezaie A., Achanta R., Godio M., Beyer K.**, *Comparison of crack segmentation using digital image correlation measurements and deep learning*, *Construction and Building Materials*, Vol. 261, 12 p., 2020.
- [Rog86] **Rogowsky D. M., MacGregor J. G., Ong S. Y.**, *Tests of Reinforced Concrete Deep Beams*, *ACI Journal*, Vol. 83, pp. 614-623, USA, 1986.
- [Rup13] **Rupf M., Fernández Ruiz M., Muttoni A.**, *Post-tensioned girders with low amounts of shear reinforcement: Shear strength and influence of flanges*, *Engineering structures*, Vol. 56, pp. 357-371, 2013.
- [Rus05] **Russo G., Venir R., Pauletta M.**, *Reinforced Concrete Deep Beams-Shear Strength Model and Design Formula*, *ACI Structural Journal*, V. 102, pp. 429-437, USA, 2005.
- [Sag10] **Sagaseta J., Vollum R. L.**, *Shear design of short span beams*, *Magazine of Concrete Research*, Vol. 62, No 4, pp. 267-282, UK, 2010.

- [Sag11] **Sagasetta J., Vollum R. L.**, *Influence of beam cross-section, loading arrangement and aggregate type on shear strength*, Magazine of Concrete Research, Vol. 53, No 2, pp. 139-155, London, UK, 2011.
- [Sah10] **Sahoo D. K., Sagi M. S. V., Singh B., Bhargava P.**, *Effect of Detailing of Web Reinforcement on the Behavior of Bottle-shaped Struts*, Journal of Advanced Concrete Technology, Vol. 8, No 3, pp. 303-314, 2010.
- [Sal05] **Salamy M. R., Kobayashi H., Unjoh S.**, *Experimental and Analytical Study on RC Deep Beams*, Asian Journal of Civil Engineering (AJCE), Vol. 6, No 5, pp. 487-499, 2005.
- [Sen10] **Senturk E. A., Higgins C.**, *Evaluation of Reinforced Concrete Deck Girder Bridge Bent Caps with 1950s Vintage Details: Laboratory Tests*, ACI Structural Journal, Vol. 107, No 5, pp. 534-543, 2010.
- [Sha69] **Sharma N. K.**, *Splitting Failures in Reinforced Concrete Members*, PhD Thesis, 424 p., Ithaca, N.Y., USA: Cornell University, 1969.
- [She07] **Sherwood E. G., Bentz E. C., Collins M. P.**, *Effect of Aggregate Size on Beam - Shear Strength of Thick Slabs*, ACI Structural Journal, Vol. 104, No 2, pp. 180-190, 2007.
- [SIA13] **SIA**, *SIA 262:2013 - Structures en béton*, Société suisse des ingénieurs et des architectes, 102 p., Zurich, Switzerland, 2013.
- [Sig11] **Sigrist V.**, *Generalized Stress Field Approach for Analysis of Beams in Shear*, ACI Structural Journal, Vol. 108, No 4, pp. 479-487, Farmington Hills, USA, 2011.
- [Sig13] **Sigrist V., Bentz E. C., Fernández Ruiz M., Foster S. J., Muttoni A.**, *Background to the Model Code 2010 Shear Provisions - Part I: Beams and Slabs*, Structural Concrete, Vol. 14, No 3, pp. 204-214, Berlin, Germany, 2013.
- [Smi82] **Smith K. N., Vantsiotis A. S.**, *Shear Strength of Deep Beams*, ACI Journal Proceedings, Vol. 79, No 3, pp. 201-213, 1982.
- [Sol08] **Soltani M., Maekawa K.**, *Path-dependent mechanical model for deformed reinforcing bars at RC interface under coupled cyclic shear and pullout tension*, Engineering Structures, Vol. 30, pp. 1079–1091, 2008.
- [Sør74] **Sørensen H. C.**, *Shear Tests on 12 Reinforced Concrete T-Beams*, Technical University of Denmark, No R60, 52 p., Lyngby, Denmark, 1974.
- [Sor17] **Sorensen J. H., Hoang L. C., Olesen J. F., Fischer G.**, *Testing and modeling dowel and catenary action in rebars crossing shear joints in RC*, Engineering Structures, Vol. 145, pp. 234–245, 2017.

Bibliography

- [Sor86] **Soroushian P., Obaseki K., Rojas M., Sim Jongsung**, *Analysis of Dowel Bars Acting Against Concrete Core*, ACI Structural Journal, Vol. 83, No 4, pp. 642-649, 1986.
- [Sor87] **Soroushian P., Obaseki K., Rojas M.**, *Bearing Strength and Stiffness of Concrete Under Reinforcing Bars*, ACI Structural Journal, Vol. 84, No.3, pp. 179-184, 1987.
- [Sta77] **Stanton J. F.**, *An investigation of dowel action of the reinforcement of nuclear containment vessels and their nonlinear dynamic response to earthquake loads*, 1977.
- [Tak19] **Takase Y.**, *Testing and modeling of dowel action for a post-installed anchor subjected to combined shear force and tensile force*, Engineering Structures, Vol. 195, pp. 551–558, 2019.
- [Tan99] **Tan K. H., Lu H.-Y.**, *Shear Behaviour of Large Reinforced Concrete Deep Beams and Code Comparisons*, ACI Structural Journal, Vol. 96, No 5, pp. 836-846, USA, 1999.
- [Tan11] **Tanaka Y., Murakoshi J.**, *Reexamination of dowel behavior of steel bars embedded in concrete*, ACI Journal, Vol. 108, No 6, pp. 659–668, 2011.
- [Tan05] **Tanimura Y., Sato T.**, *Evaluation of Shear Strength of Deep Beams with Stirrups*, QR of RTRI, Vol. 46, No 1, pp. 53-58, 2005.
- [Tay69] **Taylor H. P. J.**, *Investigation of the Dowel Shear Forces Carried by the Tensile Steel in Reinforced Concrete Beams*, Cement and Concrete Association, Report No. TRA 431, 24 p., London, UK, 1969.
- [Tim25] **Timoshenko S., Lessells J. M.**, *Applied Elasticity*, Westinghouse Technical Night School Press, 1925.
- [Tir21] **Tirassa M., Fernández Ruiz M., Muttoni A.**, *An interlocking approach for the rebar-to-concrete contact in bond*, Magazine of Concrete Research, Vol. 73, No 8, pp. 379-393, 2021.
- [Tuc16] **Tuchscherer R., Birrcher D., Bayrak O.**, *Reducing discrepancy between deep beam and sectional shear-strength predictions*, ACI Structural Journal, Vol. 113, No 1, pp. 3-16, 2016.
- [Vec86] **Vecchio F. J., Collins M. P.**, *The modified compression-field theory for reinforced concrete elements subjected to shear*, ACI Structural Journal, Vol. 83, No. 2, pp. 219-231, USA, 1986.
- [Vec04] **Vecchio F. J., Shim W.**, *Experimental and Analytical Reexamination of Classic Concrete Beam Tests*, ASCE Journal of Structural Engineering, Vol.130, pp. 460-469, USA, Anglais, 2004.

- [Vin84] **Vintzeleou E.**, *Mechanisms of Load Transfer along Reinforced Concrete Interfaces under Monotonic and Cyclic Actions*, PhD Thesis, 549 p., National Technical University of Athens, 1984.
- [Vin86] **Vintzeleou E., Tassios T.P.**, *Mathematical models for dowel action under monotonic and cyclic conditions*, Magazine of Concrete Research, Vol. 38, No 134, pp. 13-22, 1986.
- [Vin87] **Vintzeleou E., Tassios T.P.**, *Behavior of Dowels Under Cyclic Deformations*, ACI Structural Journal, Vol. 84, No 1, pp. 18-30, 1987.
- [Wal13] **Walraven J. C., Belletti B., Esposito R.**, *Shear Capacity of Normal, Lightweight, and High-Strength Concrete Beams according to Model Code 2010. I: Experimental Results versus Analytical Model Results*, Journal of Structural Engineering, Vol. 139, No 9, pp. 1593-1599, 2013.
- [Win67] **Winkler E.**, *Die Lehre von der Elastizität und Festigkeit*, Dominicus, 411 p., Prague, Czech Republic, German, 1867.
- [Yos00] **Yoshida Y.**, *Shear reinforcement for large lightly reinforced concrete members*, Master thesis, University of Toronto, 160 p., Toronto, Canada, 2000.
- [Zha07] **Zhang N., Tan K. H.**, *Size effect in RC deep beams: Experimental investigation and STM verification*, Engineering structures, Vol. 29, No 12, pp. 3241-3254, Anglais, 2007.
- [Zha09] **Zhang N., Tan K. H., Leong C. L.**, *Single-Span Deep Beams Subjected to Unsymmetrical Loads*, ASCE Journal of Structural Engineering, Vol. 135, No 3, pp. 239-252, 2009.
- [Zha10] **Zhang N., Tan K. H.**, *Effects of Support Settlement on Continuous Deep Beams and STM Modeling*, Engineering Structures, Vol. 32, No 2, pp. 361-372, 2010.
- [Zim88] **Zimmermann H.**, *Die Berechnung des Eisenbahnoberbaues*, 308 p., Berlin, Germany, German, 1888.

Bibliography

Curriculum Vitae

Pejatović Marko

marko.pejat@gmail.com

+41 78 930 16 22

Born: 14.07.1993

Languages: Montenegrin/Serbian (native), French (fluent), English (fluent), Italian (good)



Education

- 2019 - 2024 **PhD Degree in Civil Engineering**
*Structural Concrete Laboratory (IBETON),
Swiss Federal Institute of Technology (EPFL), Lausanne (CH)*
- 2016 - 2018 **MSc in Civil Engineering**, specialisation in structural engineering
The Polytechnic University of Milan (Polimi), Milan (IT)
- 2015 - 2016 **Specialisation Degree in Civil Engineering**
University of Montenegro (UCG), Podgorica (MNE)
- 2012 - 2015 **BSc in Civil Engineering**, specialisation in structural engineering
University of Montenegro (UCG), Podgorica (MNE)

Professional Experience

- 2019 - 2024 **PhD research assistant**
*Structural Concrete Laboratory (IBETON),
Swiss Federal Institute of Technology (EPFL), Lausanne (CH)*
- Models for slender and squat concrete members with shear reinforcement based on stress fields to serve as a revision for the next generation of design codes (Model Code 2020 and 2nd generation of Eurocode 2). (*supervised by Prof. A. Muttoni and Prof. M. Fernández Ruiz*)
- Experimental and theoretical work on dowel action in steel reinforcement. (*supervised by Prof. A. Muttoni*)
- 2019 - 2024 **PhD teaching assistant**
*Structural Concrete Laboratory (IBETON),
Swiss Federal Institute of Technology (EPFL), Lausanne (CH)*
- Teaching assistant for courses:
“Structures I and II”, “Concrete structures”, “Conceptual design of bridges”, “Concrete bridges”, “Advanced design of concrete structures”, “Structure and Architecture”, “Stress fields”.
- Tutor/supervision of several master projects.

2016 **Teaching assistant in Civil Engineering**
University of Montenegro (UCG), Podgorica (MNE)

Publications

- 2024 Pejatović M., Muttoni A., *Steel stresses and shear forces in reinforcing bars due to dowel action*, 2024. [publication in preparation]
- 2024 Pejatović M., Muttoni A., *Experimental investigation of dowel action in reinforcing bars using refined measurements*, *Structural Concrete*, 2024. [submitted, December 2023]
- 2022 Pejatović M., Muttoni A., *Experimental investigation of dowel action using advanced measurement techniques*, *The fib 14th International PhD Symposium in Civil Engineering*, pp. 573-580, Rome, Italy, September, 2022.
- 2022 Pejatović M., Fernández Ruiz M., Muttoni A., *Design of slender and squat reinforced concrete members with shear reinforcement*, *Structural Concrete*, 2022.

Awards

- 2022 **The best paper in the category of “Retrofitting and assessment of existing structures”**
The *fib* 14th PhD Symposium in Civil Engineering, Rome, Italy, 5-7 September 2022
- 2013 - 2015 **Award for the best student in Civil Engineering**
University of Montenegro (UCG), Podgorica (MNE)

Computer skills

Microsoft Office, Illustrator, Matlab, Cubus, Autocad, Jconc